Title
Synchrotron X-ray Applications Toward an Understanding of Elastic Anisotropy

Author
Kanitpanyacharoen, Waruntorn

Publication Date
2012

Peer reviewed|Thesis/dissertation

Synchrotron X-ray Applications Toward an Understanding of Elastic Anisotropy

By

Waruntorn Kanitpanyacharoen

A dissertation submitted in partial satisfaction of the

requirements for the degree of

Doctor of Philosophy

in

Earth and Planetary Science

in the

Graduate Division

of the

University of California, Berkeley

Committee in charge:

Professor Hans-Rudolf Wenk
Professor Raymond Jeanloz
Professor Paulo Monteiro

Fall 2012

Synchrotron X-ray Applications Toward an Understanding of Elastic Anisotropy

By Waruntorn Kanitpanyacharoen

Abstract

Synchrotron X-ray Applications Toward an Understanding of Elastic Anisotropy

by

Waruntorn Kanitpanyacharoen

Doctor of Philosophy in Earth and Planetary Science

University of California, Berkeley

Professor Hans-Rudolf Wenk, Chair

The contribution of this dissertation is to expand the current knowledge of factors and mechanisms that influence the development of preferred orientation of minerlas and pores in different materials, ranging from rocks in Earth's crust to minerals in the deep Earth. Preferred orientation–a main contributing component to elastic anisotropy–is however very challenging to quantify. The overall focus of this thesis thus aims to (1) apply the capabilities of synchrotron X-ray techniques to determine preferred orientations of hexagonal metals and shales under different conditions and (2) enhance our understanding of their relationships to the elastic properties.

Lattice preferred orientation (LPO) or 'texture' of hexagonal close-packed iron (hcp- Fe) crystals during deformation has been suggested as the cause of the elastic anisotropy observed in Earth's inner core. However, relatively little is known about LPO of other hcp metals. An investigation of a wide range of hcp metals (Cd, Zn, Os, and Hf) as analogs to hcp-Fe was thus undertaken to better understand deformation mechanisms at high pressure and temperature in Chapter 2. The diamond anvil cell in a radial geometry (rDAC) and the D-DIA multi-anvil apparatus, equipped with a heating system, were used to impose both pressure and stress on the samples. These state-of-the-art tools enable us to create extreme conditions similar to the Earth's interior. A synchrotron X-ray beam is then employed to record diffraction patterns of the deformed materials. Results show that all hcp metals preferentially align their *c*-axes near the compression axis during deformation but with considerable differences. The gradual texture evolution in Cd and Zn is mainly controlled by {0001}<$2\bar{1}\bar{1}0$> basal slip systems while a rapid texture development in Os and Hf at ambient temperature is due to a dominant role of {$10\bar{1}2$}<$\bar{1}011$> tensile twinning, with some degree of {0001}<$2\bar{1}\bar{1}0$> basal slip. At elevated temperature, {$10\bar{1}2$}<$\bar{1}011$> tensile twinning is suppressed and texturing is governed by combined basal and prismatic slip. Under all conditions, {0001}<$2\bar{1}\bar{1}0$> basal slip appears to be the main deformation mechanism in hcp metals at high pressure and temperature. These findings are similar to those of hcp-Fe and useful to better understand the deformation mechanisms of hcp metals and their implications for elastic anisotropy.

Besides the investigation of deep Earth materials, this dissertation also considers crustal rocks: particularly shales, which are among the most anisotropic rocks. Shale has increasingly received attention because of its significance in prospecting for petroleum deposits, as well as seals in the context of CO_2 sequestration. Elastic anisotropy in shales is caused by the LPO of clay minerals as well as by shape preferred orientation (SPO) of pore, fractures, and the organic material (kerogen) network. However, due to the small grain size and poor crystallinity of swelling clays, the

LPO of clays is difficult to quantify. In Chapter 3, a high-energy synchrotron X-ray diffraction technique was applied to characterize LPO and phase proportions of Posidonia Shale collected in the Hils Syncline from Germany, in order to examine the influence of clay content, burial depth, and thermal history. The samples used in this study had experienced different local temperatures during burial and uplifting, as established by the maturity of kerogen (0.68-1.45% vitrinite reflectance, R_o), but their constituent clay minerals, including kaolinite, illite-mica, and illite-smectite, show similar degrees of LPO in all samples, ranging between 3.7 and 6.3 multiple of random distribution (m.r.d.). These observations imply that the difference in local thermal history, which significantly affects the maturity of kerogen, at most marginally influences LPO of clays, as the alignment of clays was established early in the history.

In Chapter 4, the SPO of constituents phases in Kimmeridge Shale (North Sea, UK) and Barnett Shale (Gulf of Mexico, USA) was quantified to a resolution of ~1 μm by using synchrotron X-ray microtomography (SXMT) technique. Measurements were done at different facilities (ALS, APS, and SLS) to characterize 3D microstructures, explore resolution limitations, and develop satisfactory procedures for data quantification. Segmentation images show that the SPO of low density features, including pores, fractures, and kerogen, is mostly anisotropic and oriented parallel to the bedding plane. Small pores are generally dispersed, whereas some large fractures and kerogen have irregular shapes and remain aligned horizontally. In contrast, pyrite exhibits no SPO. The volume fractions and aspect ratios of low density features extracted from three synchrotron sources show excellent agreement with 6.3(6)% for Kimmeridge Shale and 4.5(4)% for Barnett Shale. A small variation is mainly due to differences of optical instruments and technical setups. The SXMT is proven to be a crucial technique to investigate 3D internal structures of fine-grained materials at high-resolution.

A relationship between LPO, SPO, and elastic anisotropy of the Qusaiba Shale from the Rub'al-Khali basin in Saudi Arabia is established in Chapter 5. The Qusaiba samples exhibit strong LPO of clay minerals (2.4-6.8 m.r.d.) due to their high total clay content and high degree of compaction. The SPO of pores, fractures, and kerogen here are also anisotropic and organized mainly parallel to bedding, with little connectivity of the flat pores normal to the bedding. The microscopic information (LPO) extracted from different synchrotron X-ray techniques is then applied in different averaging approaches (Voigt, Reuss, Hill, and Geometric mean) to calculate macroscopic properties of shales. A comparison of calculated elastic properties ($V_{p(max)}$=6.2 km/s, $V_{p(max)}$=5.5 km/s, and V_p ani.% =12%) with ultrasonic measurements ($V_{p(max)}$=5.3 km/s, $V_{p(max)}$=4.1 km/s, and V_p ani.% =27%) suggests some discrepancy as the distribution of kerogen and the orientation of the microfracture and porosity network are not included in the averaging model. These features reduce the strength of the matrix, enhancing the elastic anisotropy. Through linking the matrix and porosity components, a more comprehensive model of shale elastic properties is thus necessary for a further study.

CONTENTS

FIGURES

TABLES

ACKNOWLEDGEMENTS

First and foremost, I would like to thank my family, particularly mom, dad, and Jib, for their unconditional love and support. Not only they understand my indefinite learning desire, but also encourage me to follow my dreams and live my life the way I want.

I am very grateful for receiving the Royal Thai Government scholarship, which has fully funded my degrees for the past 9 years. This life-changing opportunity has allowed me to enjoy invaluable learning experiences, American culture, and priceless friendship at Miss Porter's, Duke, and Cal. Cal and its very unique culture have taught me to be a problem solver, a team player, and a more responsible person to make this world better for everyone.

I also would like to express my sincere gratitude to my advisor, Rudy Wenk, who has always provided insightful advices on both professional and personal levels. I would like to thank him for every opportunity that he has given me in the past few years. His humble personality, dedication to science, and extraordinary success in research have inspired me to pursue my own passion and try to become the best I can be.

In addition, I would like to thank the Department of Energy and Carnegie/ Department of Energy Alliance Center and for funding my projects. I thank my thesis committees, Raymond Jeanloz and Paulo Monteiro for guidances and useful comments in this dissertation. Much appreciation also goes to former and current members in the Wenk's group: Marco Voltolini for teaching useful tricks in MAUD; Lowell Miyagi for being a great mentor and passing on the rDAC skills; Sébastien Merkel for answering hcp-metal questions; Eloisa Zepeda-Alarcon and Pam Kaercher for help with experiments and being an awesome company during beamtimes; Marie Jackson, Cagla Meral, and John Grimsich for useful suggestions on presentations and projects. I also thank Buddhi Godwal for introducing me to osmium, Tim Teague for his meticulous skills in sample preparation, as well as other EPS staff, especially Margie Winn, Dawn Geddes, Micaelee Ellswythe for assistance with administrative tasks.

I am very honored to have an opportunity to work with many experts from different synchrotron facilities, particularly Jason Knight, Selva Vennila Raju, Bin Chen, Jinyaun Yan, Simon Clark, Alastair MacDowell, and Dula Parkinson at the Advanced Light Source (ALS) of Lawrence Berkeley National Laboratory; Yang Ren, Chris Benmore, Francesco De Carlo, and Yanbin Wang at the Advanced Photon Source (APS) of Argonne National Laboratory; and Marco Stampanoni, Federica Marone, and Rajmund Mokso at the Swiss Light Source (SLS) of the Paul Scherrer Institute. I thank them for teaching me how to do experiments and spending hours tirelessly for troubleshooting. I also appreciate access to beamline 8.3.2 and 12.2.2 at ALS, which is supported by the Director, Office of Science, Office of Basic Energy Sciences, of the U.S. Department of Energy under (DOE-BES) under Contract No. DE-AC02-05CH11231, as well as beamline 2-BM-B, 11-ID-C, and 13-

BM-D, and 16-ID-B at APS, which is supported by DOE-BES, under Contract No. DE-AC02-06CH11357.

Moreover, I greatly appreciate help from Luca Lutterotti (MAUD), Siegfried Matthies (BEARTEX), and Carlos Tomé (VPSC) with data analysis software. I also would like to thank Frans Kets for many useful discussions on shale projects. His attention to detail has inspired me to always deliver the best work. I thank Christian Lehr, Brian Hornby, and Ruarri Day-Stirrat for providing shale samples. I thank Luca Duranti for giving me a summer internship opportunity at Chevron. It was an eye-opening experience for me into the business world.

Last but not least, my friends here and overseas contributed immensely to this dissertation. I thank Yui and Bier for always being there whenever I need it. I thank Hong and Bright for making our apartment feel as home. I thank Arm, Joe, Tippy, Annie, Jonas, Ong, May, Pam, Pla, Pure, Bump, Pik, Ice, Ou and Jade for always bringing fun into my life. I thank Kratae, Mon, Tor, Yim, Mol, Bell, and Teng for always supporting me from thousands of miles away. I thank Shan, Eloisa, Zack, Nicole, Ariana, Andrea, Sanne, Kelly, Emily, and Jean for being amazing fellows in EPS. I thank Edison and Oat for helping me figure out who I am and what I want to be.

To this end, I cannot express my gratitude enough for help from everyone. I never would have made it here without your support to the greatest extent. Thank you very much!

CURRICULUM VITAE

WARUNTORN (JANE) KANITPANYACHAROEN

janekanit85@gmail.com

1. EDUCATION

1.1. Ph.D. in Earth and Planetary Science, University of California, Berkeley (Dec 2012)
1.2. B.S. in Earth and Ocean Sciences, Duke University (May 2008)
Graduated with Distinction

2. RESEARCH INTERESTS

2.1. Preferred orientation, porosity, and elastic anisotropy in shales
2.2. Texture evolution and deformation mechanisms in hexagonal metals at high pressure and temperature

3. PROFESSIONAL EXPERIENCES

3.1. Geophysics intern, Chevron Corporation (Jun-Aug 2012)
3.2. Graduate student researcher, UC-Berkeley (Aug 2008-Dec 2012)
3.3. Graduate student instructor, UC-Berkeley (Jan-May 2010)
3.4. Geochemistry research assistant, Duke University (May 2007-May 2008)
3.5. Hydrology research assistant, Duke University (May-Dec 2006)
3.6. Resident advisor, Duke University (Aug 2005-May 2007)
3.7. Teaching assistant, Brewster Academy (Jun-Aug 2005)

4. LIST OF PUBLICATIONS

4.1. W. Kanitpanyacharoen, D. Parkinson, F. De Carlo, F. Marone, M. Stampanoni, R. Mokso, A. MacDowell, and H.-R. Wenk (2013) A comparative study of X-ray microtomography on shales at different synchrotron facilities: ALS, APS, and SLS. *Journal of Synchrotron Radiation,* 20:1-9.
4.2. B. Chen, K. Lutker, S.V. Raju, J. Yan, W. Kanitpanyacharoen, J. Lei, S. Yang, H.-R. Wenk, H.-K. Mao, and Q. Williams (2012) Texture of nanocrystalline nickel: probing the lower size limit of dislocation activity. *Science* (In press)
4.3. W. Kanitpanyacharoen, F.B. Kets, H.-R. Wenk, and R. Wirth (2012) Mineral Preferred orientation and microstructure of Posidonia Shale in relation to different degrees of thermal maturity. *Clays and Clay Minerals,* 60:315-329.
4.4. W. Kanitpanyacharoen, S. Merkel, L. Miyagi, P. Kaercher, C.N. Tomé, Y. Wang, H.-R. Wenk (2012) Significance of mechanical twinning in hexagonal metals at high pressure. *Acta Materialia,* 60:422-430.

4.5. W. Kanitpanyacharoen and A.E. Boudreau (2012) Sulfde-associated mineral assemblages in the Bushveld Complex, South Africa: platinum-group element enrichment by vapor refining by chlorite-carbonate fluids. *Mineralium Deposita,* doi 10.1007/s00126-012-0427-2

4.6. C. Janssen, W. Kanitpanyacharoen, H.-R. Wenk, R. Wirth, L. Morales, E. Rybacki, M. Kienast, G. Dresen (2012) Clay fabrics induced weakening in SAFOD core samples. *Journal of Structural Geology*, 43:118-127.

4.7. P. Kaercher, S. Speziale, L. Miyagi, W. Kanitpanyacharoen, and H.-R, Wenk (2012). Evolution of crystallographic preferred orientation across the cubic-to-rhombohedral phase transition in FeO. *Physics and Chemistry of Minerals,* 39:613-626.

4.8. W. Kanitpanyacharoen, H.-R. Wenk, F.B. Kets, C. Lehr, and R. Wirth (2011) Texture and anisotropy of Qusaiba Shales, Saudi Arabia. *Geophysical Prospecting,* 59:536-556.

4.9. L. Miyagi, W. Kanitpanyacharoen, S. Stackhouse, B. Militzer, and H.-R. Wenk (2011) The enigma of post-perovskite anisotropy: deformation versus transformation textures. *Physics and Chemistry of Minerals,* 38:665-678.

4.10. M.D. Buatier, A. Chauvet, W. Kanitpanyacharoen, H.-R. Wenk, J. F. Ritz, and M. Jolivet (2011) Origin and behavior of clay minerals in the Bogd Fault Gouge, Mongolia. *Journal of Structural Geology,* 34:77-90.

4.11. L. Miyagi, W. Kanitpanyacharoen, P. Kaercher, K.L.M. Lee, and H.-R. Wenk (2010). Slip systems in MgSiO3 post-perovskite: Implications for D" anisotropy. *Science,* 329:1639-1641.

4.12. H.-R. Wenk, W. Kanitpanyacharoen, and M. Voltolini (2010) Preferred orientation of phyllosilicates: comparison of fault gouge, shale and schist. *Journal of Structural Geology,* 32:478-481.

5. AWARDS

5.1. Outstanding Student Paper Award (Dec 2011) Mineral Rock Physics session at the American Geophysical Union Fall Meeting

5.2. Royal Thai Government Scholarship (May 2003-May 2013)

5.3. Carnegie/DOE Alliance Center Support (Aug 2008-Dec 2012)

5.4. Sarah LaBoskey Award, Duke University (May 2008)

5.5. Duke Undergraduate Research Support Grant (May 2007-May 2008)

CHAPTER 1

INTRODUCTION

1.1) MOTIVATION & GOALS

The directionality of elastic wave propagation has been observed throughout the Earth. Particularly in the Earth's solid inner core, a compressional wave travels approximately 3% faster along the Earth's rotational axis than the equatorial path (Morelli et al. 1986). This elastic anisotropy is generally believed to be caused by the lattice preferred orientation (LPO) or 'texture' of hexagonal close-packed iron (hcp-Fe) crystals during deformation (Jeanloz et al. 1988; Karato 1999; Wenk et al. 2000b). In fact, previous experimental studies suggest that hcp-Fe develops strong LPO with *c*-axes parallel to the compression direction at high pressure and temperature (e.g. Miyagi et al. 2008; Merkel et al. 2004). However, texture evolution of other hcp metals at high pressure is much less discussed. This has raised my interest in studying a wide range of hcp metals at extreme conditions to understand their texture development and underlying deformation mechanisms. The goals of the first part of this dissertation are to (1) quantify LPO of Zn, Os, Cd, and Hf at high pressure and temperature by performing synchrotron X-ray diffraction experiments with the diamond anvil cell in a radial geometry (rDAC) and the D-DIA multi-anvil press and (2) compare the experimental results with the visco-plastic self-consistent (VPSC) model to gain insight into which slip and/or twinning mechanisms activate the deformation and produce LPO. The findings are aimed to enhance our understanding of the deformation of hcp metals and their implications for elastic anisotropy.

Elastic anisotropy in the crustal rocks is another subject of my interests, particularly in shales which are among the most anisotropic rocks. Shales are defined as fine-grained sedimentary rocks, containing high volume fractions of clay minerals. Due to their sheet-like structure, these minerals preferentially align with (001) lattice planes parallel to the bedding plane, during sedimentation, compaction, and diagenesis (e.g. Ho et al. 1999; Aplin et al. 2006; Wenk et al. 2008). Recrystallization processes also lead to a reorientation of clay platelets, increased elastic and seismic anisotropy, and a loss of porosity and permeability (e.g. Baker et al. 1993; Hornby 1994; Sayers 1994; Johansen et al. 2004; Draege et al. 2006; Bachrach, 2011). Recently, shales have been recognized as unconventional gas reservoirs, which consequently have increased interest in studying their physical and chemical characteristics (e.g. Curtis 2010; Loucks et al. 2009; Schulz et al. 2010; Bernard et al. 2010). However, relatively little is known about lattice and shape preferred orientations (LPO and SPO) of clay minerals in these shales. The second part of this dissertation is thus aimed to (1) explore factors that affect the development of LPO by using high-energy synchrotron X-ray diffraction, (2) use synchrotron X-ray microtomography to quantify SPO of constituent phases in shales at high resolution, and (3) apply microstructural information extracted from synchrotron X-ray techniques in different averaging approaches to calculate macroscopic properties of shales, and then compare the calculations with ultrasonic velocity measurements. Through linking the LPO, SPO, and single crystal elastic properties of minerals, elastic properties of shale can be reliably predicted.

1.2) SYNCHROTRON X-RAY APPLICATIONS ON HEXAGONAL METALS

For over a decade, X-ray diffraction patterns obtained from rDAC experiments have been used to study LPO and lattice strain development under non-hydrostatic stresses in a wide range of materials at high pressure and temperature (e.g. Hemley et al 1997; Merkel et al. 2007; Miyagi et al. 2008; Merkel et al. 2009; Miyagi et al. 2010). The rDAC consists of two opposed diamonds that are used to compress a small polycrystalline sample between the diamond tips (or culets) while a probe beam, typically a monochromatic synchrotron X-ray with an energy of 25-30 keV, is brought in orthogonal to the compression direction. Without inserting a pressure medium, the diamond anvils impose both differential compressive stress and hydrostatic pressure on the sample, which is enclosed in an X-ray transparent gasket (e.g. boron-kapton epoxy). The polycrystalline sample then deforms ductily, activating intracrystalline deformation mechanisms, and thus lead to texture development. The modified Mao-Bell type rDAC with large openings on two sides is generally used and loaded in a holding frame for remote pressure control through a membrane of helium or argon gas. The rDAC studies can be performed at various synchrotron facilities but rDAC experiments in this dissertation were performed at the high-pressure beamline 16-ID-B (HPCAT) of the Advanced Photon Source (APS) at Argonne National Laboratory and beamline 12.2.2 of the Advanced Light Source (ALS) of Lawrence Berkeley National Laboratory.

In addition, an investigation of LPO of hcp metals at high pressure can be done by the D-DIA multi-anvil press, which consists of three pairs of anvils. Two pairs of anvils can be controlled independently, which allows us to increase pressure quasi-hydrostatically and impose axial differential stress separately (Wang et al. 2003). The D-DIA is also capable of reversing differential strain and equipped with resistive heating system, which is useful for studying effects of temperature on texture evolution. Unlike in the rDAC experiments where the sample size has to be very small (<10 μm), the D-DIA requires a millimeter-sized sample in the gasket. The D-DIA is also equipped with the X-ray radiography system, which can record the changes of sample length and provide a direct record of macroscopic axial strain. The D-DIA thus has significant advantages over versatility and sample preparation; however, it cannot attain high pressure ranges of the rDAC apparatus. The D-DIA experiments here were done at the beamline 13-BM-B (GSECARS) of the APS of at ANL.

The variation of X-ray intensity and diffraction peak positions along the rings are commonly observed during deformation experiments. The variation of X-ray intensity along azimuth of the rings indicates LPO attained during plastic deformation. The Rietveld refinement (Rietveld, 1969), implemented in the Material Analysis Using Diffraction (MAUD) software (Lutterrotti et al. 1997), is generally used to analyze the LPO and corresponding phase fractions. This method relies on a least-squares approach to minimize the difference between experimental diffraction data and a calculated model. Texture is computed by the EWIMV algorithm (Matthies et al. 1982), with a cylindrical symmetry around the compression direction imposed, to produce an orientation distribution (OD). The OD is represented as inverse pole figures (IPFs), which describe the orientation of the compression axis relative to the crystal coordinates. Pole densities are expressed as multiples of a random distribution (m.r.d.), where 1 m.r.d. corresponds to a random texture. Thus the higher m.r.d. number refers to the stronger degree of LPO.

The variation of peak positions (or lattice *d*-spacings) along azimuth of diffraction rings clearly indicates that the sample was under stress and experiencing elastic lattice distortion. If the single crystal elastic constants, the OD, and the lattice spacings in the diffracting subsets of grains are known, an elastic averaging model, Moment Pole Stress model (Matthies 1996, Matthies and Daymond 2001), can be applied to calculate the macroscopic differential stress that superimposes to the hydrostatic pressure.

1.3) SYNCHROTRON X-RAY APPLICATIONS ON SHALES

The quantification of LPO of clay minerals in shales is very challenging due to their small grain sizes and poor crystallinity, particularly in the swelling clay group. Much early work has been dedicated to quantify the alignment of mica platelets, which can be easily measured with the universal stage and petrographic microscope (e.g. Sander 1930). With advances in X-ray diffraction techniques, a pole figure goniometer method in transmission geometry was applied to fine-grained slates (e.g. Oertel 1983). This X-ray texture goniometer (XTG) technique relies on positioning the detector at the Bragg angle for a (001) basal reflection diffraction peak and recording intensity changes with sample orientation (Van der Pluijm et al. 1994). The LPO of phyllosilicates in various rock types such as gneiss, schists, and shales can be then be quantified (e.g. Curtis et al. 1980; Sintubin, 1994; Ho et al. 1995; Ho et al. 1999; Aplin et al. 2006; Valcke et al. 2006; Day-Stirrat et al. 2008a,b). However, these two methods work well with minerals that have reasonably large grain sizes and only measures (001) pole figures. Thus there is very little orientation information of other directions (e.g. *a*-axes). Moreover, in shales the detrital illite-muscovite is overlapped with authigenic illite-smectite at the 10Å peak, as well as the kaolinite peak at 7Å is superimposed on the chlorite peak. These distinct peaks cannot be separated by the universal stage and the XTG methods. A more robust and reliable technique is therefore critically important for obtaining a complete orientation distribution of clay minerals in shales.

A high-energy (>100 keV) synchrotron X-ray diffraction technique at BESSRC 11-ID-C of the APS has been used to provide the information about LPO of various shales (e.g. Lonardelli et al. 2007; Wenk et al. 2008; Voltolini et al. 2009; Wenk et al. 2010). This method relies on full X-ray diffraction spectra, rather than individual diffraction peaks. The high brilliance and intensity of synchrotron X-ray can penetrate through a milimeter-sized sample with minor absorption. The advancement of detector technology and software updates at 11-ID-C further decreases the data acquisition time and allows multiple samples to be collected in a day. During X-ray exposure, the sample is tilted and translated along the horizontal axis to provide sufficient pole figure coverage and enough grain statistics. Similarly to the patterns observed in the rDAC and D-DIA experiments, some diffraction rings of minerals in shales show the variation of X-ray intensity along the azimuth, indicating LPO. Also here the LPO is quantified by the Rietveld analysis in MAUD. This approach not only can quantitatively determine the degree of LPO and volume fractions of multiple phases in shales, but also can separate overlapping peaks ~10 Å of illite-mica and illite-smectite. Pole densities are represented as pole figures (PF) that describe the orientation of crystallites in the crystal coordinates in the relative to the sample coordinates. The (001) PF corresponds to the basal plane of clay minerals thus is often illustrated in this study.

While LPO in shales can be derived from synchrotron X-ray diffraction experiments (Wenk et al. 2008; Voltolini et al. 2009, Wenk et al. 2010), the three-dimensional (3D) SPO is difficult to quantify due to their multiple phase composition and small grain sizes. Synchrotron X-ray microtomography (SXMT) has been used to examine the 3D internal structure of a wide variety types of rocks such as sandstone (Lindquist et al. 2000), meteorites (Friedrich et al. 2008), and gypsum (Fusseis et al. 2012), but a very little work on shales has been reported. The SXMT experiments in this study were performed at beamline 8.3.2. at the ALS of LBNL, beamline 2-BM at the APS of ANL, and beamline TOMCAT at the Swiss Light Source (SLS) of the Paul Scherrer Institut, Switzerland. The SXMT technique is based on different linear attenuation coefficients of constituent phases (Beer-Lambert's law). The X-ray penetrates and transmits through a rotating cylinder of shale in small incremental steps. The transmitted X-ray intensity is absorbed by a thin scintillator screen, which converts X-ray to a certain wavelength of visible light, depending on scintillator material. The visible light is projected on to a CCD detector through an objective lens,

producing an X-ray attenuation map for 3D reconstruction. The reconstructed data is segmented for materials of interest by a thresholding method. The threshold values separate the image into background and foreground by assigning a label to every voxel and effectively distinguishing between low- and high-absorbing phases. For shales, the SPO distribution or 'aspect ratio' of low density features, including pores, fractures, and kerogen, is of most interest as the information can be used in anisotropic velocity modeling.

1.4) OUTLINE OF THESIS

A systematic evolution of LPO in Cd, Zn, Os, and Hf is investigated in Chapter 2 by using the rDAC and the D-DIA apparatus. Results show that hcp metals orient their *c*-axes near the compression axis during deformation. At room temperature, a rapid texture development in Os and Hf is contributed mainly by tensile twinning, with some degree of basal slips, while a gradual texture evolution of LPO in Cd and Zn is activated by basal slip systems. Based on experiments, basal slip appears to be the main deformation mechanisms of hexagonal metals at high pressure and temperature, similarly to hcp-Fe. Portions of this chapter have been previously published in Kanitpanyacharoen et al. (2012a). I am the primary contributing author of this work and contributions from others are presented in the Acknowledgements and the text of this chapter.

In Chapter 3, a high-energy synchrotron X-ray diffraction technique was applied to characterize LPO and phase proportions of the Posidonia Shale collected in the Hils Syncline, Northern Germany. Thermal maturity of Posidonia Shale varies strongly as a function of location, indicating differences in local history and kerogen maturity (0.68-1.45%R_o). The degree of LPO of all clay minerals and in all samples is similar, ranging from 3.7 to 6.3 m.r.d. Calcite also displays weak LPO, with *c*-axes perpendicular to the bedding plane (1.1-1.3 m.r.d.). These observations suggest that the difference in thermal history only marginally influenced the LPO of clays as the alignment seems to have evolved early in history. Portions of this chapter have been previously published in Kanitpanyacharoen et al. (2012b). I am the primary contributing author of this work and contributions from others are presented in the Acknowledgements and the text of this chapter.

Chapter 4 addresses the significance of the SPO of constituent phases in Kimmeridge Shale and Barnett Shale. The samples were measured by using SXMT technique at the ALS, APS, and SLS. Internal features such as pyrite and low density features, including pores, fractures, and organic matter were segmented on the same basis and calculated for volume fractions. In general, low density features are anisotropic and aligned parallel to the bedding plane whereas pyrite shows no SPO. A small variation of SPO distribution and volume fractions is mainly due to different types of optical instruments and varying technical setups. Portions of this chapter have been previously published in Kanitpanyacharoen et al. (2013). I am the primary contributing author of this work and contributions from others are presented in the Acknowledgements and the text of this chapter.

In the last chapter, the LPO and SPO of Qusaiba Shale from Saudi Arabia were determined for elastic properties calculations. Clay minerals show a strong degree of LPO (2.4-6.8 m.r.d.) due to high total clay content and high degree of compaction of the samples. The geometry of low density features is mostly anisotropic and oriented horizontally. The orientation distributions of clays were applied in different averaging methods to predict the elastic velocities of shales. A discrepancy between the calculated and experimental velocities was observed and attributed to the effects of anisotropic pore/fracture present in the sample, which have not been taken into account in the matrix averaging. A more comprehensive model of shale elastic properties is thus necessary for a further investigation. Portions of this chapter have been previously published in Kanitpanyacharoen et al. (2011). I am the primary contributing author of this work and contributions from others are presented in the Acknowledgements and the text of this chapter.

CHAPTER 2

TEXTURE & DEFORMATION MECHANISMS OF HEXAGONAL METALS AT EXTREME CONDITIONS

2.1) INTRODUCTION

Hexagonal metals are divided into two categories according to the *c/a* ratio: those with high *c/a* axial ratios (e.g. zinc, cadmium) and those with low *c/a* ratios (e.g. hafnium, osmium). Due to their unique properties, Zn, Cd, Hf, and Os are chosen as analogs for hcp-Fe in this study. Zn is considered to be weak and generally brittle (Yoo 1981). Interestingly, the *c/a* ratio of Zn evidences an 'anomalous effect' and decreases substantially with pressure (Takemura 1997; Fast et al. 1997). On the other hand, Os is a dense and hard metal belonging to the platinum group, with very low compressibility (Gschneidner 1964) and a very high bulk modulus (395-435 GPa) (Takemura 2004; Occelli et al. 2004), second only to diamond. A recent report also suggests strong elastic anisotropy in Os at high pressure (Weinberger et al. 2008).

At high pressures, texture development in polycrystals depends on the active deformation mechanisms. Much research has been devoted to model deformation of hexagonal metals by polycrystal plasticity theory. Particularly useful has been a visco-plastic self-consistent (VPSC) model (Hutchinson 1976), further developed by Molinari et al. (1987) and later refined by Lebensohn and Tomé (1993). Comparing experimental texture patterns with VPSC simulations provides insight into which slip and/or twinning mechanisms are active under a given set of deformation modes. By having different hexagonal metals tested at high pressure and temperature in the rDAC and Deformation-DIA (D-DIA) experiments, this work is aimed to investigate texture evolution and the significance of mechanical twinning as a deformation mechanism by directly observing *in-situ* elastic and plastic behaviors of Zn, Cd, Hf and Os.

2.2) EXPERIMENTAL TECHNIQUES

2.2.1) The Diamond Anvil Cell in Radial Geometry (rDAC)

The experiment on Zn polycrystals (Alfa Aesar 99.9%+ purity) was performed at beamline 16-ID-B (HPCAT) of the APS. Small Zn grains (<10 μm) were packed into a 80 μm sample chamber of boron-kapton gasket (Merkel and Yagi 2005). A Pt flake (Alfa Aesar foil, 10 μm diameter, ~5 μm thickness) was also imbedded in Zn as an internal pressure standard. To estimate pressure during the experiment, the equation of state of Pt (Fei et al. 2007) was applied. A monochromatic X-ray with a wavelength of 0.39853 Å and 10x10 μm in size was brought in orthogonal to the compression direction and used to collect each diffraction pattern for 300s (Fig. 2.1a). Diffraction images were recorded on a 2θ range from 0° to 31.5° with a Mar345 detector, positioned about 348 mm from the sample.

An analogous experiment on Os was conducted at beamline 12.2.2 of the ALS. Os grains (Alfa Aesar Os 99.9%, <10 μm in size) and a small flake of Pt were loaded in the same gasket type and assembled in the same rDAC. The X-ray beam with a wavelength 0.49594 Å was focused to 20x20 μm to penetrate through the sample. Diffraction patterns were collected on a 2θ range from 0° to 38° with a Mar345 image plate detector, situated around 287 mm away from the sample.

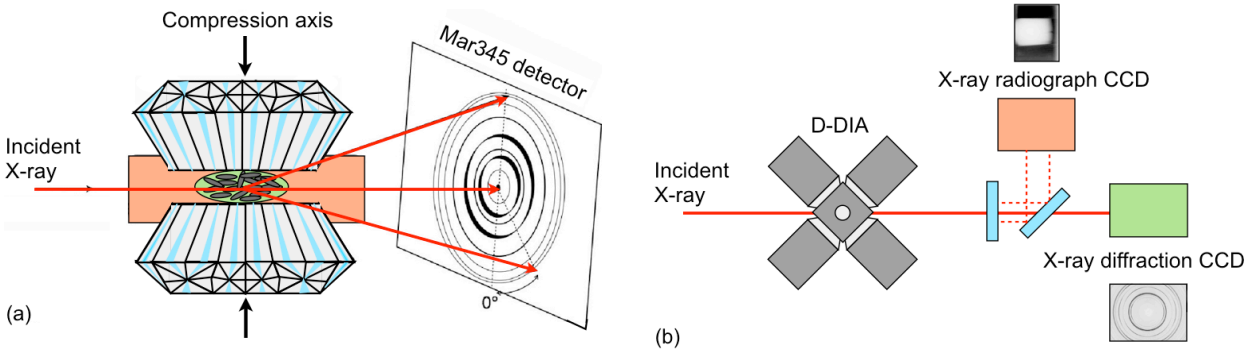

Figure 2.1: A schematic diagram of (a) the rDAC experiment and (b) the D-DIA setup.

2.2.2) The D-DIA Multi-Anvil Press

The D-DIA experiments were performed on Cd and Hf at beamline 13-BM-D (GSECARS) of the APS (Fig. 2.1b). The D-DIA requires a hydraulic press to generate forces (in ton) that drive the anvils together, which consequently increases the pressure of the sample (in GPa). More details of the D-DIA setup are described in Wang et al. 2003. The X-ray beam of wavelength 0.20663 Å was collimated to 200 x 200 μm and brought through space between the anvils assembly. Cylindrical samples, 0.5 mm in diameter and 0.8 mm in length, (ESPI metals, high purity) were cut and loaded into a boron nitride sleeve and capped on both ends with densified alumina disks to serve as pistons. Diffraction patterns were recorded on a Mar165 charge-coupled device (CCD) for 600 s. X-ray radiography also recorded the changes of wire length, providing a direct measure of macroscopic axial strain.

The experiment of Cd was done at room temperature and compressed quasi-hydrostatically to 20 tons (~4 GPa). Cd was gradually applied axial shortening to 52% strain then followed by axial lengthening back to 0% natural strain. Similar experiments were carried out on Hf under two different conditions. At ambient temperature, the first run was compressed quasi-hydrostatically to 15 tons (~4 GPa) and slowly deformed to 30% strain. Differential rams were then reversed to lengthen the wire to the initial length. The same steps were repeated in the second run, except Hf was compressed to 5 tons (~1 GPa) and simultaneously heated to 700 K during deformation.

2.3) Data Analysis

The diffraction patterns of standard material (e.g. for LaB_6 for rDAC and CeO_2 for D-DIA) were used to calibrate the instrument geometry such as sample-detector distance, beam center, and image plate tilt in Fit2D (Hammersley 1998). These instrumental parameters were then use to analyze experimental data in MAUD software (Lutterrotti et al. 1997). MAUD relies on the Rietveld refinement (Rietveld, 1969), which is based on a least-squares approach to minimize the difference between experimental diffraction data (dotted) and a calculated model (solid) (Fig. 2.2a and c). The calculated model is defined by several factors such as instrumental parameters, scattering background, crystal structure, microstructure, weight fraction of each phase, and its preferred orientation. The experimental diffraction image was first integrated or 'unrolled' in 10° incremental

steps along the azimuth to produce 36 spectra, representing distinctively oriented lattice planes. The spectra are expressed as function of $Q=2\pi/d$ rather than *d* (lattice spacing), where everything becomes compressed towards small lattice spacings. The spectra were refined with background polynomial functions, scale parameters, phase volume fraction, and lattice parameters, but atomic coordinates were kept constant. The peak shapes and widths were modeled by refining isotropic crystallite size and microstrain. A comparison of calculated model (top) with experimental spectra (bottom) (Fig. 2.2b and d) indicates a close similarity indicative of an excellent fit, both in intensities as well as position of diffraction peaks.

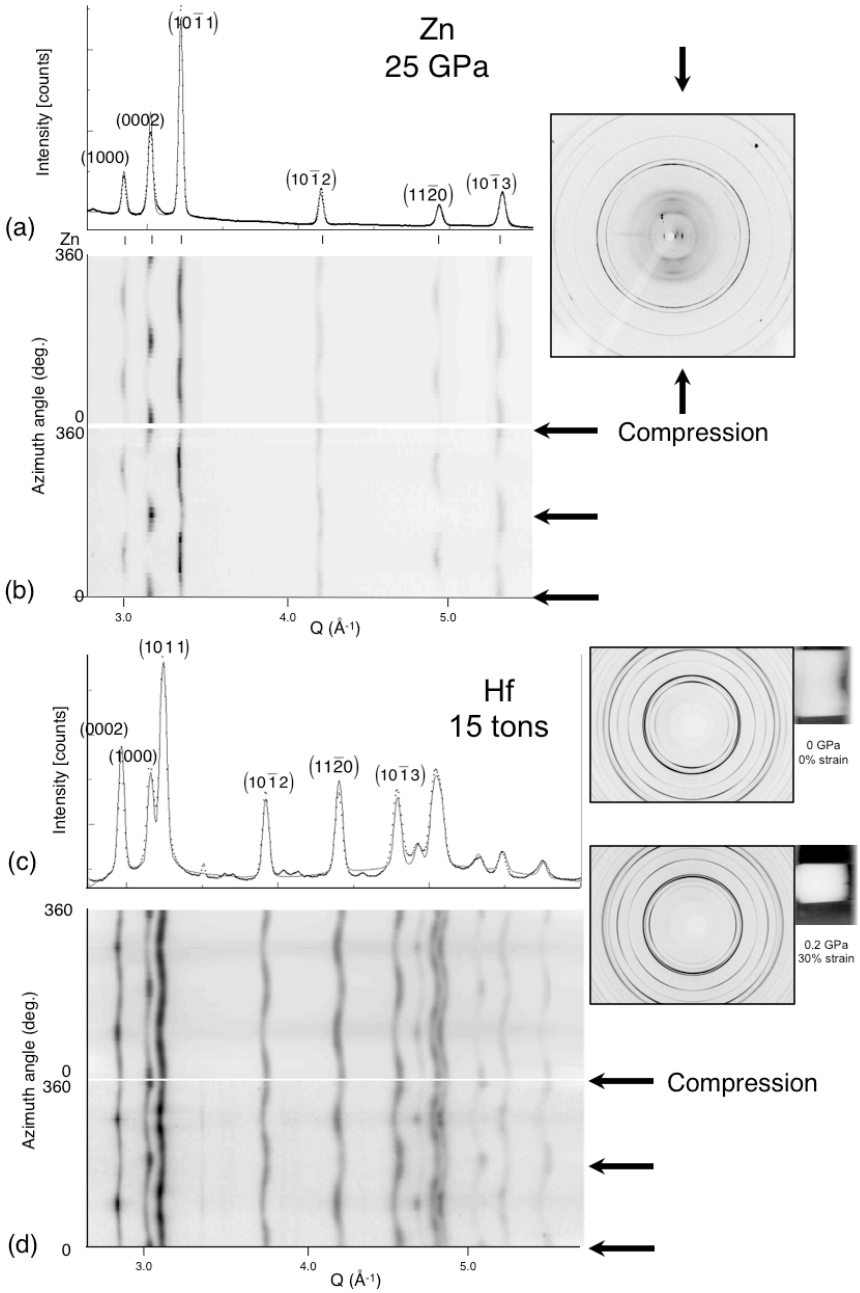

Figure 2.2: Diffraction patterns of (a) Zn at 25 GPa and (b) Hf at 1 GPa with 20% strain, and unrolled images (c) of Zn and (d) of Hf diffraction rings, show the variation of intensity and d-spacings, indicating texture development and stress imposed on the sample.

2.3.1) Lattice Preferred Orientation (LPO)

The variation of intensity along the diffraction rings immediately indicates LPO attained during plastic deformation (insets of Fig. 2.2). Quantitative texture was computed by the EWIMV algorithm (Matthies et al. 1982), with a cylindrical symmetry around the compression direction imposed, to produce an orientation distribution (OD). The OD from MAUD was exported to the BEARTEX software (Wenk et al. 1998) and smoothed with a 7.5° filter to minimize artifacts from OD cell structures. Inverse Pole Figures (IPFs), which describe the orientation of the compression axis relative to the crystal coordinates, are used for representation. Figure 2.3 illustrates the lattice geometry of hcp metals, including major slip systems, in crystal coordinates and equal area projection. Due to the hexagonal crystal symmetry, a 30° partial IPF is sufficient to represent complete texture information (shaded area in Fig. 2.3). Pole densities are expressed as multiples of a random distribution (m.r.d.), where 1 m.r.d. corresponds to a random texture. Note that texture strength is defined as the maximum density in the measured IPF.

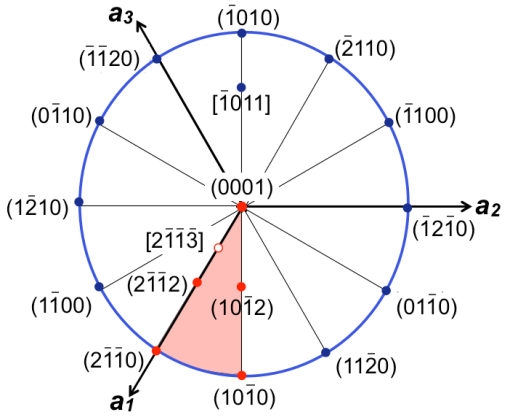

Figure 2.3: A complete IPF describes the orientation of the sample axis on a stereogram plotted relative to the crystallographic coordinates in equal area projection. A 30° partial IPF plotted on a stereographic triangle (shaded) is used to represent the OD. Filled circles are upper hemisphere and empty circle is lower hemisphere.

2.3.2) Stress and Strain

Sinusoidal variations in peak positions are a result of deviatoric stress imposed by the rDAC or the D-DIA on the sample. The pressure was determined by fitting unit cell parameters (corrected for non-hydrostatic stresses) with a third-order Birch-Murnaghan equation of state (EOS) (Birch 1947). The initial volume at atmospheric pressure (V_0) of Zn is 30.24 Å^3, and values for bulk modulus (K_0) and its pressure derivative (K') are 65 GPa and 4.6 GPa respectively (Takemura 1997). Pressures of the other metals were calculated with the same approach. For Os: V_0 = 27.98 Å^3, K_0 = 411 GPa and K' = 4.0 (Occelli et al. 2004), Cd: V_0 = 43.17 Å^3, K_0 = 42 GPa and K' = 6.5 (Occelli et al. 2004), and Hf: V_0 = 43.36 Å^3, K_0 = 105 GPa and K' = 3.95 (Ostanin and Trubisin 2000).
The variation of peak positions along azimuth of diffraction rings clearly indicates that the sample was under deviatoric stress and experiencing elastic lattice distortion. If the single crystal elastic constants, the texture and the *d*-spacings in the diffracting subsets of grains are known, an elastic averaging model, Moment Pole Stress model (Matthies 1996, Matthies and Daymond 2001), can be applied to calculate the macroscopic deviatoric stress that superimposes to the hydrostatic pressure. Single crystal elastic constants (C_{ij}) of Zn (Ledbetter 1977) and Hf (Hao et al. 2010) at ambient pressure, and of Os (Deng et al. 2008) and Cd (Garland and Silverman 1960) at various pressures, were used to determine the deviatoric stress component. According to the geometry of axial

compression and axially symmetric textures, the deviatoric stress component (S_{ij}) in the rDAC and the D-DIA (Matthies and Vinel 1982; Wenk et al.1998) is described as

$$S_{ij} = \begin{bmatrix} -t/3 & 0 & 0 \\ 0 & -t/3 & 0 \\ 0 & 0 & -t/3 \end{bmatrix}$$

where t is differential stress and refers to the difference between the largest and smallest compressive stress. The differential stress also provides a lower bound of yield strength such that compressive stresses are negative. Lattice parameters refer to the hydrostatic condition, i.e. at an azimuth of 54.7° to the compression direction (Singh et al. 1998; Singh and Balasingh 1994)

Axial plastic strain is more difficult to estimate and to distinguish from elastic strain for rDAC experiments. This is due to the small sample size, the effect of the confining gasket material, compaction of the original powder and the geometry of rDAC and gasket. Judging from texture development in previous rDAC experiments on a wide range of materials, it is estimated that axial strain of 20-25% may be reached at 20 GPa (Miyagi et al.2008; Merkel et al. 2004; Wenk et al. 2000; Merkel et al. 2009). At higher pressures, strain continues to increase but at a diminishing rate. For D-DIA experiments, X-ray radiographs can be used to calculate the macroscopic strain (ε) that is defined as $\varepsilon = 100 * ln\,(l_0/l)$, where l_0 is the initial sample length after quasi-hydrostatic compression (Miyagi et al. 2008).

2.4 RESULTS

2.4.1) Stress

Data analysis was performed on selected diffraction images and details about pressure, differential stress, lattice parameters and texture strength are summarized in Table 2.1. In general, lattice parameters and the c/a ratio of hcp metals decrease as a function of pressure (Fig. 2.4).

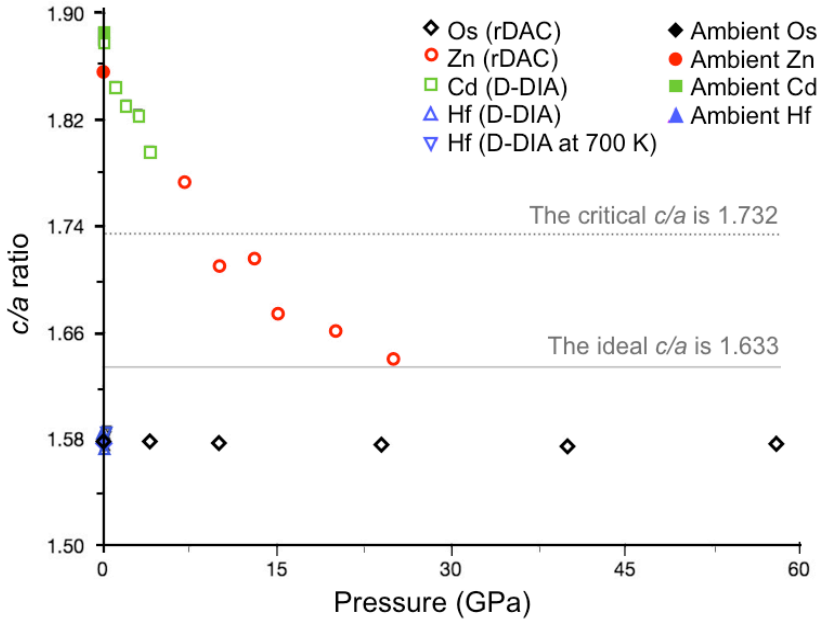

Figure 2.4: A diagram illustrates the c/a ratio of studied hcp metals decreases as a function of pressure (open symbols). The ideal values for Zn, Os, Cd and Hf are shown with full symbols.

While the axial ratio of Zn and Cd deviates strongly from their initial values at atmospheric pressure, the changes in *c/a* ratio of Os and Hf are minimal over the pressure ranges explored in this study. The evolution of differential stress (*t*) with pressure or strain varies for different experiments (Table 2.1). For Zn, Cd, and Hf, differential stresses are relatively low (≤ 1 GPa) due to the low yield strength of plastic systems for those metals. In contrast, the differential stress of Os is high and reached 6.31 GPa at a pressure of 58 GPa.

2.4.2) Lattice Preferred Orientation (LPO)

2.4.2.1) Zinc

Diffraction images at ambient pressure show that both, Zn and Os crystals are initially randomly oriented in the aggregate, since the intensity is uniform along the diffraction rings. As compression and deformation continue, a systematic variation of diffraction intensity and lattice spacings with azimuthal angles is observed in the samples (inset of Fig. 2.2). In Zn, only a very weak (0001) maximum develops (1.27 m.r.d.) at 10 GPa (Fig. 2.5a, no. 2). Texture gradually strengthens at 15 GPa to 2.57 m.r.d and reaches 5.18 m.r.d at 25 GPa (Fig. 2.5a, no. 5). The degree of LPO in Zn at 25 GPa is four times stronger than that at 10 GPa, suggesting a different mechanism in texture development at high pressure. This behavior is later described in the Discussion section.

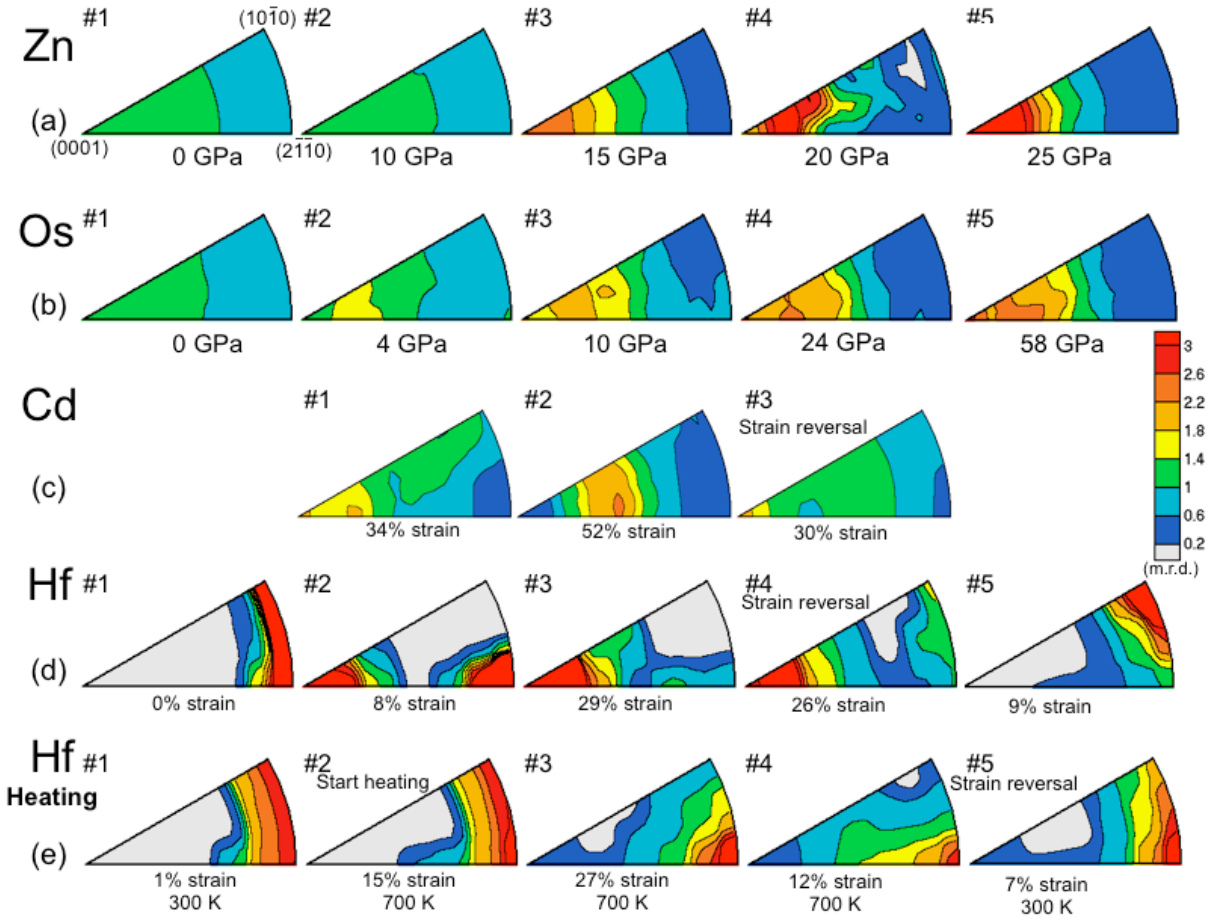

Figure 2.5: IPFs of (a) Zn, (b) Os, (c) Cd, and (d)-e) Hf at selected pressures. Pole densities are expressed as multiples of random distribution (m.r.d.). Equal area projection, linear scale and contours.

2.4.2.2) Osmium

Os behaves very differently. At pressure as low as 4 GPa, a weak texture immediately develops with a 1.89 m.r.d. maximum near (0001) (Fig. 2.5b, no. 2). The texture strength increases with pressure to 2.33 m.r.d. at 10 GPa, and then reaches 2.99 m.r.d. at 58 GPa (Fig. 2.5b, no. 5). The IPF maximum remains near (0001), though it is always slightly displaced.

2.4.2.3) Cadmium

Cd initially shows a spotty diffraction pattern, indicating large crystals and poor grain statistics (Fig. 2.6a). Crystallite size decreases as compression proceeds, allowing texture to develop (Fig. 2.6b). Upon applying quasi-hydrostatic pressure to 4 GPa and imposing axial shortening to 34% strain, a weak texture (2.04 m.r.d.) is observed near (0001) but slightly displaced (Fig. 2.5c, no. 1). Texture in Cd becomes strongest (2.53 m.r.d.) when deformed to 52% strain (Fig. 2.5c, no. 2), but the maximum shifts ~30° from (0001). The maximum reverses back to near (0001) during decompression and strain reversal (Fig. 2.5c, no. 3), and becomes weak at room condition.

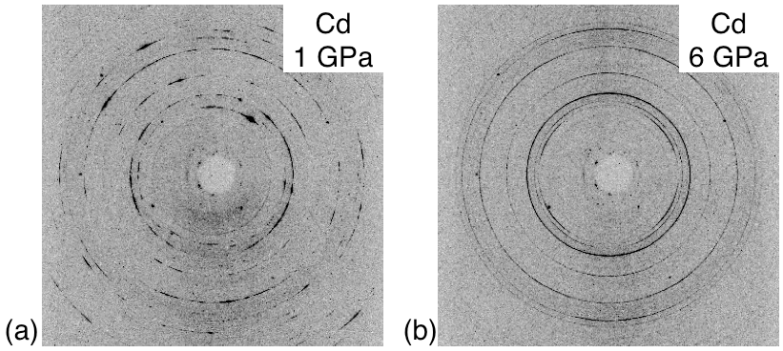

Figure 2.6: Diffraction patterns of Cd at (a) 1 GPa and (b) 6 GPa. A spotty pattern indicates large grain size, which becomes smaller upon compression to a higher pressure.

2.4.2.4) Hafnium

The diffraction image of starting Hf wire (Fig 2.2d, inset) shows a strong texture (7.72 m.r.d.), with an IPF maximum near $(2\bar{1}\bar{1}0)$ and $(10\bar{1}0)$ (Fig. 2.5d, no. 1), corresponding to a typical hcp extruded wire texture (MacEwan and Tomé 1987; Tenckhoff 1988). In the first run, at room temperature, an IPF maximum near (0001) starts to develop as soon as quasi-hydrostatic pressure is applied to 4 GPa (Fig. 2.5d, no. 2). Simultaneously, depletion around the $(10\bar{1}0)$ orientation takes place, which is consistent with tensile twinning reorientation. Upon further compression the strength of the (0001) maximum quickly increases and then saturates. As deformation proceeds to 29% strain, the maximum near (0001) reaches 6.91 m.r.d., while the initial maxima near $(2\bar{1}\bar{1}0)$ and $(10\bar{1}0)$ become depleted (Fig. 2.5d, no. 3). An IPF maximum evolves near $(10\bar{1}0)$ during strain reversal and decompression. In the second run at 700 K, Hf crystals are oriented with the IPF maximum of 3.30 m.r.d near $(2\bar{1}\bar{1}0)$ and $(10\bar{1}0)$ (Fig. 2.5e, no. 1). As hydrostatic pressure is applied to 1 GPa and axial shortening of 15% strain imposed, texture shifts from $(10\bar{1}0)$ to near $(2\bar{1}\bar{1}0)$ (4.36 m.r.d.) (Fig. 2.5e, no. 2). During decompression and strain reversal, the IPF maximum gradually decreases but remains near $(2\bar{1}\bar{1}0)$ (Fig. 2.5e, no. 5). These observations are different from the first run, suggesting that temperature has a significant effect on deformation in Hf.

Table 2.1: A summary of cell parameters (Å), texture strength (m.r.d.) and differential stress (t) (GPa) change as a function of pressure (GPa).

Sample	Load (ton)	P (GPa)	a (Å)	c (Å)	c/a	Max(m.r.d.)	t (GPa)	Strain %	T (K)	Note
Zn	-	0	2.6594(1)	4.9368(1)	1.8564	1.08	0.00	-	300	
(rDAC)	-	10	2.6216(1)	4.4825(2)	1.7098	1.27	-0.18	-	300	
	-	15	2.6036(1)	4.3597(2)	1.6744	2.57	-0.15	-	300	
	-	20	2.5867(1)	4.2979(2)	1.6615	3.45	-0.27	-	300	
	-	25	2.5453(1)	4.1756(2)	1.6405	5.18	-0.48	-	300	
Os	-	0	2.7330(1)	4.3163(2)	1.5793	1.29	-0.42	-	300	
(rDAC)	-	4	2.7264(1)	4.3046(2)	1.5789	1.89	-2.44	-	300	
	-	10	2.7135(1)	4.2828(1)	1.5783	2.33	-3.91	-	300	
	-	39	2.6647(1)	4.1992(2)	1.5759	2.61	-5.79	-	300	
	-	58	2.6324(1)	4.1552(2)	1.5785	2.99	-6.31	-	300	
Cd	2	0	2.9695(1)	5.5793(1)	1.8789	-	-	0	300	
(D-DIA)	10	1	2.9594(1)	5.4606(2)	1.8452	-	-	10	300	
	20	4	2.9311(1)	5.2663(2)	1.7967	2.04	-0.10	34	300	
	20	4	2.9303(1)	5.2697(1)	1.7983	2.53	-0.11	52	300	
	20	2	2.9513(1)	5.4047(2)	1.8313	2.03	0.09	30	300	Strain reversal
Hf	0	0	3.2220(1)	5.0907(1)	1.5800	8.19	-0.22	0	300	
(D-DIA)	15	3.9	3.1856(1)	5.0370(2)	1.5811	9.64	-0.70	8	300	
	15	4.4	3.1861(1)	5.0168(1)	1.5746	6.91	-0.97	29	300	
	15	2.3	3.1972(1)	5.0657(1)	1.5844	3.98	1.00	26	300	Strain reversal
	15	1.3	3.2125(1)	5.0615(1)	1.5755	8.03	0.84	9	300	Strain reversal
Hf	2	0	3.1600(1)	4.9972(1)	1.5814	3.30	0.03	1	300	
(D-DIA)	5	0.6	3.1597(1)	5.0166(2)	1.5877	4.36	-0.36	15	700	Start heating
Heating	5	0.5	3.1618(1)	5.0165(2)	1.5866	2.89	-0.24	27	700	
	5	0.8	3.1608(1)	5.0019(1)	1.5824	3.69	0.20	12	700	Strain reversal
	1	0.1	3.1563(1)	5.0056(1)	1.5859	2.79	0.16	7	300	

2.5) DISCUSSION

2.5.1) Visco-Plastic Self-Consistent (VPSC) Simulations

The rDAC and D-DIA experiments induce both plastic and elastic deformations. Plastic strains produce texture development while elastic strains are only used to infer stress conditions. An interpretation of texture patterns relied on a comparison of experimental observations with simulations of the VPSC polycrystal code (Lebensohn and Tomé 1993), which neglects elasticity and accommodates deformation by slip and twin shear. VPSC can generate deformation textures for different combinations of active systems and different strains, by treating each crystal as a visco-plastic inclusion in a homogeneous but anisotropic medium with the average properties of the polycrystal. The polycrystal yield surface, which is defined as the locus of stress states that induce plastic yield at constant dissipation rate, can also be calculated from texture and active deformation mechanisms of the polycrystal (Lebensohn and Tomé 1993). However yield surface is not computed in this study due to the lack of adequate experimental data of yield stress for comparison.

Two thousand initially randomly oriented crystals were used to simulate the Zn, Cd and Os aggregates. However, the experimentally measured texture of the extruded Hf wire was introduced as the starting distribution for the Hf plasticity simulations. The OD of Hf wire at ambient was quantified, exported from MAUD, and used to assign weights to the initial two thousand orientations in BEARTEX (Wenk et al. 1998). Crystals deform plastically and preferentially reorient as compressive strain is applied in 20 steps of 1% strain. Deformation mechanisms for hcp metals are well established (Yoo 1981), and this study investigates dominant basal and prismatic slip, and tensile and compressive twinning. Different values of critical resolved shear stress (CRSS, Table 2.2) for the deformation modes generate distinctive texture patterns. CRSS is given by $\sigma \cos \Phi \cos \lambda$, where σ is the applied compression stress, Φ is the angle between the slip/twinning plane normal and the compression direction, and λ is the angle between the slip/twinning direction and the compression direction. The CRSS were chosen to explore the importance of slip and twining on texture patterns and are kept constant through the simulation. Work-hardening is not taken into account here due to a lack of accurate measurements of the macroscopic stress-strain response. To conform with estimated strains in the rDAC experiments, simulated IPFs for 5% and 20% compressive strain are shown.

Many studies of hcp metals (Brown et al. 2005; Clausen et al. 2008; Proust et al. 2007; Cerreta et al. 2007) have shown that mechanical twinning plays a major role in texture development. The characteristic twinning shear (g) can be calculated from the c/a axial ratio (γ) (Yoo 1981). It relates the amount of shear contributed by the twin system $\Delta\gamma^{tw}$ with the volume fraction of the grain that reorients by twinning f^{tw} as: $\Delta\gamma^{tw} = g f^{tw}$. Because g adopts values lower than 0.2 for the cases considered here, it turns out that even small amounts of twin shear activity require large volume fractions to reorient by twinning. This work explored the most commonly observed twinning modes, i.e. $\{10\bar{1}2\}<1011>$ tensile twinning, and $\{2\bar{1}\bar{1}2\}<2\bar{1}\bar{1}\bar{3}>$ compressive twinning, but only selected simulations that are compatible with experimental results are displayed in Fig. 2.7. Mechanical twinning is unidirectional and is characterized by the ability to produce either compressive or tensile strain parallel to the c-axis (Yoo 1981). Thus, the conventional use of "tensile and compressive twinning" refers to the c-axis strain and not the deformation experiment.

In model A, basal slip on $\{0001\}<2\bar{1}\bar{1}0>$ is the dominant deformation mechanism. Basal slip was combined with $\{10\bar{1}2\}<1011>$ tensile twinning in model B and with compressive twinning on $\{2\bar{1}\bar{1}2\}<2\bar{1}\bar{1}\bar{3}>$ in model C. Model D considered basal slip and $\{10\bar{1}0\}<\bar{1}2\bar{1}0>$ prismatic slip. Two sets of simulations with the same conditions were performed, first with an initial random orientation distribution (Fig. 2.7a) and another set with an initial extruded wire texture (Fig. 2.7b)

based on Hf (Fig. 2.5d, no. 1). Output of the simulations also includes the relative activity of deformation mechanisms as a function of applied strain (Fig. 2.8).

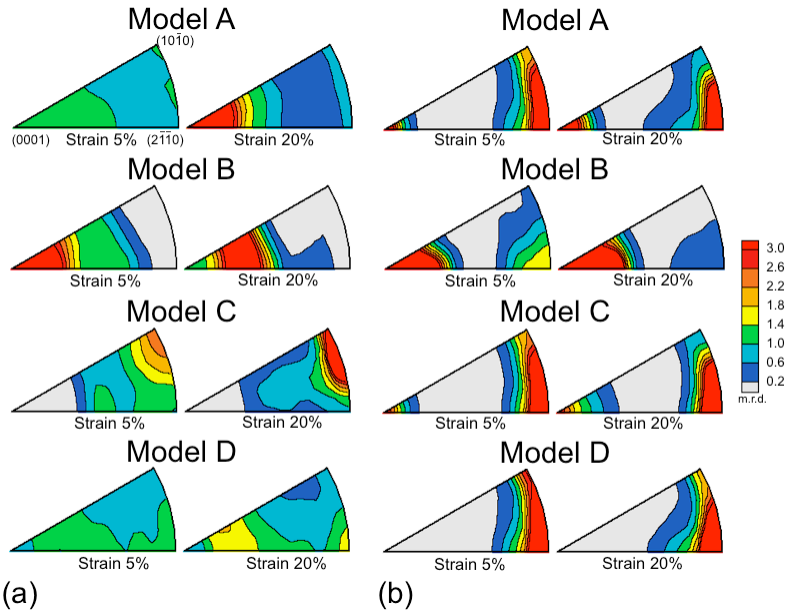

Figure 2.7: VPSC for (a) for a random initial OD and (b) an initial extruded wire texture. In model A, only basal slip is active. Model B has a combination of basal slip and tensile twinning activated. Model C is modeled with basal slip and compressive twinning. Model D uses a combination of basal and prismatic slips

.

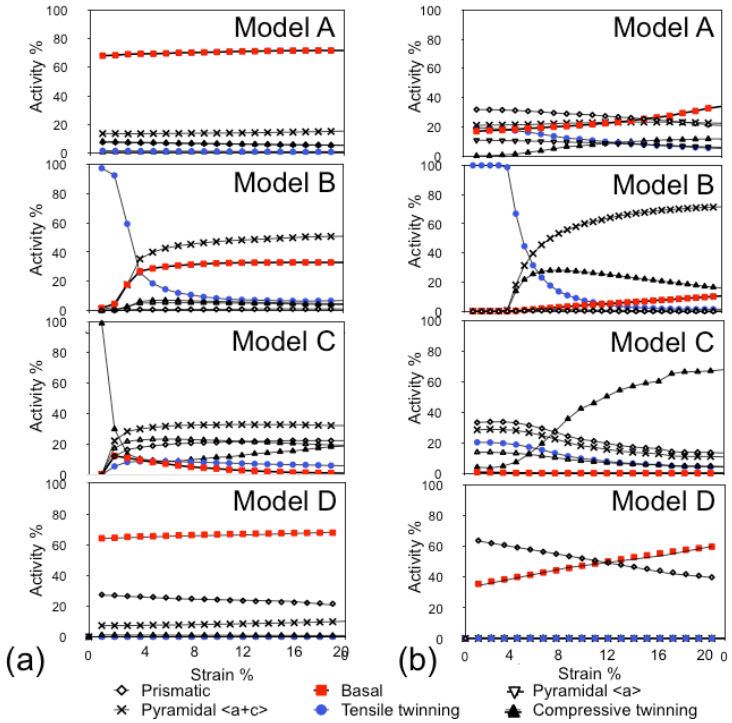

Figure 2.8: Relative activity (%) of different deformation mechanisms are plotted as a function of axial strain % for simulations using models A-D (Table 2.2) (a) for a random initial orientation distribution and (b) for an initial wire texture.

Table 2.2: CRSSs and activities (ACT) of different deformation modes for simulations (model A-D in Fig. 2.7). Activities are shown for the start of the simulation (0% strain) and the end of the simulation (20% strain).

Model	Random initial texture (c/a = 1.580)				Extruded wire initial texture (c/a = 1.580)			
	A	**B**	**C**	**D**	**A**	**B**	**C**	**D**
$\{10\bar{1}0\}<\bar{1}2\bar{1}0>$ *prismatic slip*								
CRSS	6	6	6	2	6	6	6	2
Activity (%)								
Start	7.6	0	0.1	27.4	31.8	0	33.2	62.8
5% strain	7.1	0.6	19	25.9	30.7	0	31.3	58.0
20% strain	5.5	1	22.4	21.2	20.9	0.1	13.2	32.1
$(0001)<2\bar{1}\bar{1}0>$ *basal slip*								
CRSS	2	5	5	1	2	5	5	1
Activity (%)								
Start	68.1	1.7	0.3	64.2	17	0	0.6	35.6
5% strain	69.4	28.8	8.4	65.5	18.9	0	0.1	41.5
20% strain	71.1	33	1.1	67.9	33.9	6.6	0	66.8
$\{10\bar{1}1\}<\bar{1}2\bar{1}0>$ *pyramidal slip*								
CRSS	6	6	6	3	6	6	6	3
Activity (%)								
Start	8.2	0.2	0.2	1.2	10.8	0	13.7	0.1
5% strain	7.6	5.3	23.3	1.1	10.2	0	12.3	0.1
20% strain	5.6	3.9	19.4	0.8	5.9	0.6	4.4	0
$\{10\bar{1}\bar{1}\}<\bar{1}\bar{1}23>$ *pyramidal slip*								
CRSS	6	6	6	3	6	6	6	3
Activity (%)								
Start	13.7	0.7	0.2	7.3	21	0	28.4	0.5
5% strain	13.6	39.9	31.1	7.6	21.5	0.7	26.6	0.5
20% strain	15.2	50.8	32.3	10.1	22.4	67.2	10.6	0.3
$\{10\bar{1}2\}<\bar{1}011>$ *tensile twinning*								
CRSS	6	1	6	6	6	1	6	6
Activity (%)								
Start	1.7	97.4	0	0	19.4	100	20.2	0
5% strain	1.5	18.5	8.9	0	16.3	98.7	17.1	0
20% strain	0.9	6.8	6	0	5.2	2.6	4	0
$\{2\bar{1}\bar{1}2\}<2\bar{1}\bar{1}3>$ *compressive*								
CRSS	6	6	1	6	6	6	1	6
Activity (%)								
Start	0.7	0	99.3	0	0.1	0	3.9	0
5% strain	0.8	6.9	9.4	0	2.4	0.6	12.6	0
20% strain	1.0	4.6	18.8	0	11.7	22.9	67.8	0

2.5.1.1) Random Initial Texture

Basal slip (Model A) produces a maximum at (0001) and indeed basal slip is the only significantly active system in the random initial texture (Figs. 2.7a and 2.8a). Tensile twinning (Model B) also produces a maximum near (0001) though slightly displaced. This texture develops immediately at low strains. In this case, twinning is active initially and once favorable orientations are twinned, deformation proceeds by pyramidal and basal slip. For compressive twinning (Model C) a maximum near $(10\bar{1}0)$ develops. Again, twinning is initially active, followed by pyramidal and prismatic slip. If both basal and prismatic slips are active, and twinning is suppressed (Model D), a relatively weak bimodal texture develops, with concentrations near (0001) as well as near $(2\bar{1}\bar{1}0)$. Orientations closer to (0001) deform mainly by basal slip and rotate towards (0001), while orientations at high angles to (0001) deform by prismatic slip and rotate towards $(2\bar{1}\bar{1}0)$.

2.5.1.2) Extruded wire initial texture

Most grains are unfavorably oriented for basal slip (Model A) in the initial wire texture (5s. 2.5b and 2.6b). A few grains rotate towards (0001) but most remain at high angles. Many slip systems are active. For tensile twinning (Model B), there is a spike in twinning activity that rotates grains with *c*-axes at high angles to the compression direction towards (0001). This is followed by pyramidal slip. Pyramidal slip is active because most grains are unfavorably oriented for prismatic and basal slip. Compressive twinning (Model C) cannot occur because most grains are unfavorably oriented and thus strain is accommodated by other systems. Finally, for basal and prismatic slip (Model D), these two systems dominate and compete. Rotations do not proceed towards (0001) but converge at $(2\bar{1}\bar{1}0)$.

This documents the importance of the original orientation distribution, especially for cases where twinning is subordinate. Texture patterns for Model A and Model D are entirely different. Basal and prismatic slip favor grains with *c*-axes inclined at intermediate angles (~45°) and if these orientations do not exist, texture evolution is impeded. These simulations are now compared with experimental results of different hcp metals.

2.5.2) Osmium

Model B (Fig. 2.7a) agrees best with the low-pressure texture for Os at 4 GPa (Fig. 2.5b, no. 2), and resembles the high-pressure texture at 58 GPa (Fig. 2.5b, no. 5). At as little as 4 GPa, mechanical twinning on $\{10\bar{1}2\}<\bar{1}011>$ produces tensile strain parallel to *c*-axis and yields a texture maximum near (0001). It can be concluded that $\{10\bar{1}2\}<\bar{1}011>$ tensile twinning is a significant mechanism in Os, accommodating plastic deformation, already at low pressure/low strain. With increasing strain, the texture does not significantly strengthen.

2.5.3) Zinc

Zn, where the *c/a* decreases rapidly with increasing pressure (Takemura 1997; Fast et al. 1997), provides a dramatic example of the significance of twinning in hcp metal deformation at high pressures. The prevalent twin system goes from being compressive twinning $\{10\bar{1}2\}<10\bar{1}\bar{1}>$ to tensile twinning $\{10\bar{1}2\}<\bar{1}011>$ as *c/a* becomes smaller than the critical value of $\sqrt{3}$ (see Yoo 1981, and Fig. 2.9). Model A (Fig. 2.7a) most closely resembles the experimental texture of Zn at 10 GPa (Fig. 2.5a, no.2), indicating that basal slip is dominant (Fig. 2.8a). As the *c/a* ratio crosses below the critical value at a pressure of 15 GPa, $\{10\bar{1}2\}<\bar{1}011>$ tensile twinning (model B, Fig. 2.5a) reorients the crystals and strengthens the (0001) texture (Fig. 2.5a, no. 3).

Additional models with different *c/a* ratios were generated to explore the effect of tensile twinning on Zn texture evolution (Fig. 2.9). The parameters used in model B of Fig. 2.7 were modified for different *c/a* ratios of Zn obtained from tDAC experiment and updated their corresponding characteristic shear (*g*). Note that *c/a* = 1.856 for model B_1, *c/a* = 1.741 for model B_2, *c/a* = 1.710 for model B_3, *c/a* = 1.641 for model B_4. A new set of CRSS parameter was also employed (CRSS for basal slip is 2, CRSS for tensile twinning is 1, the rest are 6). At *c/a* >1.732, models B_1 and B_2 show a maximum in the distribution of compression axes near (20) and (100). This texture pattern is controlled by compressive twinning on $\{10\bar{1}2\}\langle 10\bar{1}1\rangle$. As the *c/a* ratio crosses below 1.732, $\{10\bar{1}2\}$ twinning reverses the shear direction to $\langle 10\bar{1}1\rangle$ and becomes tensile twinning, which leads to a maximum near (0001) (models B_3 and B_4 in Fig. 2.9). Model B_4 corresponds to the strongest texture of Zn at 25 GPa (Fig. 2.5e, no. 5). The observations confirm the role of $\{10\bar{1}2\}\langle 10\bar{1}1\rangle$ tensile twinning in Zn texture development at high pressure.

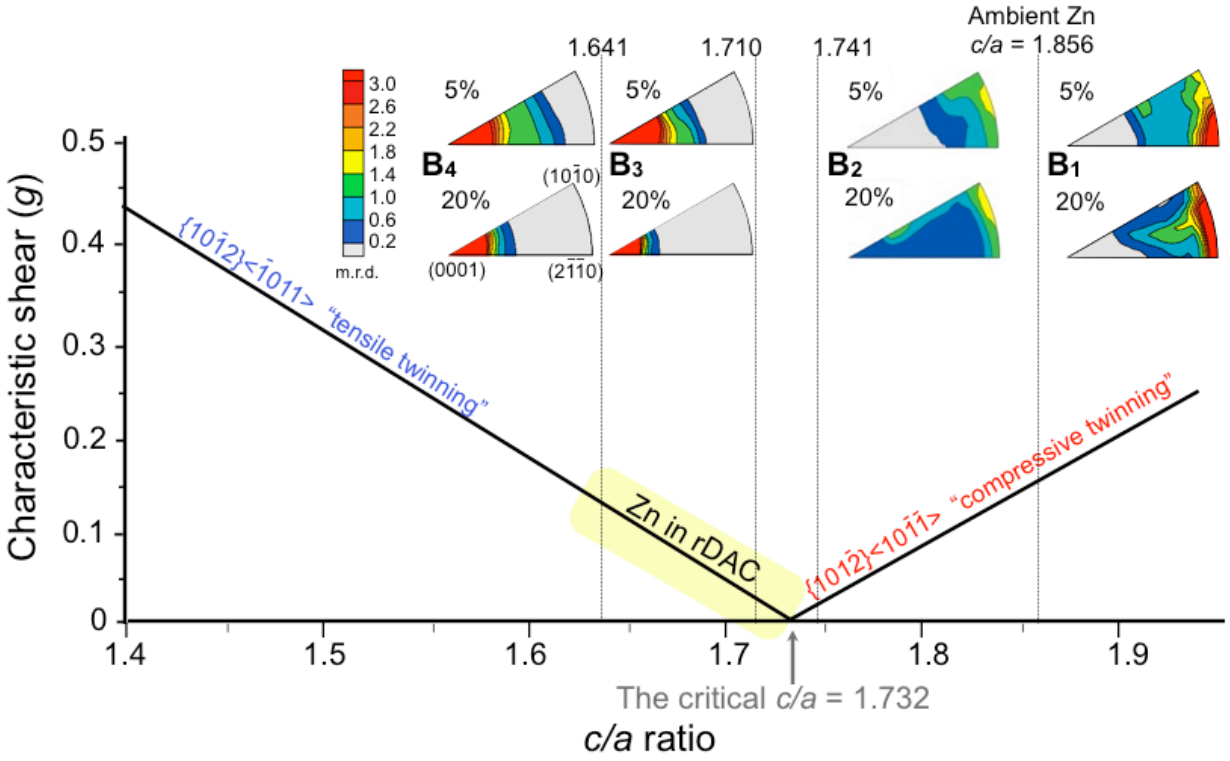

Figure 2.9: Additional VPSC simulations for Zn with different *c/a* ratios. The CRSS are listed in Table 2.2. Models in the top row are generated with 5% strain and models in the bottom row are simulated with 20% strain.

2.5.4) Cadmium

Cd behaves similarly to Zn as they both have high *c/a* ratios (Fig. 2.7). Model A in Fig. 2.8a most closely resembles to the (0001) texture in Cd during compression and axial shortening to 52% strain (Fig. 2.5c, no.1 and 2). As decompression and strain reversal continue, the texture weakens slightly but remains near (0001) (Fig. 2.5c, no. 3). The simulations infer that the texture in Cd is mainly controlled by $\{0001\}\langle 2\bar{1}\bar{1}0\rangle$ basal slip. Tensile twinning might not be active in Cd at low pressure, as the *c/a* ratio obtained from the D-DIA experiment did not cross below the 1.732 threshold, contrary to Zn.

2.5.5) Hafnium

Since Hf has initially a wire texture, the experimentally measured wire texture is used as starting distribution for the plasticity simulations (Figs. 2.7b, 2.8b). Hf crystals reorient and immediately develop the IPF maximum near (0001) (Fig. 2.5d, no. 2) when applying pressure to 4 GPa and axial shortening to 8%. This texture is activated by $\{10\bar{1}2\}<\bar{1}011>$ tensile twinning (model B in Fig. 2.7b), which produces a (0001) maximum parallel to the compression direction. The simulations reassure that $\{10\bar{1}2\}<\bar{1}011>$ tensile twinning is a main deformation mechanism in Hf at high pressure. Upon decompression and strain reversal to ambient condition, texture remains strong but developed the IPF maximum near $(10\bar{1}0)$ (Fig. 2.5d, no.5). As Hf crystals detwin, their *c*-axes rotate away from the compression direction. Immediate switch from compression (negative *t*) to tension (positive *t*) during strain reversal (Table 2.1) and corresponding detwinning are also observed during axial shortening and lengthening cycle (Fig. 2.10).

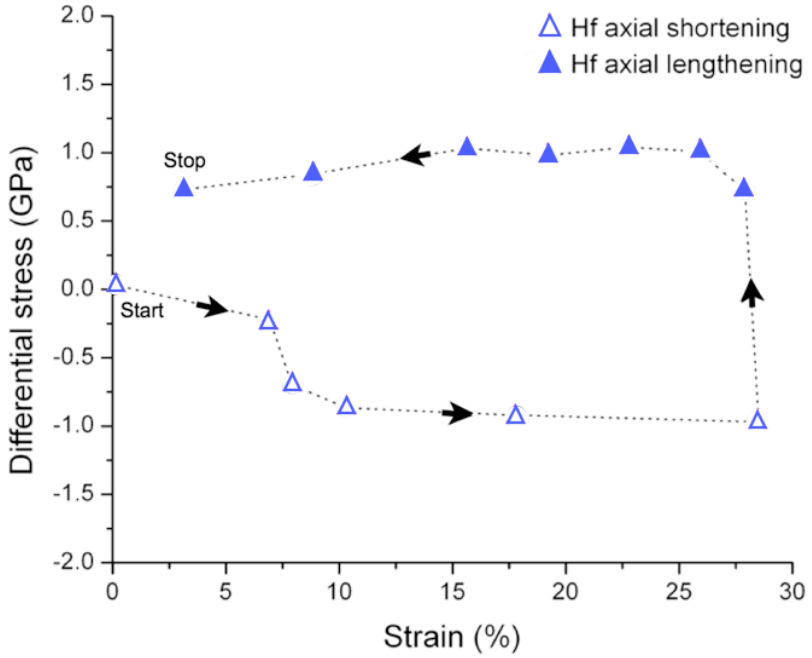

Figure 2.10: A diagram illustrates changes of differential stress upon an axial shortening and lengthening cycle in D-DIA experiment of Hf at ambient temperature.

In the second run of the Hf experiment, resistive heating was incorporated to examine texture development at high temperature. The starting Hf wire has a relatively weaker texture (3.00 m.r.d) than that in the first run (7.72 m.r.d.). As the sample was simultaneously heated to 700 K and applied compression as well as axial shortening, the IPF maximum developed near $(2\bar{1}\bar{1}0)$ (Fig. 2.5e, no. 2-4), indicating that the *c*-axes are inclined at intermediate angles to the compression direction. The $(2\bar{1}\bar{1}0)$ texture agrees with model D in Fig. 2.7b, which is mainly controlled by $\{0001\}<2\bar{1}\bar{1}0>$ basal slip and $\{10\bar{1}0\}<\bar{1}2\bar{1}0>$ prismatic slip (Fig. 2.8b). Interestingly, the IPF maximum remains near $(2\bar{1}\bar{1}0)$ during decompression and strain reversal (Fig. 2.5e, no.5). These observations suggest that mechanical twinning is not active at high temperature.

The maximum texture in Zn (Fig. 2.5a), Os (Fig. 2.5b) and Cd (Fig. 2.5c) is slightly displaced from (0001), which can be characteristic of tensile twinning, as shown in model B at 20% strain (Fig. 2.7a). Clausen et al. (2008) and Agnew et al. (2003) suggest that a displacement of the IPF maximum after dominant basal slip and tensile twinning of hcp metals is influenced by pyramidal slip <*a*+*c*>, rotating the *c*-axis away from the compression axis. Twinning causes a large number of grains to reorient the *c*-axis and align it with the compression axis, which is a plastically hard orientation. The presence of twin boundaries may also serve to inhibit the movement of dislocations and increase the yield strength. This is supported by high differential stresses observed in the Os sample. However, at high temperature, texture in Hf is controlled by {0001}<$2\bar{1}\bar{1}0$> basal slip and {$10\bar{1}0$}<$\bar{1}2\bar{1}0$> prismatic slip systems. It is evident that tensile twinning is an unfavorable mechanism to accommodate plastic strain at high temperature.

Transmission Electron Microscopy (TEM) would be necessary to further characterize the microstructure, particularly the penetration of twin boundaries by dislocations and the misorientation angle between the twinned crystals and surrounding grains. Dislocation and twin interactions in Zr and Hf have been observed with the TEM (Proust et al. 2007), as the twinned regions produce strong contrast variations. If prismatic and pyramidal slips are activated significantly, i.e. CRSSs are around 3, the texture pattern does not conform to experiment data. It is revealing to look at deformation system activities (Fig. 2.8). For slip, activity rates remain fairly constant, at least at moderate strains, and activities correspond to the CRSS inputs. If twinning is active, it dominates at low strains and reorients favorably oriented crystals immediately. But once crystals are twinned twinning activities decline rapidly (Fig. 2.7, Fig. 2.8 Models B and C). Twinning produces a rapid but moderate and stable preferred orientation. Slip, on the other hand, steadily increases texture strength. In addition, the fact that a relatively large volume fraction of crystals needs to reorient in order to accommodate a rather modest amount of shear strain, means that slip is always a player, in the parent and in the twin, to accommodate the remaining imposed deformation.

2.6) CONCLUSIONS

Hexagonal metals, deformed in axial compression at ambient temperature and high pressure, develop an alignment of *c*-axes near the compression axis. Textures in Zn and Cd initially develop by {0001}<$2\bar{1}\bar{1}0$> basal slip and at higher pressure slip may be accompanied by {$10\bar{1}2$}<$\bar{1}011$> tensile twinning when the *c*/*a* ratio decreases below the critical value (*c*/*a* = 1.732). In contrast, texture in Os and Hf at ambient temperature develops early due to a dominant role of {$10\bar{1}2$}<$\bar{1}011$> tensile twinning, with some degree of basal slip. At elevated temperature (700 K), tensile twinning is suppressed and texturing in Hf is due to combined basal and prismatic slip. Twinning is activated as soon as compression is applied, with rapid changes in texture pattern. However once twinning of favorably oriented grains has occurred, the mechanism stops and subsequent deformation takes place by slip. At high temperature twinning is suppressed and all deformation occurs by slip. Under all conditions, basal slip appears to be the main deformation mechanism in hcp metals at high pressure and temperature.

CHAPTER 3

LATTICE PREFERRED ORIENTATION OF POSIDONIA SHALE WITH DIFFERENT THERMAL HISTORY

3.1) INTRODUCTION

The LPO of mineral and anisotropic pore space are important contributors to elastic and seismic anisotropy (Vernik and Nur 1992; Hornby 1994; Sayers 1994). Studies by Vernik (1993, 1994) suggest that the intrinsic anisotropy of organic-rich shales is further enhanced by bedding-parallel microfractures that were created during hydrocarbon generation. Several studies, which rely on traditional X-ray pole figure goniometry (e.g. Curtis et al. 1980; Sintubin, 1994; Ho et al. 1995; Ho et al. 1999; Aplin et al. 2006; Valcke et al. 2006; Day-Stirrat et al. 2008a,b) and on synchrotron X-ray diffraction techniques (e.g. Lonardelli et al. 2007; Wenk et al. 2008; Voltolini et al. 2009; Wenk et al. 2010), have supplied evidence that the LPO of clay minerals increases with increasing clay content, burial, and diagenesis. Given the diversity of shales and the dependence of LPO on provenance, clay mineralogy, and bioturbation, the variation of mineral preferred orientation cannot be attributed to a single factor.

In this study, shales of a single formation but with a different thermal history were measured to investigate whether differences in temperature has affected the LPO patterns of constituent clay minerals. A synchrotron X-ray diffraction technique was used to characterize composition, LPO, and microstructure of four Lower Jurassic Toarcian Posidonia Shale samples retrieved from the Hils Syncline in northern Germany. The samples vary in vitrinite reflectance (R_o) from 0.68% in the SE to 1.45% in the NW (Littke and Rullkötter, 1987; Littke et al. 1988). The variation indicates differences in local temperature history due to either a local igneous intrusion or a complex burial history (e.g. Leythaeuser et al. 1980; Rullkötter et al. 1988; Petmecky et al. 1999). Microstructures at were also studied by scanning electron microscopy (SEM).

3.2) SAMPLES

The Lower Jurassic Toarcian Posidonia Shale is the main hydrocarbon source rocks in the North Sea offshore Netherlands and in northern Germany (Rullkötter et al. 1988; Littke et al. 1991, 1997, Doornenbal and Stevenson, 2010 and references therein). Posidonia Shale is generally dark grey, laminated, and bituminous, and was deposited in a low energy and oxygen-depleted condition. The shales represent peak transgression during a sea-level highstand and correspond to a global oceanic anoxic event, dating back approximately 176 Ma (Doornenbal and Stevenson, 2010).

In the Hils Syncline of Northern Germany, properties of the Posidonia vary considerably depending on the burial depth, compaction, and local history (Littke and Rullkötter, 1987; Littke et al. 1988). The low energy environment rocks from the same sedimentary sequence are laterally

continuous, with main variability caused by organic content as a function of depth and stratigraphy (Littke et al. 1991, Rullkötter et al. 1988). Significant lateral variation in maturity of the organic content of Posidonia Shale retrieved at the Hils Syncline is due to local history of the Lower Saxony Basin (Rullkötter et al. 1988). Lateral differences in thermal maturity are believed to be caused by deep Cretaceous igneous intrusions (Deutloff et al. 1980; Leythaeuser et al. 1980; Rullkötter et al. 1988), or, as was demonstrated for structures slightly west of the area of interest, by a combination of deep burial, substantial subsidence, and intense uplift processes of individual structures (Petmecky et al. 1999; Muñoz et al. 2007). The cause of the thermal anomalies is still under discussion (Kus et al. 2005; Bilgili et al. 2009).

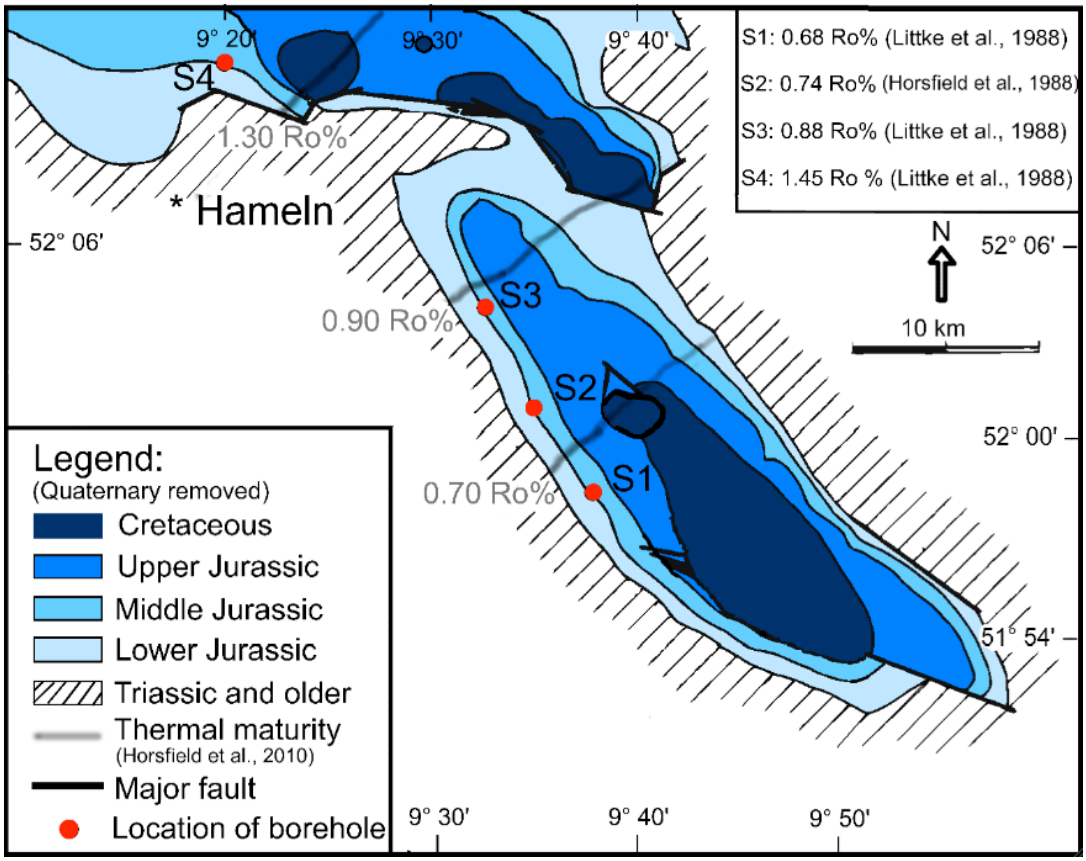

Figure 3.1: A geological map of Posidonia Shale in the Hils syncline, indicating samples (S1-S4) used in this study (modifed from Littke et al. 1988). Different thermal maturity (Ro%) contours (after Horsfield et al, 2010) are also displayed.

Posidonia Shale were retrieved from four different wells about 10-20 km apart (Mann 1987, Fig. 3.1) of the Hils syncline. The samples were obtained from the approximately 40 m thick Toarcian formation at a depth of approximately 50 – 60 m. No evidence has been found for significant variation in depositional environment over the sampled area (Littke et al. 1988), but faulting has been diagnosed at the location of S4, leading to a locally higher porosity (Mann, 1987). The maturity of the organic matter, defined by vitrinite reflectance (R_o) (Tissot and Welte, 1984), ranges from 0.68%R_o to 1.45% R_o (Littke and Rullkötter, 1987; Littke et al. 1988; Bernard et al. 2011). As inferred from mercury injection capillary pressure (MICP), the porosity of shales with similar thermal maturity obtained from the same set of wells is generally low, ranging from 4% to 10% (Mann, 1987), with porosity decreasing as a function of maturity.

3.3) EXPERIMENTAL TECHNIQUES

3.3.1) Scanning Electron Microscopy (SEM)

A polished slice of sample S4 was coated with carbon and examined with a Zeiss Evo MA10 low vacuum SEM, equipped with an EDAX Energy-Dispersive Spectroscopy (EDS) system. The SEM was operated with an accelerating voltage of 30 kV and a probe current of 20 nA to collect images. The brightness variation of backscattered (BE)-SEM images, ranging from low (black) to high (white) is due to the contrast in atomic number, with high atomic numbers giving white. The EDAX Genesis Imaging/Mapping software was used to map different elements e.g. Al, Si, O, Fe, Mg, and K and identify minerals such as pyrite and illite.

3.3.2) High-Energy Synchrotron X-ray Diffraction

Four shale samples were first embedded in low-temperature hardening epoxy resin in plastic containers to produce epoxy cylinders, around 2 cm in diameter. The cylinders were then cut and polished into 2 mm slices. A monochromatic synchrotron X-ray beam, with a size of 1mm in diameter and a wavelength of 0.10779 Å (115 keV), was used to collect diffraction patterns at the BESSRC 11-ID-C beamline of the APS (Fig. 3.2). The sample was mounted on a goniometer, translated parallel to the goniometer-axis over 5 different spots in 2 mm increments to obtain a representative sample volume. The sample was also tilted around the goniometer-axis from -45° to 45° in 15° increments to obtain an adequate pole figure coverage (Fig. 3.2, inset). Diffraction patterns were recorded for 60s with a Mar345 detector, positioned at about 2 m from the sample. The 2θ angles range from 0° to 4.6° in each diffraction pattern.

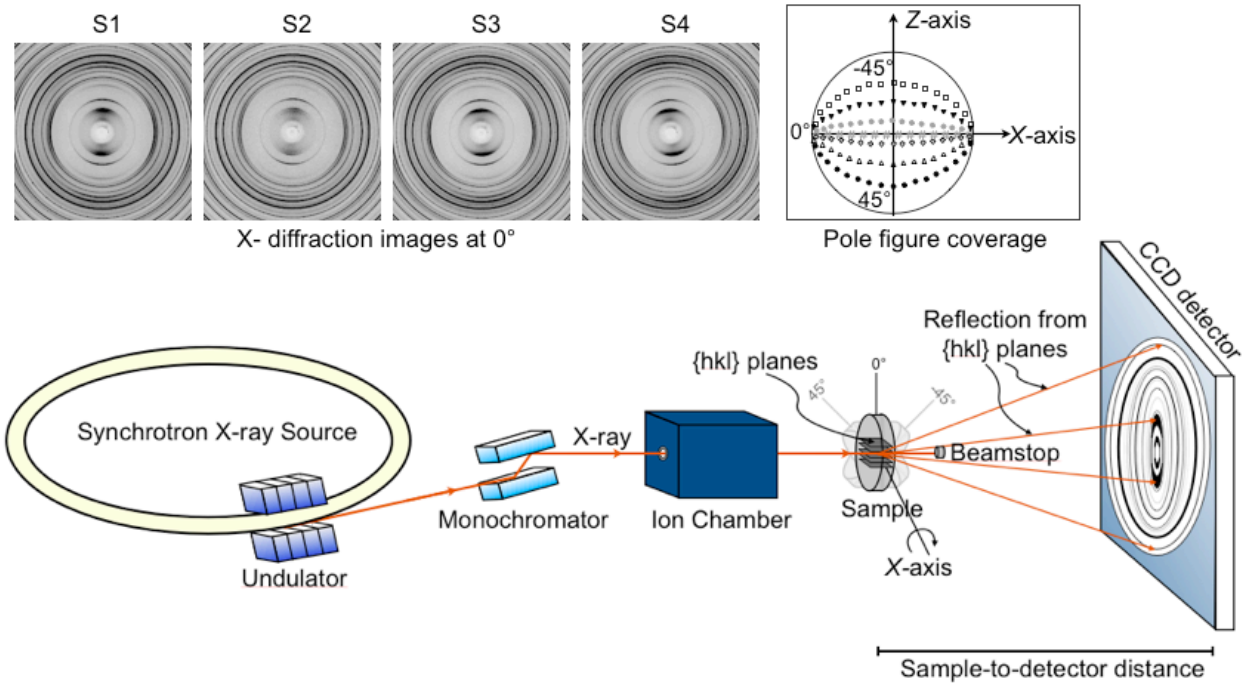

Figure 3.2: A setup of hard synchrotron X-ray diffraction experiment at beamline 11-ID-C of APS.

The instrument geometry (sample-detector distance, beam center, and image plate tilt) was first calibrated with a CeO_2 powder standard. The diffraction images were integrated from 0° to 360° azimuth over 10° intervals to produce 36 spectra, representing distinctively oriented lattice planes.. A Q range of 0.37-3.70 $Å^{-1}$ (*d*-spacing 1.80-16.98 Å) was used in the Rietveld refinement.

Seven major minerals were recognized in the samples. Crystallographic structures of clays were obtained from the American Mineralogist Database (Downs and Wallace, 2003); specifically triclinic kaolinite from Bish (1993), monoclinic illite-mica from Gualtieri (2000), and monoclinic illite-smectite, based on a muscovite-phengite composition, from Plançon et al. (1985), whereas quartz, calcite, feldspar, pyrite, and dolomite structures were imported from the database contained in MAUD. For the Rietveld refinement of monoclinic phases the first setting (with *c* as unique axis) has to be used, but for representation, the more conventional second setting (with *b* as unique axis) is used here. The monoclinic phyllosilicates (001) is thus the cleavage plane. The spectra were refined with background polynomial functions, scale parameters, phase volume fraction, and lattice parameters, but atomic coordinates were kept constant. The peak shapes and widths were modeled by refining anisotropic crystallite size and microstrain. The LPO was computed by the EWIMV algorithm (Matthies and Vinel, 1982), using 10° resolution for the orientation distribution (OD) determination, without imposing sample symmetry.

The OD, which defines the crystallite orientation relative to sample coordinates, was imported into the BEARTEX software (Wenk et al. 1998) to further process the orientation data. The OD was also smoothed with a 7.5° filter to minimize artifacts from the orientation cell structures. In the final step, the sample was rotated so that pole figures are defined in respect to the bedding plane. The pole densities are expressed as multiples of random distribution (m.r.d.), where a value of 1 corresponds to a random or isotropic distribution and a high value in a particular direction suggests a strong orientation along that direction. Pole densities are normalized in such a way that the integral over the whole pole figure is 1.0. The basal plane (001) in clay minerals is most significant, thus the (001) pole figures are displayed, with the bedding plane normal in the center.

3.4) RESULTS

Backscattered SEM images (Fig. 3.3a) show complex microstructures of very fine-grained clays, calcite veins, coarse-grained quartz, and pyrite. Pyrite is present as euhedral crystals and as fine-grained clusters of small octahedra in a framboid structure (<5 μm) (Fig. 3.3b). Calcite-filled fractures are clearly aligned with the well-developed horizontal bedding planes. Very fine-grained clays are abundant in the matrix, in particular Fe- and Mg-containing detrital illite, which was verified by EDS elemental maps (Fig. 3.4a-f).

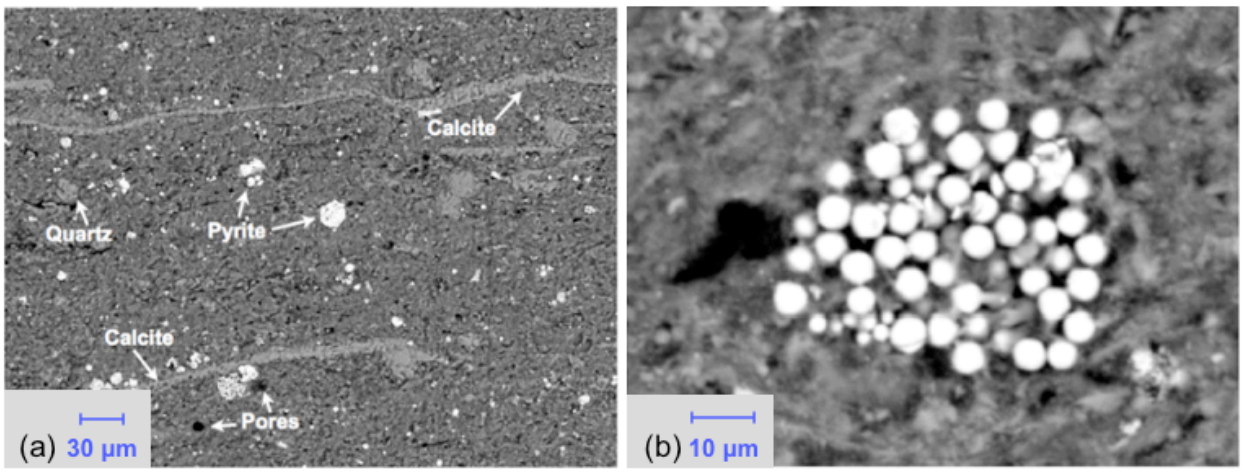

Figure 3.3: Backscattered SEM images of sample S4 illustrating (a) microstructure of component minerals and (b) the presence of pyrite framboid structure.

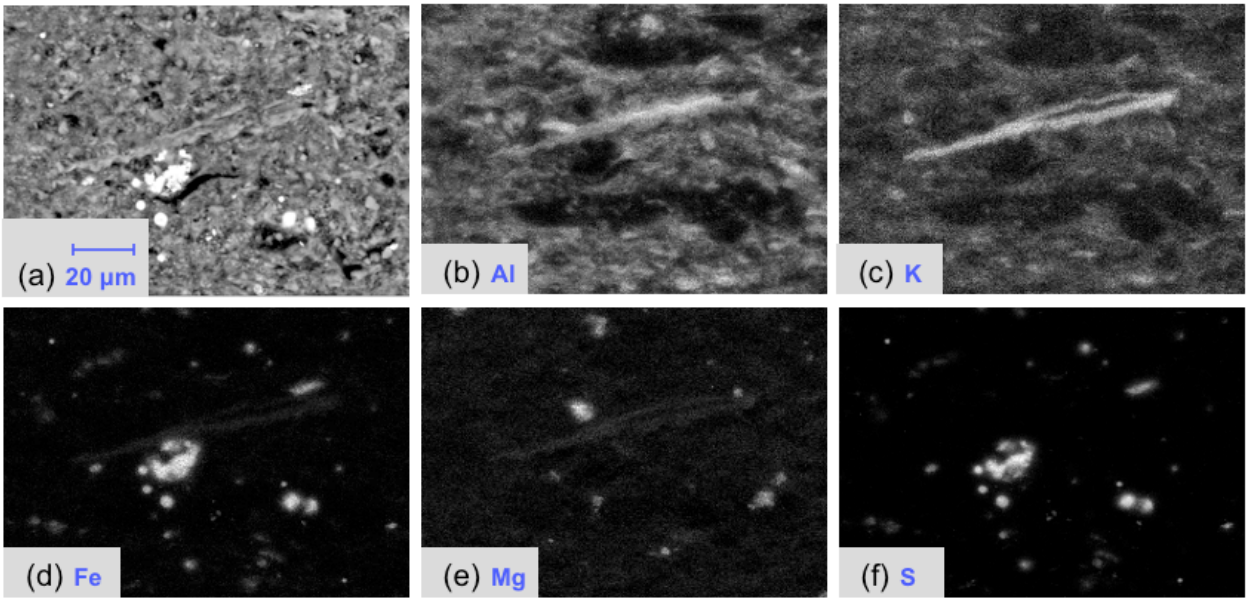

Figure 3.4: Chemical maps of various elements indicate the presence of Fe- and Mg-containing illite.

A summary of different phase proportions in weight fractions and lattice parameters, based on the Rietveld refinement, is given in Tables 3.1-3.2. In general, calcite (31-44 vol%) and the illite-group (24-40 vol%) dominate the composition in all samples. The amount of other phases such as quartz, kaolinite, pyrite, and albite are fairly similar. Dolomite was only observed in high maturity samples S3 (0.88% R_o) and S4 (1.45% R_o). The weight fractions of different phases in this study are consistent with the proportions reported by Mann et al. (1986) and Mann (1987). The broad diffuse peak of illite-smectite (inset of Fig. 3.5) indicates a low degree of crystallinity, small crystallite size, and stacking disorder.

Table 3.1: Quantitative mineral proportions in wt% (top row) and vol% (bottow row) fractions extracted from the Rietveld refinement of S1, S2, S3 and S4 samples.

Sample	Kaolinite	Illite-smec	Illite-mica	Calcite	Quartz	Albite	Pyrite	Dolomite
S1	7.95	11.76	11.24	43.82	16.21	2.30	6.71	-
	8.45	13.24	11.06	44.34	16.82	2.41	3.68	
S2	10.56	12.50	17.48	37.25	16.66	0.99	5.59	-
	11.20	13.76	17.08	37.64	17.27	1.12	3.06	
S3	5.91	22.06	14.79	33.18	16.58	2.49	4.49	1.50
	6.24	23.18	14.49	33.48	16.12	2.60	2.44	1.44
S4	5.94	15.52	13.72	38.36	12.91	5.31	5.64	2.62
	6.37	16.94	13.46	38.72	13.36	5.54	3.08	2.51

Table 3.2: Lattice parameters of major phases obtained from the Rietveld refinement. Parameters ofalbite and dolomite are kept constant throughout the refinement (marked with asterisk). Monoclinic phases are displayed in the second setting system.

Phase	Sample	A (Å)	b (Å)	c (Å)	α (°)	β (°)	γ (°)
Kaolinite	S1	5.18(1)	8.98(1)	7.44(1)	92.13(2)	105.06(2)	89.31(1)
	S2	5.15(1)	8.96(1)	7.41(1)	91.86(1)	104.99(1)	89.91(1)
	S3	5.17(1)	8.98(1)	7.43(1)	92.14(1)	104.06(2)	89.29(1)
	S4	5.16(1)	8.97(1)	7.44(1)	92.57(1)	105.10(1)	89.19(1)
Illite-smectite	S1	5.26(1)	8.90(1)	11.62(1)	90.00	100.01(2)	90.00
	S2	5.29(2)	8.94(2)	11.46(1)	90.00	99.87(2)	90.00
	S3	5.31(1)	8.88(1)	10.84(1)	90.00	100.89(2)	90.00
	S4	5.45(1)	8.91(1)	10.89(1)	90.00	100.29(1)	90.00
Illite-mica	S1	5.25(1)	9.06(1)	20.34(1)	90.00	95.09(1)	90.00
	S2	5.20(2)	9.00(3)	20.12(2)	90.00	95.87(1)	90.00
	S3	5.25(1)	9.06(1)	20.34(1)	90.00	95.37(1)	90.00
	S4	5.28(2)	9.03(2)	20.44(2)	90.00	95.24(1)	90.00
Calcite	S1	4.99(1)	4.99(1)	17.06(1)	90.00	90.00	120.00
	S2	4.99(1)	4.99(1)	17.06(1)			
	S3	4.99(1)	4.99(1)	17.05(1)			
	S4	4.99(1)	4.99(1)	17.06(1)			
Quartz	S1	4.91(1)	4.91(1)	5.41(1)	90.00	90.00	120.00
	S2	4.92(1)	4.92(1)	5.40(1)			
	S3	4.92(1)	4.92(1)	5.40(1)			
	S4	4.92(1)	4.92(1)	5.40(1)			
Albite*	S1	8.14	12.79	7.16	94.33	116.57	87.65
	S2						
	S3						
	S4						
Pyrite	S1	5.42(1)	5.42(1)	5.42(1)	90.00	90.00	90.00
	S2	5.42(1)	5.42(1)	5.42(1)			
	S3	5.41(1)	5.41(1)	5.41(1)			
	S4	5.41(1)	5.41(1)	5.41(1)			
Dolomite*	S1	-	-	-	-	-	-
	S2	-	-	-	-	-	-
	S3	4.81	4.81	16.08	90.00	90.00	120.00
	S4	4.81	4.81	16.08	90.00	90.00	120.00

The refined model diffraction spectra (top: Calc) were compared with experimental spectra (bottom: Exp) in Fig. 3.5a, which show a close similarity, indicative of an excellent fit, both in intensities as well as position of diffraction peaks. Figure 3.5b shows the average spectra for the 0° tilt images, with dots for experimental data and a thin solid line giving the calculated fit.

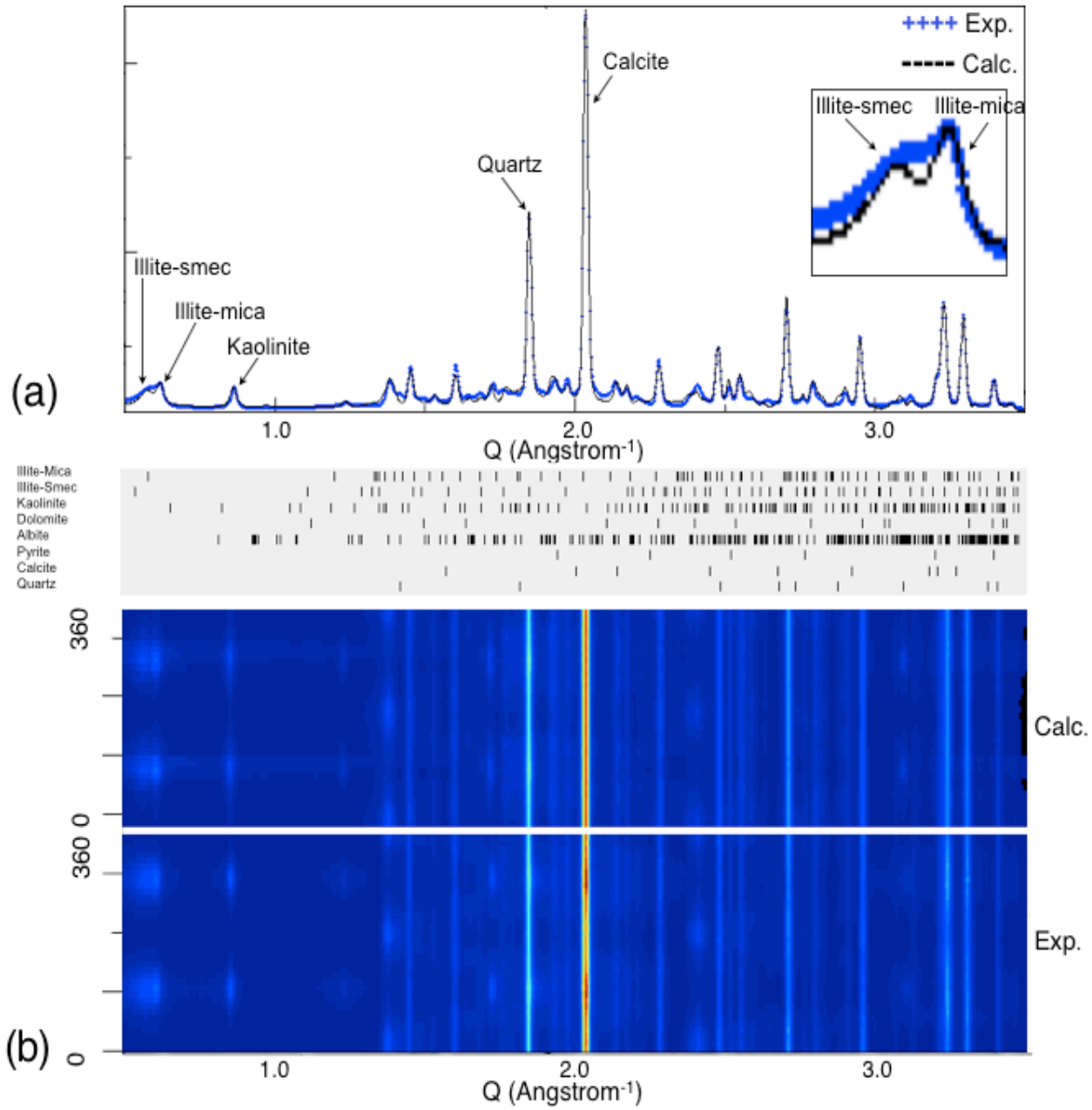

Figure 3.5: A comparison of (a) "unrolled" diffraction spectra of sample S4 between calculated model (top: Calc.) and experimental data (bottom: Exp.) and (b) diffraction peaks in spectrum which display 8 constituent minerals. The variation of intensity along the azimuth are clearly displayed in (a) and they are indicative of texture in for some minerals. The insert in (b) is an enlargement of the Q ~ 0.6 $Å^{-1}$ peak showing the overlapping 002 peaks of illite-mica and illite-smectite. Dotted line is experimental data and solid line is the Rietveld fit extracted.

Pole figures of texture analysis are displayed for kaolinite, illite-mica, illite-smectite, and calcite (Fig. 3.6), with pole densities summarized in Table 3.3. Overall, the degrees of LPO for clay minerals are quite strong (3.7 – 6.3 m.r.d.) whereas orientation of quartz, albite, pyrite, and dolomite are close to random (pole figures are not shown). All pole figures are more or less axially symmetric with the (001) maximum perpendicular to the bedding plane, though no sample symmetry was imposed. Illite-mica, with a sharper (002) diffraction peak at lower *d*-spacing, is generally coarse-grained and had a stronger LPO (4.5 – 6.3 m.r.d.) than fine-grained illite-smectite (3.7 – 4.6 m.r.d.), with some variation between samples. Illite-mica in S3 has the strongest alignment with a (001) maximum perpendicular to the bedding plane of 6.3 m.r.d. Maximum pole densities of kaolinite and illite-smectite are similar in all samples (Fig. 3.6). The (001) minima of clay phases ranges from 0.1-0.5 m.r.d., suggesting a still significant number of randomly oriented grains. Calcite grains also orient their *c*-axes preferentially perpendicular to the bedding plane, but the alignment is much weaker than for clays, ranging between 1.1 to 1.3 m.r.d.

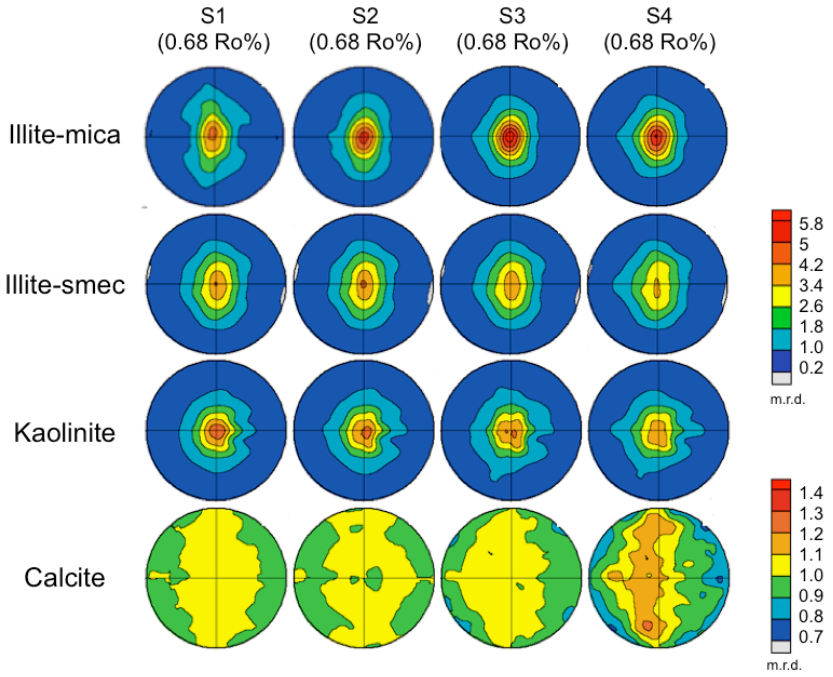

Figure 3.6: (001) pole figures for clay phases and calcite in all samples. Pole densities are expressed in m.r.d. Different scales are used for clays and calcite. Equal area projection on the bedding plane.

Table 3.3: Pole densities of (001) kaolinite, illite-smec, illite-mica, and calcite pole figures for Posidonia Shale expressed in multiples of random distribution (m.r.d.)

Sample	Kaolinite		Illite-smectite		Illite-mica		Calcite	
	Min	Max	Min	Max	Min	Max	Min	Max
S1	0.29	4.38	0.48	4.58	0.16	4.51	0.92	1.07
S2	0.21	4.83	0.44	4.44	0.18	5.35	0.81	1.09
S3	0.29	4.24	0.47	4.27	0.26	6.30	0.89	1.11
S4	0.28	3.86	0.47	3.67	0.27	5.31	0.78	1.25

3.5) DISCUSSION

Care must be taken not to over-interpret the differences observed between the four samples in this study, although they were acquired at similar depths, in the same stratigraphic unit, but possibly in slightly different stratigraphic positions. Small samples on the millimeter and micrometer scale were analyzed, thus the sophisticated analytical methods precluded statistical tests about variability.

3.5.1) Mineralogy

Previous mineralogical studies of Posidonia Shale based on bulk- and fine fraction X-ray diffraction (Mann, 1987; Littke et al. 1988) show no systematic dependence of mineralogy on maturity and exposure to different temperatures. Similarly, based on Rietveld analysis of synchrotron X-ray diffraction images, all samples have similar mineralogical composition, with the illite-group (24-40 vol%) and calcite (31-44 wt%) dominating. No clear evidence for diagenetic transformations of clay minerals was observed. Dolomite in high maturity samples may be indicative of elevated temperatures; small amounts of albite are also present in the high maturity samples, but the relevance of this latter fact is not clear.

3.5.2) Lattice Preferred Orientation

The previous work by Mann (1987) suggests a gradual decrease of porosity with maturity, with an exception noted for the well Haddessen, located in a more faulted area (corresponding to sample S4). The porosity reduction with maturity has been interpreted due to increased cementation and/or an increased depth of burial. Similarly, a trend can be observed as an increase of LPO with maturity in illite-mica for low maturity samples (S1: 0.68% R_o, S2: 0.74% R_o, and S3: 0.88% R_o), with a slight reversal trend for a high maturity sample (S4: 1.45% R_o) (Table 3.3). Illite-mica in S3 has the strongest alignment with a (001) maximum of 6.3 m.r.d. A slight variation in the degree of alignment between illite-smectite and kaolinite was observed in all samples. No trend as function of maturity can be concluded for degree of LPO of kaolinite, except that S4 has the lowest LPO for both of these minerals. Only the LPO of illite-smecite seems to decrease systematically with increase maturity. A considerable portion of clay crystallites in all samples is randomly oriented, expressed by (001) minima of 0.1-0.3 m.r.d. for kaolinite, 0.2-0.3 m.r.d. for illite-mica, and 0.4-0.5 m.r.d. for illite-smectite. The orientation distributions of quartz, albite, dolomite, and pyrite are nearly random, close to 1 m.r.d. Interestingly, calcite has a weak but significant LPO, ranging from 1.1-1.3 m.r.d. in (001) pole figures (Fig. 3.6). Maximum LPO of calcite was observed in S4.

The trends observed in texture of clays, notably the increasing trend of illite-mica, may not be statistically significant, as variability between samples, even taken centimeters apart, can be considerable. The thermal maturity did not seem to be a major effect on the degree of LPO of clays, suggesting that the clay alignment formed early either at the period of consolidation (Baker et al. 1993) or during diagenetic stages (Day-Stirrat et al. 2008b).

3.5.3) Microstructure

Continuous layers of calcite such as the veins illustrated in Fig. 3.3a may be related to cementation. The SEM image of sample S4 shows that calcite mostly aligns as horizontal veins parallel to the bedding plane. Higher-maturity samples (S3 and S4) were exposed to higher temperatures, which may have reduced the organic content and increased the already high carbonate content (Rullkötter et al. 1988). Carbonates in S3 and S4 had been diagenetically altered to dolomite, possibly due to decomposition of organic matters (Slaughter and Hill, 1991).

Contrary to some other shales, for example; from the Qusaiba Formation (clays ~66 vol.%),

Mt. Terri (clays ~70 vol%) (Wenk et al. 2008), and the North Sea (clays ~78%) (Wenk et al. 2010), clays do not dominate the microstructure of Posidonia Shale (35-47 vol%). In general, clay platelets tend to align parallel to the bedding plane but a wide dispersion is present. Organic matter is also often interlayered with clays. The high maturity sample (S4: 1.45%R_o), retrieved from a more tectonically disturbed area, is deformed as illustrated by fractured calcite fragments. The observations imply considerable local stresses, probably associated with compaction of tectonic origin (burial, uplift). The strong deformation in S4 may have contributed to a relatively weak LPO. The observation of deformation in S4, and the presence of late carbonate veins as well as the marginal increase of LPO of illite-mica in S1-S3 as a function of thermal maturity, are consistent with a scenario in which the Posidonia Shale have been buried and uplifted (Petmecky et al. 1999; Muñoz et al. 2007).

3.6) CONCLUSIONS

The focus of this study was a quantification of LPO of clays in samples of Posidonia Shale from the Hils syncline in Northern Germany, subjected to different local histories. The LPO of kaolinite, illite-mica, illite-smectite, and calcite was quantified by synchrotron X-ray diffraction techniques, followed by Rietveld refinement. The degree of LPO of clays and calcite in all four samples with different maturity history is comparable. Kaolinite and illite-mica generally exhibit stronger preferred orientations than microcrystalline illite-smectite. The difference in local history, which causes significant changes in the maturity of organic matter, did not influence the LPO to a large extent and thus it is suggested that most of mineral preferred orientation evolved rather early.

CHAPTER 4

THREE-DIMENSIONAL SHAPE PREFERRED ORIENTATION OF CONSTITUENT PHASES IN SHALES

4.1) INTRODUCTION

Elastic anisotropy of shales is mainly caused by both lattice and shape preferred orientation of constituent phases in the matrix. While LPO in shales can be derived from synchrotron X-ray diffraction experiments (Wenk et al. 2008; Voltolini et al. 2009, Wenk et al. 2010), the three-dimensional (3D) SPO is difficult to quantify due to their multiphase composition and small grain sizes. Besides, the availability of software and their ability to adequately segment components of interests are challenging problems for high spatial resolution investigations. Particularly, the SPO of low density features, including pores, fractures, and kerogen, is of great interest as the information can be used in anisotropic velocity modeling (Hornby et al. 1994).

In this study, two shales were analyzed to determine the SPO in 3D, to explore resolution limitations of three SXMT facilities, and to develop satisfactory procedures for data quantification. The SXMT data were collected from beamline 8.3.2. at the ALS, beamline 2-BM at the APS, and beamline TOMCAT at the SLS. To establish a reasonable comparison, the data were acquired with same parameters, reconstructed, and quantified on the same basis.

4.2) SAMPLES

Two well-characterized shales were selected for this study. The first sample is a Kimmeridge-aged shale from a borehole at 3750 m in the North Sea of England and is referred to as N1. Previous studies suggest that N1 has a porosity of 2.5% and is composed of illite-smectite-mica (35 wt%), quartz (30wt%), kaolinite (22 wt%), pyrite (4 wt%), feldspar (7%), and chlorite (2 wt%) (Hornby, 1998). The LPO was quantified, suggesting strong alignment of (001) clay platelets parallel to the bedding plane with maximum concentrations of 6 multiples of random distribution (m.r.d) for kaolinite, 4 m.r.d. for illite-mica, and 2 m.r.d. for illite-smectite (Wenk et al. 2010).

The second sample is a shale from the Upper Barnett Formation of Late Mississippian age of Fort Worth Basin in Texas from a borehole at 2167 m depth, and is referred to as B1 (Day-Stirrat et al. 2008). A large amount of fine-grained illite-smectite (23.7 wt%) and illite-mica (17.9 wt%) is present in sample B1, along with coarse-grained quartz (44.0 wt%), calcite (6.8 wt%), feldspars (3.1 wt%), dolomite (2.6 wt%), and pyrite (1.5 wt%). The degree of preferred orientation ranges from 2 (illite-smectite) to 7 (illite-mica) m.r.d. (Day-Stirrat et al. 2008).

Both samples were first cut into small rectangular prisms (1 mm x 1mm x 5 mm) with the aid of kerosene as a cooling agent. The small prisms were glued on a glass slide and polished with a file tool into small cylinders (1 mm diameter x 5 mm length) for SXMT experiments.

4.3) EXPERIMENTAL TECHNIQUES

4.3.1) Data Collection

A typical SXMT experimental setup at the synchrotron is illustrated in Fig. 4.1. Each synchrotron facility however has different technical configurations and specifications for equipment (Table 4.1). More details of each beamline are described elsewhere (Parkinson, 2012; Wang et al. 2001; Stampanoni et al. 2006). First, several bright- and dark-field images were collected for X-ray fluctuation correction and background normalization. Bright-field images were acquired with X-ray beam illumination but without the sample in the field of view (FOV) whereas dark-field images were acquired for detector background without the X-ray beam. The correction method is briefly described in the *Data Reconstruction* section.

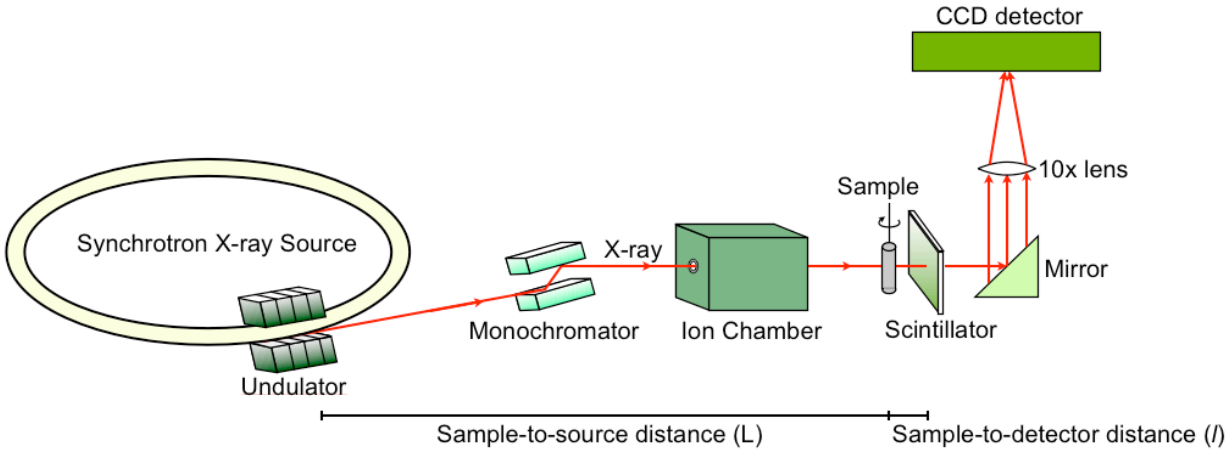

Figure 4.1: A typical SXMT experimental setup at the synchrotron facility.

During the experiment, the cylindrical sample was mounted on a rotational stage with its long axis vertical and centered in the FOV. The sample was rotated in 0.120° incremental steps for a total of 180° during a continuous rotation with a monochromatic X-ray energy of 18 keV (or a wavelength of 0.689 Å). The transmitted X-ray intensity was absorbed by a thin scintillator screen, which converts X-ray to a certain wavelength of the visible light, depending on scintillator material. The visible light was further projected on to a CCD detector through a 10x objective lens. Each raw projection represents a two-dimensional (2D) X-ray attenuation map, which was used to reconstruct a 3D data volume. Raw projections of N1 are similar to those of sample B1, thus only examples of sample N1 from each facility are displayed in Fig. 4.2(a)-(c).

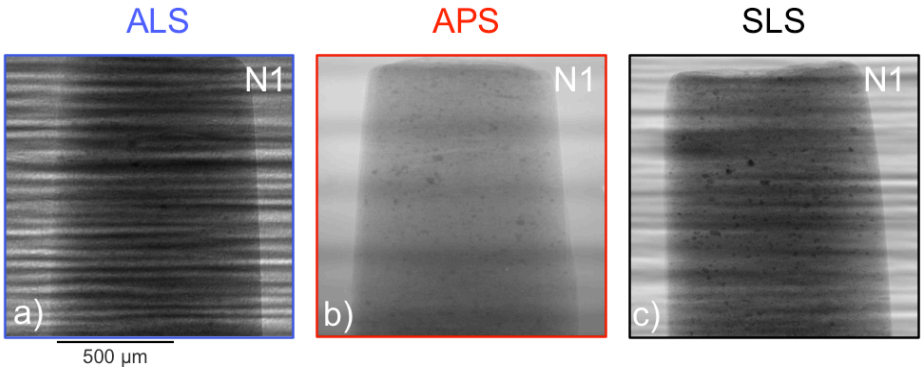

Figure 4.2: Raw projections of sample N1 collected from (a) the ALS, (b) the APS, and (c) the SLS. Horizontal stripes are caused by X-ray beam inhomogeneities due to reflections on different composition of monochromator mirrors.

Table 4.1: Specifications of equipment and acquisition parameters at each synchrotron facility.

	Advanced Light Source (ALS)	**Advanced Photon Source (APS)**	**Swiss Light Source (SLS)**
Beamline	8.3.2	2-BM-B	TOMCAT
X-ray source	Super bend magnet 4.4 Tesla Ring current 500 mA Ring energy 1.9 GeV	Bending magnet 0.6 Tesla Ring current 100 mA Ring energy 7 GeV	Super bend magnet 2.9 Tesla Ring current 400 mA Ring energy 2.4 GeV
Photon source size	220 x 25 μm^2	92 x 26 μm^2	53 x16 μm^2
Beam size at sample	40 mm x 4.6 mm	25 mm x 4 mm	40 mm x 4 mm
Beam flux	~10^2 hv/sec/μm^2	~10^2 hv/sec/μm^2	6.8.10^5 photons/sec/μm^2
Monochromator type	Multilayer (W/B4C), wide band pass ~1%	Double crystal multilayer, unfocussed	Double crystal multilayer (DCMM), bandwidth 2-3%
Monochromator-to-source distance	14 m	27.4 m	7 m
Sample-to-source distance	20 m	50 m	25 m
Sample-to-detector distance	15 mm	6 mm	5 mm
Scintillator type	Single crystal CsI doped with Tl (wavelength ~550 nm)	Single crystal LuAG doped with Ce (wavelength 535 nm)	Single crystal LuAG doped with Ce (wavelength 535 nm)
Scintillator thickness	35 μm	50 μm	20 μm
Detector type	CCD: Cooke PCO 4000	CCD: CoolSNAP *K4*	CCD: PCO2000
Detector resolution	4008 x 2672 (14-bit)	2048 x 2048 (14-bit)	2048 x 2048 (14-bit)
Objective len	Mitutoyo 10x (NA = 0.27)	Zeiss Axioplan 10x (NA = 0.20)	Olympus Uplapo 10x (NA = 0.40)
Pixel size (microns)	0.88 x 0.88	0.72 x 0.72	0.74 x 0.74
Exposure time (ms)	1500	200	200
Angular increment (degree)	0.120	0.120	0.120
Projection images	1500	1500	1500
Bright-field images	12	20	200
Dark-field images	5	20	20

4.3.2) Data Reconstruction

In general, each beamline uses different software for SXMT data reconstruction; for example, beamline 8.3.2 relies on Octopus software (Dierick et al. 2004), beamline 2-BM of the APS and beamline TOMCAT of the SLS use their in-house developed applications with a code based on the Gridrec algorithm and Fast Fourier Transforms (FFTs) (Dowd et al. 1999; De Carlo et al. 2004; Hintermüller et al. 2010). Each software has its own advantages and disadvantages but the analysis of software is not the purpose of this study. The data reconstruction was done at the ALS, thus only Octopus software was used to establish a reasonable comparison of data quality.

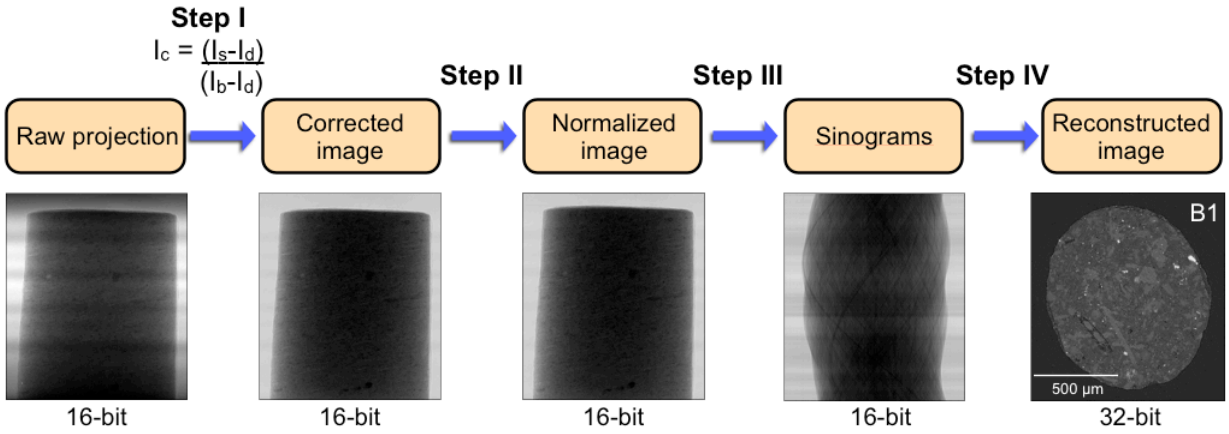

Figure 4.3: A workflow of reconstruction steps in the SXMT experiment

Reconstruction involves multiple steps of data processing as shown in Fig. 4.3. In step I, raw projections were corrected with background images (bright- and dark-field) to remove smearing effect on sharp details (or artifacts), resulting from X-ray beam fluctuation and defects in monochromator, scintillator, objective lens, and detector. The following method (Wang et al. 2001) was used to correct images:

$$I_c = \left[\frac{I_s - I_d}{I_b - I_d} \right]$$

where I_c is the corrected image, I_b is the bright-field image, I_d is the dark-field image, and I_s is the raw projection of sample. The corrected images were normalized in step II by choosing a region of the images where contains no sample, and finding the average value in that region to produce same grayscales for all images in the dataset. In step III, the normalized data was rearranged into a sinogram, which contains information of all projection angles of a projection horizontal line. A few concentric rings were observed due to defective pixels in the detector that are present at the same coordinates in all projections (Dierick et al. 2004). These artifacts were thus removed by a minimal level of median filter (level 1). The ring filter determined the mean of pixel value in each column of sinogram and compared to its eight neighboring pixels. The pixels in the column that have a higher deviation than the chosen level were then replaced by multiplying with a correction factor (Dierick et al. 2004). After obtaining filtered sinograms, the center of sample's rotation was calculated from the projections at 0° and 180° in step IV. The data was further reconstructed based on filtered backprojection algorithm (Dierick et al. 2004) and represented in 32-bit TIF format (2048 x 2048 pixels). The 32-bit TIF uses floating-point numbers to represent a wide range of grayscales (2^{32} shades) in the sample. The same procedures were repeated for all datasets. A similar slice of both sample N1 (Figs. 4.4a-c) and B1 (Figs. 4.4d-f) were identified for comparison. Small variations in sample tilts, especially in SLS measurement, contribute to slightly shifted views.

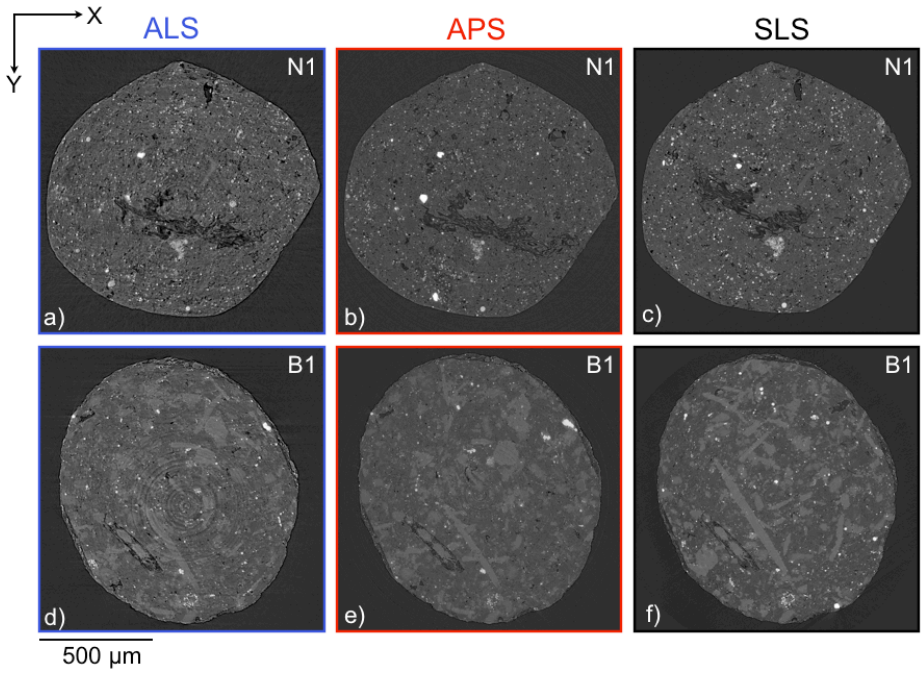

Figure 4.4: Reconstructed images in XY-plane of (a)-(c) sample N1 and (d)-(f) sample B1 obtained from similar areas of the samples. The same level of median filter was used to remove ring artifacts.

The histograms of grayscale value extracted from all measurements were plotted in logarithmic scale and are shown in Fig. 4.5 Overall, the grayscale values of all datasets display comparable ranges in the histogram. The ALS data have a relatively wider range of grayscales (Table 2) and more pronounced negative tail in the histogram. The histogram of APS data contains smallest ranges (Table 2) and falls within the ALS and SLS grayvalues. Note that grayscale of absorption is equal to -ln (%Transmission) = -ln $[(I_s - I_d) / (I_b - I_d)]$. Negative grayscale in the final reconstructed image corresponds to %Transmission greater than 100%, which is when a pixel has a higher value for I_s than for I_b. This can occur due to noise and fluctuations in the incident X-ray beam, or due to phase contrast artifacts. The phase contrast contribution likely explains the more pronounced negative tail in the histogram for the ALS, which has greater phase contrast contributions.

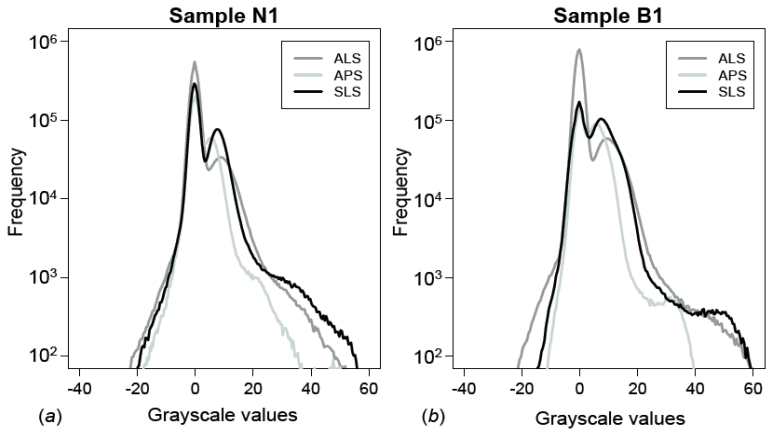

Figure 4.5: Histogram plots of grayscale values, extracted from the same cropped area in Figs.4.7-4.8, in a logarithmic scale of (a) sample N1 and (b) sample B1 obtained from each facility.

4.3.3) Data Segmentation

Several software packages for 3D tomographic data analysis are available (e.g. Lindquist, 2002; Ketcham, 2005; Modular Algorithms for Volume Images, 2005; Brun et al. 2010; Barbant et al. 2011, and etc.) but Quantification Tool in Avizo® Fire software version 6 (Visualization Sciences Group) was used for segmentation in all datasets. Each dataset was input with its corresponding pixel size (0.88 μm for the ALS, 0.72 μm for the APS, and 0.74 μm for the SLS) and processed with a 3D median filter. This filter reduces noise by replacing the grayscale value of each voxel with a median of its neighborhood within 3x3x3 voxel window. Figure 4.6a and 4.6b illustrate the difference between before and after applying the median filter to the reconstructed slice of sample B1. A small volume of interest (VOI) of 250x580x50 μm^3 was selected from sample B1 to emphasize distinctive features (Fig. 4.7). Different components in the filtered data can then be segmented by the thresholding method implemented in Avizo®. The threshold values separate the image into background and foreground (binary) by assigning a label to every voxel and effectively distinguishing between low- and high-absorbing phases.

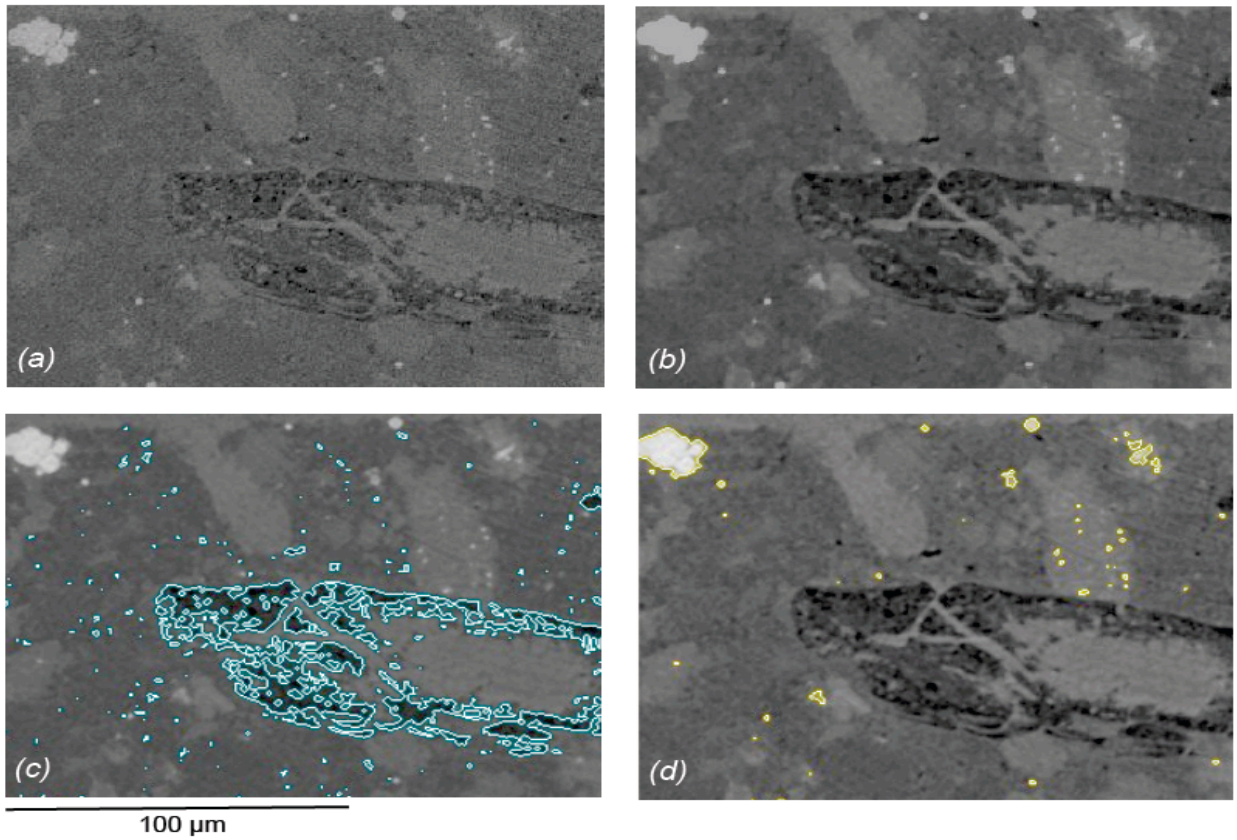

Figure 4.6: Images in XY-plane of sample B1 obtained from the APS display axial reconstructed slice (a) before and (b) after applying a 3D median filter, as well as the thresholding boundary of (c) low density features and (d) pyrite.

The highly absorbing particles (white) are pyrite (Fig. 4.6-4.8) while intermediate shades are combination of clay minerals, quartz, feldspars, and calcite. Low absorbing features (dark) represent low density materials, including pore, fractures and kerogen (Fig. 4.6-4.8). However, it is a non-trivial task to accurately determine appropriate binary threshold values in a multiphase material as in shale because the gray level distribution is continuous, lacking of clearly defined peaks or valleys in the

histogram (Fig. 4.5). In addition, intermediate gray shades are very difficult to segment due to low contrast and blurred boundaries from small grain sizes. Automatic thresholding algorithms such as histogram shape-based, clustering-based, and mean or mode value-based thresholding (Sezgin and Sankur, 2004) are thus not applicable to these datasets. The choice of threshold interval was therefore manually chosen based on visual inspection of low density features and pyrite. For instance, a threshold level of low density features in B1 collected from APS was set between the minimum grayscale of the pixels belonging to the low density features (-10.61) and their maximum gray value (2.46) (Fig. 4.6c). This threshold range sufficiently distinguishes low density features (foreground) from shale matrix (background) and allows the objects to be further analyzed. Figure 4.6d illustrates the thresholding boundary of pyrite with grayscale values between 13.52 and 42.64. After obtaining a binary image, overlapping objects were separated using Watershed Tool and constructed 3D surface via Surface Generation and Surface View Tool in Avizo®. The volume as well as length and width of individual object were also determined from the I-Analyze Tool. Other datasets were quantified under the same approach. For sample N1, the VOI was chosen at 150x180x50 μm^3 μm^3 for 3D segmentation (Fig. 4.8). Based on these considerations, the choices of threshold were selected for pyrite and low density features are summarized in Table 4.2. In addition, the standard deviation (SD) and relative standard deviation (%RSD = (SD/Average)*100%) of phase volumes were calculated in order to compare the precision of different measurements of varying magnitudes (Table 4.2).

Table 4.2: Selected absorption threshold values and volume fractions of pyrite and low density features in samples N1 and B1. The average, standard deviation (SD), and relative standard deviation (%RSD) of phase volumes are also shown. Note that %RSD is (100*SD/Average).

Sample	Source	Grayscale thresholds (Low density features)		Low density features vol.%	Grayscale thresholds (Pyrite)		Pyrite vol.%
		Min.	Max.		Min.	Max.	
N1	ALS	-30.37	3.33	5.6	18.38	72.55	5.0
	APS	-12.58	3.52	6.5	11.67	54.32	5.7
	SLS	-18.25	4.38	6.8	17.84	86.37	6.1
Average				6.3			5.6
SD				0.62			0.56
% RSD				9.91%			9.94%
B1	ALS	-23.67	4.49	4.1	24.00	68.97	1.8
	APS	-10.61	2.46	4.6	13.52	42.64	2.0
	SLS	-15.16	4.00	4.9	21.32	65.86	2.3
Average				4.5			2.0
SD				0.40			0.25
% RSD				8.91%			12.38%

4.4.) RESULTS

Raw projection images of sample N1 collected at each facility are distinctive, particularly the ones from the ALS and the SLS (Figs. 4.2a and 4.2c) contain several bright horizontal streaks. These stripe patterns are caused by X-ray beam inhomogeneities due to reflections on the multilayer composition of a monochromator mirror (Fig. 4.2, Table 4.1). The area without the sample on the ALS image is fuzzy due to background noises. The X-ray beam fluctuation and background can be corrected to some extent with the bright- and dark-field images. Figure 4.2 also shows that the cylinder axis of N1 was positioned differently and slightly inclined at each facility.

Reconstructed slices of sample N1 (Figs. 4.4a-c) and B1 (Figs. 4.4d-f) perpendicular to the cylinder axis (in XY-plane) are displayed on the same brightness and contrast scale. For each facility, a similar section was identified based on unique characteristic features. Low density features (dark areas) indicate pores (small circular spots), fractures (large irregular penny-shaped), and kerogen. Fine details of pore and fracture networks can be clearly illustrated by the data collected from the APS and the SLS whereas the data from the ALS might represent only coarser features (Figs. 4.4, 4.7-4.8). Other intermediate-absorbing materials in the matrix such as clays, quartz, and feldspars are much more difficult to distinguish from each other due to low contrast. Blurriness and ring artifacts were observed in all datasets, but most prominent in the data from the ALS (Figs. 4.4a and d) despite performing the same level of ring removal.

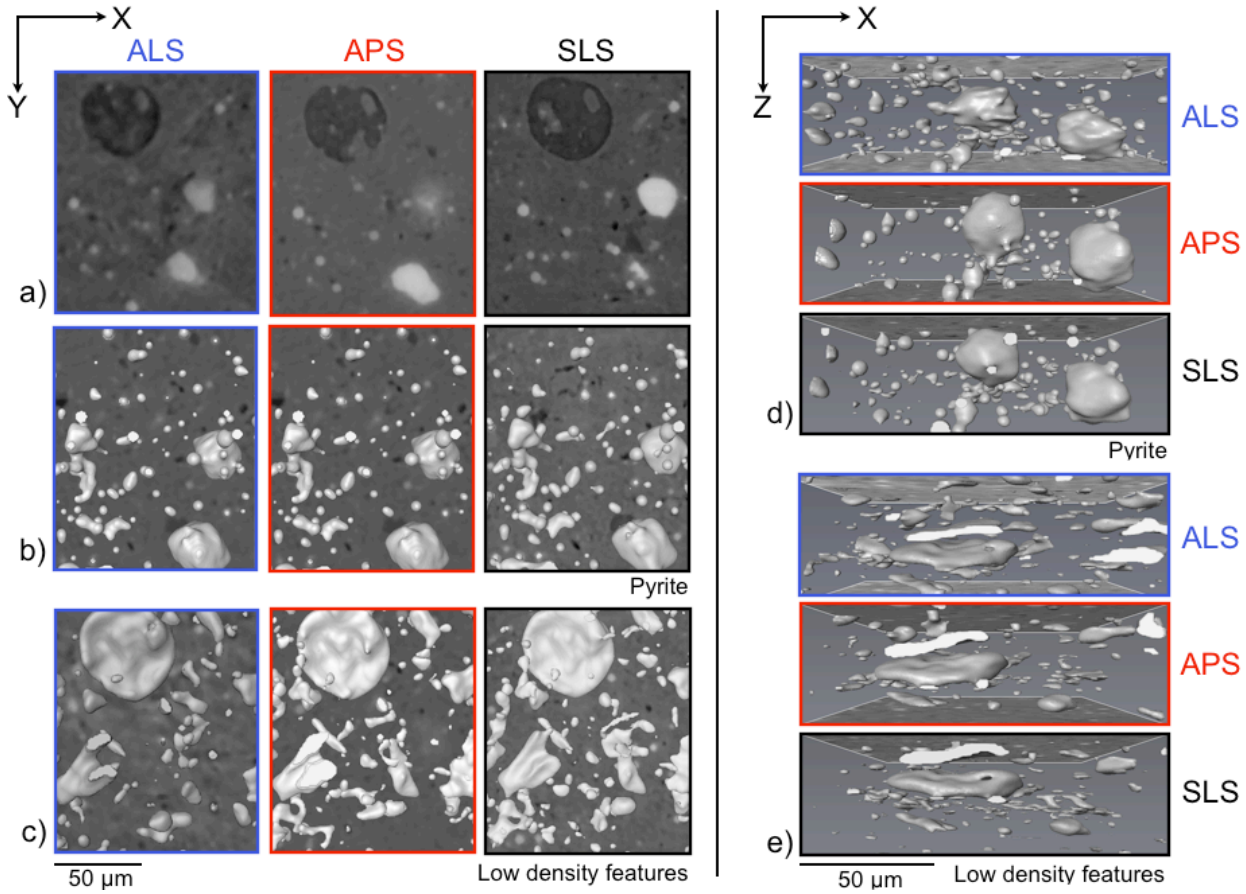

Figure 4.7: Images in the XY-plane show (a) axial slices through the cropped reconstructed volume of sample N1 after applying a 3D median filter, (b) the segmentation of pyrite, and (c) low density features in 3D. An alternate view in XZ-plane of the geometry and 3D distribution of (d) pyrite and (e) low density features are also displayed.

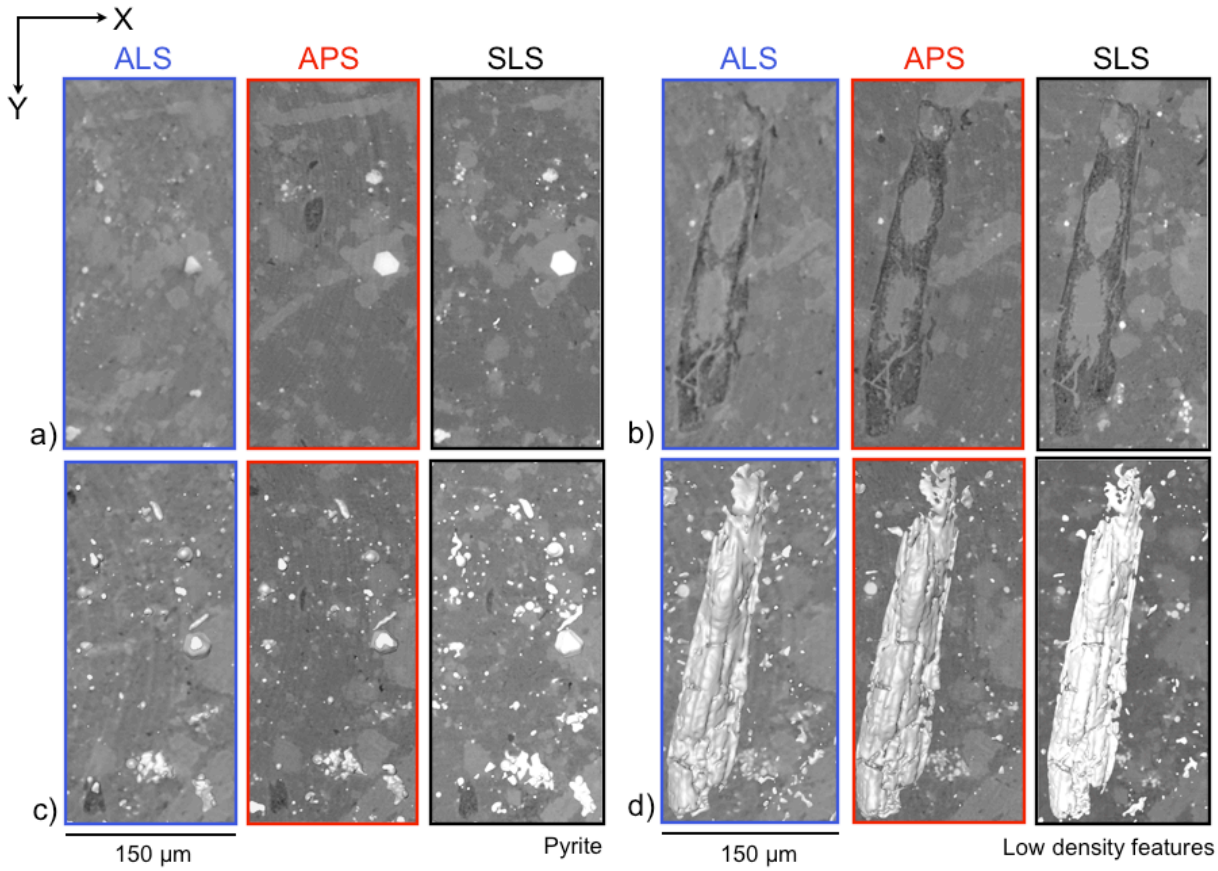

Figure 4.8: Images in the XY-plane show axial slices through the cropped reconstructed volume of sample B1 after applying a 3D median filter in (a)-(b), (c) the segmentation of pyrite, and (d) low density features in 3D.

Two main elements were segmented to illustrate the 3D internal microstructure (Figs. 4.7-4.8) and to calculate volume fractions (Table 4.2) and aspect ratio. The resolution of the system is in the order of 2 pixels (e.g. for the SLS 0.74 µm x 2 = 1.44 µm), thus any feature smaller than 3 μm^3 (i.e. $(1.44\ \mu m)^3 = 2.99\ \mu m^3$) was excluded from calculations due to the limit of the resolution. In both samples, pyrite is generally spherical, organized in small clusters, and dispersed throughout the sample (Figs. 4.7-4.8). In sample N1, the average volume of pyrite was estimated at 5.6%, with a slight variation between data obtained from the ALS (5.0%), APS (5.7%), and SLS (6.1%).

Pyrite is much less abundant in sample B1, with the average volume of 2.0%. A minor variation was also observed between data collected from different facilities (ALS 1.8%, APS 2.0%, and SLS 2.3%). In contrast to pyrite, the shape of low density features, including pores, fractures, and kerogen, is mostly flat and penny-shape like (Figs. 4.7e and 4.8d). Small low density features ($<10\ \mu m^3$) are scattered throughout the sample while the large ones are aligned roughly parallel to the bedding plane (Fig. 4.7e). Some kerogen has irregular shape but is oriented horizontally (Fig. 4.8d). The average volume fraction of low density features in sample N1 (6.3%) is higher than in sample B1 (4.5%). In addition, the volume fractions of low density features and pyrite in both samples extracted from the APS and SLS data are more closely consistent (Table 4.2). Segmentation from the ALS data again yields lowest volume estimation in both phases and samples. The %RSD of phase volumes are quite comparable, particularly those of low density features (9.91%) and pyrite (9.94%) in sample N1, as well as that of low density features in sample B1 (8.91%). The similarity of

%RSD suggests that these measurements have more or less the same precision. Segmentation of pyrite in sample B1 has highest %RSD (12.38%) probably due to its lowest magnitude of average volume.

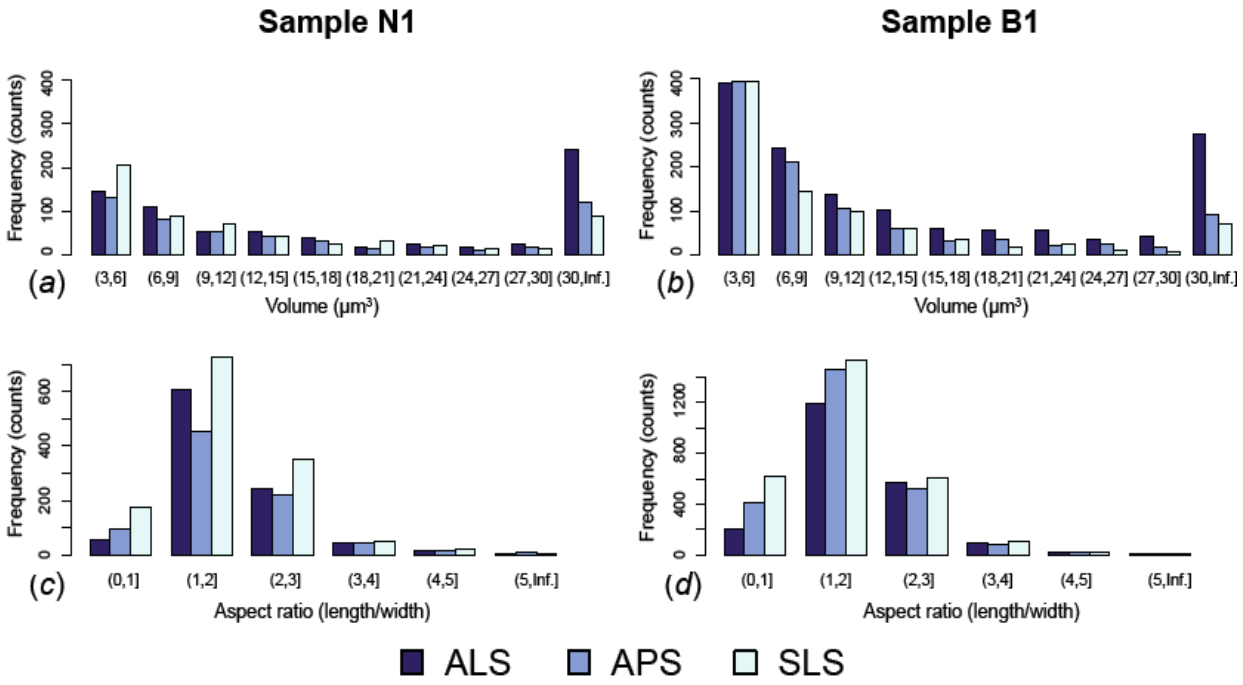

Figure 4.9: Histogram plots depict (a)-(b) the volume distribution of low density features and (c)-(d) their aspect ratios (length/width) in samples N1 and B1, respectively.

The 3D segmentation images (Figs. 4.7e and 4.8d) illustrate the shape and alignment of low density features in both samples. The aspect ratio (length/width) of low density features was also quantified, it ranges mostly between 1 and 3 (Fig. 4.9c-d). The volume distribution shows that a majority of low density features is between 3 and 6 μm^3 (Fig. 4.9a-b). The abundance of these small and scattered features are clearly visible in Fig. 4.7(e) and 4.7(d). Some large low density features (kerogen) (>100 μm^3) were also identified and aligned more or less parallel to the bedding plane (Fig. 4.8b-d).

4.5) Discussion

4.5.1) Shape Preferred Orientation (SPO)

Third-generation synchrotrons provide high brilliance and intensity to produce high-quality SXMT images for fine-grained shales. The data collected from each facility depict various 3D internal features of different samples and the same microstructures can be identified. Pyrite and low density features, including pores, fractures, and kerogen are the main elements that can be clearly observed, segmented, and quantified for relative abundances, volume distributions, and shape identification (Figs. 4.6-4.8). As a number of studies suggests, LPO and SPO of constituent phases in shales have a strong influence on elastic anisotropy and directionality of acoustic velocities (Sayers, 1994). For the application to shale seismic anisotropy, shape preferred orientation and aspect ratios of low density features is of most interest as the information can be used in anisotropic effective medium modeling for velocities (Hornby et al. 1994).

The volume of low density features in sample N1 obtained from SXMT images (6.3(6)%) is higher than the porosity reported in a previous study (2.5%) (Hornby, 1998) due to several reasons. First, the volume of low density feature includes not only porosity but also fractures and kerogen. The previous porosity was derived from a mercury injection capillary pressure experiment (MICP), which measures pores at nanometer scale as the sample is compressed under high pressure. SXMT cannot image pores in nanoscale and the measurements in this study was performed at ambient pressure, at which the pore spaces were not closed up as tightly as in the MICP experiment. The total pore volume is thus inconsistent due to different experimental conditions. In addition, the results of the current study could be biased by the selected regions of interest, which was chosen because of the presence of large unique features (e.g. kerogen and fractures) that can be obviously identified in the three datasets. Thus the selected area is rather a small and heterogeneous region, which might not be a good representative of the overall porosity. An overestimation of porosity could also be due to too high maximum threshold interval (Table 4.1). However, the volume distribution (Table 4.2) and aspect ratio calculations (Fig. 4.9) on the same selected area obtained from different facilities show fairly consistent results.

4.5.2) Spatial Resolution

A small discrepancy of volume fraction determined from each facility comes from several reasons (Table 4.2). First, the selection of threshold values affects how volume proportions are determined. Although the data segmentation was performed on the same basis, it is difficult to precisely choose threshold values that identically represent the desired features in different datasets. Secondly, the blurriness is present in all datasets but is most prominent in the reconstructed data of the ALS (Figs. 4.4, 4.7-4.8). The image blurring (d) is due to the finite size of the photon source (D) as described by

$$d = l / (L/D)$$

where l is the sample-to-detector distance and L is the sample-to-source distance (Schillinger et al. 2000). From this equation, it is obvious that a large photon source size and long sample-to-detector distance in the SXMT system can lead to a high degree of blurriness. This is evident as the photon source size and sample-to-detector distance of the ALS (15 mm) are significantly larger than those of the APS (6 mm) and SLS (5 mm) (Table 4.1), causing more blurring and phase contrast in the reconstructed images. Phase contrast affects the spatial resolution as it is generated by a phase shift or interference phenomena of Fresnel fringes. The resolution limit of edge-enhanced systems (RL) is approximated by

$$RL = \sqrt{\lambda * l}$$

where λ is the wavelength and l is the sample-to-detector distance. From this equation, it can be inferred that a smaller sample-to-detector distance leads to a better spatial resolution. Since this distance varies greatly amongst facilities (5-15 mm), the effect of phase contrast on the images would also be significantly different. Also phase contrast is more pronounced when X-ray goes through a large amount of phase boundaries, such as those of low density features. These factors thus affect the spatial resolution and the quantification of interested features as a result. Artifacts is another factor that affects the data quality and volume calculation. Concentric ring artifacts were observed in the reconstructed data of the ALS and APS (Figs. 4.4a-b, 4.4d-e, 4.8a, and 4.8b) due to photon interactions, X-ray intensity fluctuations, sensitivity and defective pixels in the detector and/or scintillator (Vidal et al. 2005). Other artifacts can also get transferred from the mathematical reconstruction algorithm, but this factor is less likely to create more or less artifacts between datasets here. Beam hardening artifacts are typically observed in data collected from conventional X-ray sources (Baruchel et al. 2000) but not from SXMT images. The differential absorption of the

polychromatic X-ray beam by the sample causes sample borders in the reconstructed slices to be brighter and yields a misleading calculation of the linear absorption coefficients.

Poor spatial resolution in SXMT images can also be improved. The spatial resolution (*R*) can be described by

$$R = \sqrt{\left(\frac{p}{NA}\right)^2 + \left(q * x * NA\right)^2}$$

where NA is the numerical aperture, x is the scintillator thickness, and p and q are constants (Stampanoni et al. 2002). From this equation, the numerical aperture (NA) and the scintillator thickness are the main factors that determine the spatial resolution. For each scintillator thickness, an optimal NA is necessary for achieving high spatial resolution. Besides, scintillator material can affect the spatial resolution. Single crystal lutetium aluminum garnet doped with cerium (LuAG:Ce) is used at the APS and SLS whereas single crystal cesium iodide doped with thallium (CsI:Tl) (Table 4.1) is employed at the ALS. The LuAG:Ce scintillator is more efficient and able to achieve higher resolution that the CsI:Tl one. The setup of BL 8.3.2 at the ALS is optimized for lower magnification e.g. 5x and 2x objective lens. With increasing magnification (e.g. 10x), the depth of focus of visible light optics is decreasing, thus a thinner scintillator and appropriate NA are necessary for improving spatial resolution at the ALS.

Limitations on spatial resolution and different sources of artifacts as well as bluriness introduce challenges into visualization and quantitative extraction of constituent phases in shales with a wide range of grain sizes and phases of different absorption characteristics. SXMT methods may be complemented with nanoscale approaches such as focused ion beam scanning electron microscopy (Keller et al. 2011; Bera et al. 2011), transmission electron microscopy, and X-ray nanotomography (Nelson et al. 2011; Grew et al. 2010). Overall, this round robin experiment of synchrotron SXMT documented that all three beamlines produce similar results with microstructural resolution of approximately 2 μm. The 3D images of low density features and pyrite crystals, as well as derived morphological information such as volume fractions, size distributions and aspect ratios are consistent among facilities, suggesting that this methodology is robust and ready to be applied to similar samples in the future.

4.6) CONCLUSIONS

Shales are challenging samples because many microstructural features are in the micron scale, at the limit of the resolution. SXMT non-destructively provides visualization and characterization of the SPO of low density features, including pores, fractures, and organic matter or kerogen. The sharpness of phase boundaries in the reconstructed data collected from the APS and SLS was comparable and slightly more refined than in the data obtained from the ALS. The discrepancy of data quality and volume fractions was mainly due to different types of optical instruments and varying technical setups at each facility. This project identifies critical parameters in instrument capabilities and data processing, as well as suggests corresponding improvements. State-of-the-art SXMT is proven to be a valuable tool to address various open questions in the geological field.

CHAPTER 5

THE LINK BETWEEN PREFERRED ORIENTATION & ELASTIC ANISOTROPY OF QUSAIBA SHALE

5.1) INTRODUCTION

Elastic properties of shales can be calculated by averaging single crystal elastic coefficients of constituent minerals over the experimentally determined orientation distributions (OD). For simplicity, the bounds for the elastic constants and velocities in rock physics modeling are often assumed to be isostrain or Voigt upper bound (Voigt, 1887) and isostress or Reuss lower bound (Reuss, 1929) averages. With respect to the Reuss and Voigt averaging, the Hashin-Shtrikman bounds (Hashin and Shtrikman, 1963) give relatively narrower possible ranges of elastic modulus, but exclude anisotropic microstructures. These averages constitute bounds that maybe similar for polyscrytalline aggregates of isotropic matrix. However, depending on microstructural characteristics, the actual elastic properties can be taken as the average of the Voigt and Reuss bounds, known as the arithmetic Hill average (Hill, 1952) or a Geometric mean (Matthies and Humbert, 1993). From different averaging approaches, elastic properties of shales can be obtained and then compared with ultrasonic velocity measurements.

This study is oriented toward two main goals. The first aim is to characterize both LPO and SPO of lower Silurian diagenetic shales of the Qusaiba Formation from Saudi Arabia by applying synchrotron X-ray diffraction and microtomography techniques. The extracted microstructural information is then used to calculate the elastic properties of the polyphase aggregates, assuming a nonporous material. A comparison between the calculated and measured elastic velocities is then made to explore whether these approaches can accurately predict the elastic properties.

5.2) SAMPLES

Three shales from a well drilled in south-west Saudi Arabia were used in this study (referred to as Qu1, Qu2 and Qu3). The samples were retrieved at a depth of 3566 m from the Lower Silurian Qusaiba member of the Qalibah Formation. This formation is the main source rock for hydrocarbons in the Palaeozoic section of the Rub'al-Khali basin (Al-Harbi 1998; Schenk, Pollastro and Ahlbrandt 2002) and is mainly composed of claystones, interbedded with siltstones and mudstones. Information obtained from the South Rub Al-Khali Company (SRAK) documents shows that the sample is from a lean portion of the Qusaiba, with total organic carbon (TOC) of 1.5%. Qusaiba samples are also very fine-grained, quite heterogeneous, firmly cemented, and have a low porosity (~3 vol.%). They are visibly anisotropic, with horizontally deposited mica platelets and layers of kerogen rich material in a matrix of cemented mudrock.

5.3) EXPERIMENTAL TECHNIQUES

5.3.1) Scanning Electron Microscopy (SEM)

A polished slice of the shale sample Qu2 was coated with carbon and analyzed for mineralogical composition and microstructure with a Zeiss Evo MA10 low vacuum scanning electron microscopy (SEM) equipped with an EDAX Energy-Dispersive Spectroscopy (EDS) system at the University of California, Berkeley. The SEM was operated with an accelerating voltage of 30 kV and a probe current of 20 nA to collect images. The brightness variation of the back-scattered electron (BE) SEM image, ranging from low (black) to high (white) is due to the contrast in atomic number, with high atomic numbers appearing bright. EDAX Genesis Imaging/ Mapping software was used to collect compositional maps for Fe, S, Mg, Si, O, Al, and K.

5.3.2) High-Energy Synchrotron X-ray Diffraction

The sample preparation and experimental setup are similar to the LPO measurements done on the Posidonia Shale (See Chapter 3, section 3.2). Thres Qusaiba shales were measured at the BESSRC 11-ID-C beamline of the APS. A monochromatic X-ray beam with a wavelength of 0.10779 Å (115 keV) and a diameter of 0.5 mm was used to ensure high penetration through the sample. The sample was also translated over 3 mm along the horizontal axis and tilted from -60° to 60° in 20° incremental steps to ensure sufficient grain statistics. Diffraction images were recorded with a Mar345 detector, positioned at about 2 m from the sample. Typical images, recorded a 2θ angle range from 0–4.6° for 60 s. Intensity variations along some Debye rings immediately indicate the LPO of corresponding lattice planes *hkl*. (Fig. 5.1).

The diffraction images were integrated over 10◦ intervals to produce 36 spectra and analyzed with MAUD software (Lutterotti et al. 1997). Crystallographic parameters for different phases used here are the same as for minerals in Posidonia Shale (see Chapter 3, section 3.2). Phase parameters such as volume fraction and lattice parameters were refined but atomic coordinates were kept constant (Table 5.1). The peak shapes and widths are governed by microstructural parameters and thus were modeled by refining an isotropic crystallite size and microstrain. The LPO was computed by the EWIMV algorithm (Matthies and Vinel 1982), using 10◦ resolution for the orientation distribution (OD) determination, without imposing sample symmetry. The OD was exported and smoothed with a 7.5◦ filter to minimize artifacts from orientation distribution cell structure in the BEARTEX software (Wenk et al. 1998), then plot (001) and (100) pole figures. The (001) pole figures have a strong maximum in the center, indicating that (001) lattice planes of clays are more or less parallel to the bedding plane. The (100) pole figures are shown to establish if there are constraints on the orientation of *a*-axes [100] or if they have rotational freedom in the (001) plane.

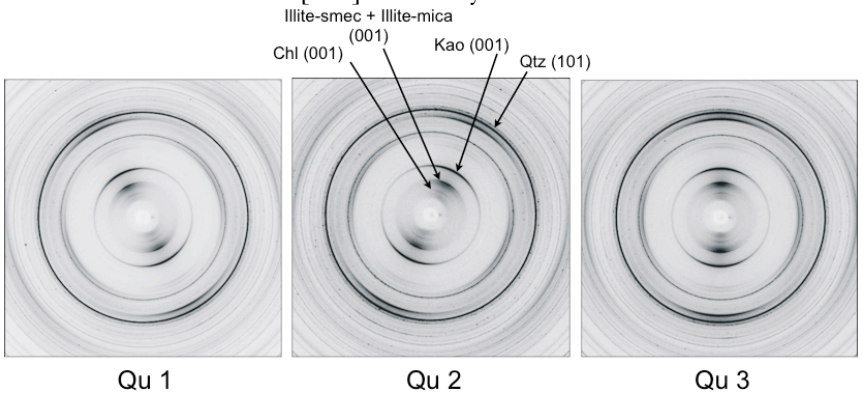

Figure 5.1: Diffraction patterns of sample Qu1-Qu3 illustrate the variation of X-rsy intensity along the azimuth, indicating the LPO of clay minerals.

Table 5.1: Lattice parameters of major phases used in the Rietveld refinement. Standard deviations are indicated in parentheses. Parameters of quartz, k-feldspars, pyrite, and chlorite are kept constant throughout the refinement. Monoclinic phases are in the second setting.

Phase	Sample	A (Å)	b (Å)	c (Å)	α (°)	β (°)	γ (°)
Kaolinite	Qu1	5.181	8.956	7.440	91.863	104.999	89.911
	Qu2	5.184	8.980	7.444	92.134	105.058	89.309
	Qu3	5.184	8.980	7.444	92.134	105.058	89.309
Illite-Smectite	Qu1	5.371(1)	8.936(2)	11.170(2)	90.000	100.529	90.000
	Qu2	5.112	9.496	11.164	90.000	95.661	90.000
	Qu3	5.112	9.496	11.164	90.000	100.529	90.000
Illite-Mica	Qu1	5.254	9.046(1)	20.391(1)	90.000	95.366	90.000
	Qu2	5.247	9.062	20.343	90.000	95.096	90.000
	Qu3	5.247	9.062	20.343	90.000	95.37	90.000
Chlorite	Qu1 Qu2 Qu3	5.327	9.232	14.399	~90	97.160	~90
Quartz	Qu1 Qu2 Qu3	4.937	4.937	5.433	90.000	90.000	120.000
K-feldspars	Qu1 Qu2 Qu3	8.604	13.029	7.263	90.000	116.005	90.000
Pyrite	Qu1 Qu2 Qu3	5.442	5.442	5.442	90.000	90.000	90.000

5.3.3) Synchrotron X-ray Microtomography

A small cylinder of Qu2 was prepared in a size of 1 mm in diameter and 5 mm in height. The cylinder was investigated at the TOMCAT beamline of SLS. The sample is rotated in 0.12◦ increments, resulting in a total of 1500 projections, while exposing to a monochromatic X-ray with a wavelength of 0.775 A° (16 keV). A 20x lens was used during the scan thus each voxel has a size of 0.38 μm x 0.38 μm x 0.38 μm.

Raw projections were reconstructed with local software at the SLS (Stampanoni et al. 2006). A cubic volume of 150 μm x 150 μm x 150 μm was selected from the array to represent the volumetric data set and characterized by the Avizo software (Visualization Sciences Group). Segmentation was done based on the grayscale value threshold (See Chapter 4, section 3.3). Low absorption features (dark) with values ranging from 10043–24800 are indicative of porosity, fractures and/or kerogen. The highly absorbing particles (white) with values ranging from 44000–65535 are pyrite, intermediate shades represent quartz, feldspars and clay minerals.

5.3.4) Ultrasonic Velocity Measurements

Elastic P- and S-wave velocities were measured by Shell at the Geomechanics Laboratory in Rijswijk, the Netherlands. A cylindrical plug (36 mm in diameter and 52.1 mm in length) with an axis normal to the bedding plane was drilled from the core. This core was quite homogeneous and contains a number of visible horizontal fractures. These fractures may have originated as stress relief features and from poor core preservation, or alternatively have been opened as a result of core extraction and sample preparation. As the rock was cemented and had a long history of diagenesis in the subsurface, the probability of substantial damage to the LPO and clay structure of the sample due to storage conditions was considered to be minor. This core is not identical to the samples used for the synchrotron X-ray measurements but retrieved in close proximity of each other, and can hence be expected to have similar properties on the cm scale.

The velocity measurements were performed in a biaxial compaction apparatus, where the plug is mounted between titanium end-caps and enclosed in a Viton sleeve. Within that sleeve, the sample is wrapped in metal gauze in order to allow radial drainage and enhanced pressure equilibration via a permeable shell around the circumference of the plug. This method is widely employed in shale testing and described in detail in the literature (e.g., Hornby 1998; Jacobsen et al. 2000; Dewhurst et al. 2006; Fjaer et al. 2008). The apparatus is rated at 100 MPa with an independent control of axial stress, confining or radial stress and pore fluid pressure, in order to mimic the *in-situ* vertical stress, horizontal stress and pore pressure. Pairs of piezoelectric transmitters and receivers for ultrasonic P- and S-waves are embedded in the end caps. In addition, P-wave transducers are mounted to the outside of the Viton sleeve. The pulse transmission with frequency ~1 MHz is employed to measure elastic P-wave velocity in the radial direction (parallel to bedding) and P- and S-wave velocities in the axial direction (normal to the bedding plane and along the symmetry axis). The signals were recorded at the ultrasonic receivers after pulse transmission travelling through the sample and end-cap (axial), as well as through the sample and sleeve assembly (radial). The time scale has its origin at the trigger for the pulse transmission. The original, transmitted pulse is clearly maintained in the received signals. This allows straightforward, accurate and reliable picks of arrival times, on which the derived velocity values are based.

The plug was also saturated with tap water and after two weeks loaded stepwise with 4 MPa steps to a maximum net stress condition, followed by a low rate simultaneous increase of pore pressure and total stress while maintaining the system at a constant net stress (net stress = total stress – pore fluid pressure). Each step was followed by a hold period of 48 hours to equilibrate pore fluid pressure and strain throughout the sample. The total stresses, corresponding to *in-situ* conditions, are 80 MPa in the axial direction and 66 MPa in the radial direction, with a 71MPa mean value. The maximum net stresses selected for the experiment were 27 MPa in the axial direction and 13 MPa in the horizontal direction, with an 18 MPa mean value. The corresponding pore pressure was 53 MPa, which is higher than the actual *in-situ* pore pressure of 37 MPa. The measurement was thus taken at an overpressure situation. Measurements at lower net stresses and overpressure conditions were used to extrapolate velocities to the values at *in-situ* stress condition.

5.4) RESULTS

A backscattered (BE) SEM image shows complex microstructures of authigenic illite-smectite, kaolinite, detrital illite-mica platelets, some coarse-grained quartz, and pyrite with a well-developed horizontal bedding plane (Fig. 5.2a). Only maps for Fe, S, Mg and Si are displayed in Fig. 5.2b-e, suggesting an abundance of detrital angular quartz (SiO_2), Fe- and Mg-containing detrital mica and pyrite (FeS_2).

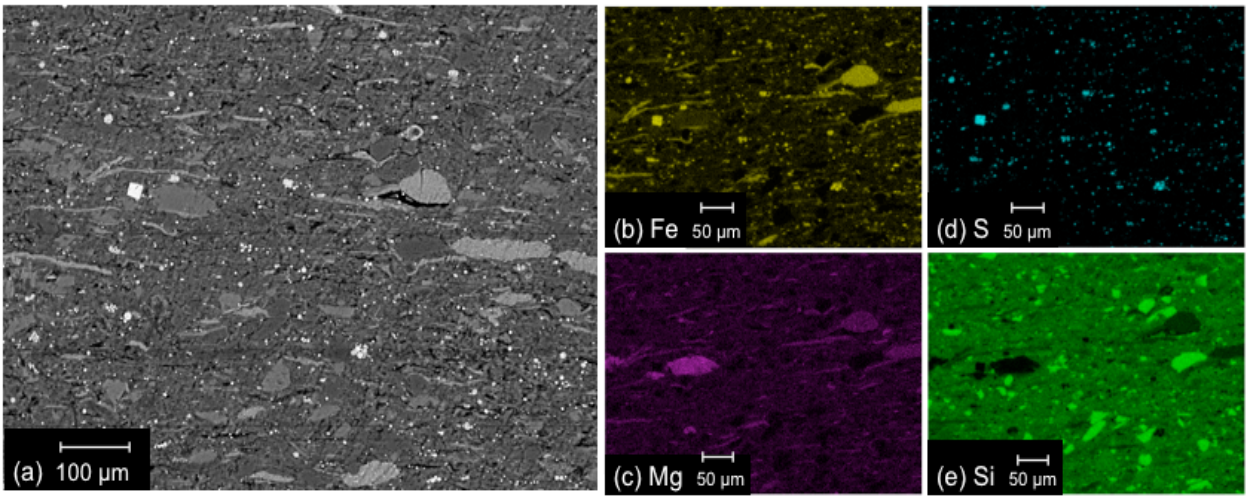

Figure 5.2: (a) A back-scattered SEM image of sample Qu2 showing microstructures of different phases and (b)-(e) EDS chemical maps of Fe, S, Mg, and Si.

5.4.1) Lattice Preferred Orientation (LPO)

A summary of seven phase proportions in weight fractions extracted from Rietveld analysis is given in Table 5.2. All samples are rich in clays (~60-70%), with the illite-group as the dominant phase. There are large amounts of detrital quartz and illite-mica. Among authigenic clays, kaolinite dominates over illite-smectite.

Table 5.2: Quantitative phase proportions in weight% fractions extracted from Rietveld analysis.

Sample	Kaolinite	Illite-Smectite	Illite-Mica	Chlorite	Quartz	K-feldspars	Pyrite
Qu1	28.46	19.06	13.80	4.55	22.02	8.58	3.52
Qu2	25.31	22.19	20.19	3.56	20.18	5.47	3.09
Qu3	27.48	21.16	20.60	4.56	18.93	4.35	2.93

The diffraction peaks of illite-smectite are diffuse (Fig. 5.3a), indicating small grain size and considerable stacking disorder. Figure 5.3b (bottom: Exp.) displays a stack of these spectra of Qu2 for the 0° tilt image. It clearly shows peak intensity variations with the azimuth. A Q range of 0.37–3.70 A^{-1} (d-spacing 1.80–16.98 A°) was used for the refinement. Illite-smectite was successfully separated from illite-mica with diffraction peaks at similar positions (see insets in Fig. 5.3). Glycolation tests could not identify montmorillonite and the 14 °A peak is attributed to chlorite.

The LPO of clays is represented as pole figures (Fig. 5.4), with maximum and minimum pole densities given in Table 5.3. In general, the degree of LPO of clay minerals is quite strong, whereas the orientations of quartz, K-feldspars and pyrite are close to random (pole figures are not shown). All pole figures are more or less axially symmetric with the (001) maximum perpendicular to the bedding plane and rotational freedom of (100). Kaolinite shows a strong degree of LPO (4.4–6.5 m.r.d.). Detrital illite-mica has a stronger LPO (3.2–6.8 m.r.d.) than authigenic illite-smectite (2.4–4.0m.r.d.). There is some variation between the samples. Illite-mica in Qu1 has the highest LPO with a (001) maximum perpendicular to the bedding plane of 6.8 m.r.d. A similar maximum is observed for kaolinite in Qu3 (6.5 m.r.d.). Orientation distributions of chlorite are quite high in all samples but most relevant in Qu3 with 5.8 m.r.d. The weakest degree of LPO is observed in Qu2.

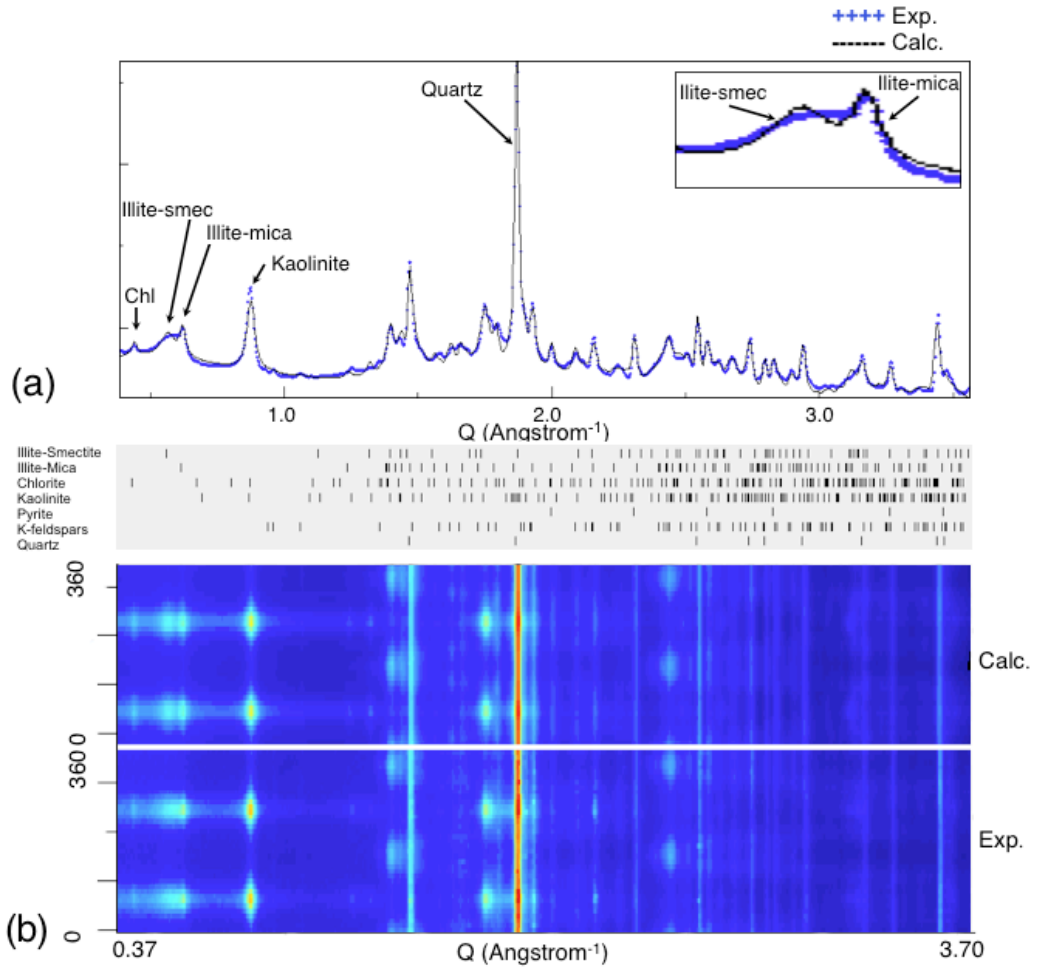

Figure 5.3: (a) Average diffraction spectra showing experimental data (dotted line) and calculated (solid line) models and (b) map 2D plots of calculated (top) and experimental (bottom) diffraction spectra of Qu2. The gray shades illustrate the intensity variation in the diffraction images.

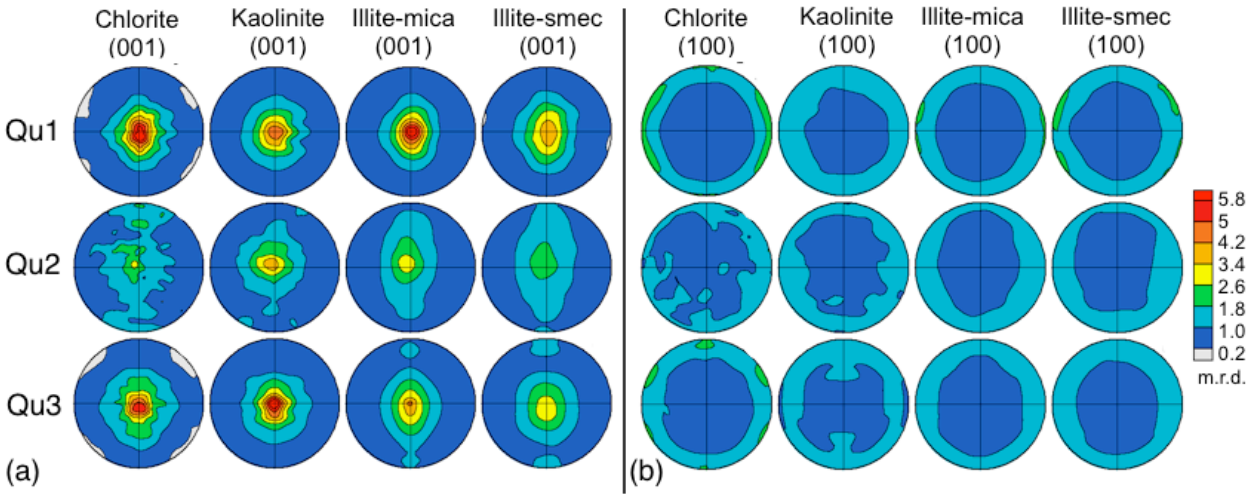

Figure 5.4: (a) (001) and (b) (100) pole figures for chlorite, kaolinite, illite-mica, and illite-smectite from the OD of all samples. Equal area projection on bedding plane. Contours in m.r.d.

Table 5.3: Pole densities for (001) of different clay pole figures (m.r.d.).

Sample	Kaolinite		Illite-Smectite		Illite-Mica		Chlorite	
	Min	Max	Min	Max	Min	Max	Min	Max
Qu1	0.29	4.81	0.19	3.97	0.30	6.75	0.17	5.61
Qu2	0.33	4.41	0.41	2.42	0.44	3.23	0.17	3.56
Qu3	0.19	6.49	0.29	3.31	0.36	4.56	0.12	5.77

5.4.2) Shape Preferred Orientation (SPO)

Figure 5.5 illustrates the 2D and 3D reconstruction images of Qu2. Pyrite exists in the form of individual octahedral crystals (5–20 μm) and as fine-grained framboidal clusters (<1 μm) (Fig. 5.5c). The distribution seems random and not linked to the bedding plane. In contrast, low density features, including pores, fractures, and kerogen are anisotropic. They are organized mainly parallel to bedding, with little connectivity of the flat pores in the direction perpendicular to the bedding plane (Fig. 5.5b). A few large horizontal fractures are also observed. Segmentation done by the Avizo software shows that the volume fractions of low density features and pyrite are estimated at 1.1 vol% and 0.7 vol%, respectively. The porosity derived from tomography images is lower than the value derived from a mercury injection capillary pressure experiment (~3.0 vol%) as nanometer size pores are beyond the resolution of microtomography.

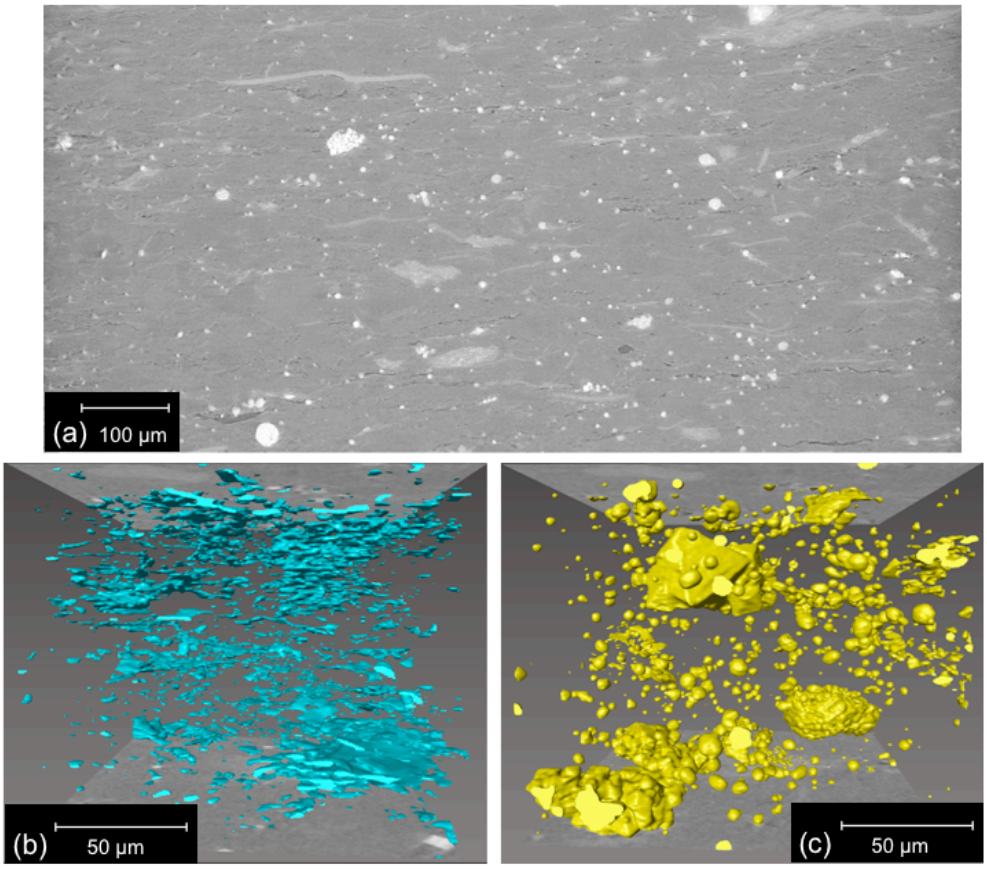

Figure 5.5: (a) A tomographic 2D slice of sample Qu2 and 3D images showing the geometry and distribution of (b) porosity and microfractures and (c) pyrite.

5.4.3) Elastic Anisotropy Calculations

The orientation distributions and single crystal elastic properties are required for the calculation of the elastic properties of the anisotropic polyphase aggregate. Elastic properties of clay minerals are not very well-known (e.g., Mondol et al. 2008). Crystals are generally too small for experimental determinations. Depending on the approximation method, quite different values have been obtained for numerical estimates from experiments in which clay properties are calculated from an extrapolation of trends assuming clay mineral distributions that best fit the data (Hornby et al. 1994; Wang et al. 2001). Indentation tests find relatively low values for elastic constants (Prasad et al. 2002). Katahara (1996) attributed differences between estimates derived from well-crystallized clays and other values to the presence of microcracks aligned with crystals and to the presence of bound water that would naturally align with the crystal surfaces.

The first principles calculations for single crystal elastic properties of clays based on the local density approximation (LDA) (Militzer et al. 2011) are used in this study (Table 5.4). These parameters are very reliable for illite-mica but that there is some uncertainty for illite-smectite, particularly the C_{33} that relies on the structural stacking model. This illite-smectite model takes structural water into account but excludes additional water layers in the expanded smectite structure. Stacking and polytypism does not affect elastic properties appreciably thus this also model is used for ideal kaolinite. The values from Militzer et al. 2011 are considerably different from the simulations by Sato et al. (2005). Some off-diagonal coefficients for kaolinite are consistently large, which is expressed in an unexpected behavior for shear waves and particularly shear-wave splitting (Fig. 5.6). Elastic properties of quartz are based on experimental data of Heyliger et al. (2002).

Table 5.4: Single crystal stiffness tensor coefficients (C_{ij}) of kaolinite, illite-smectite, illite-mica, chlorite, and quartz that were used in elastic properties calculations (in GPa).

Phase	C_{11}	C_{12}	C_{13}	C_{22}	C_{23}	C_{33}	C_{44}	C_{55}	C_{66}
Kaolinite[(1)]	169.1	66.1	15.4	179.7	10.2	81.1	17.0	26.6	57.6
Illite-smec[(1)]	27.2	13.2	5.2	153.9	25.1	188.5	55.4	10.4	2.8
Illite-mica [(1)]	60.3	27.2	23.5	180.9	53.4	170.0	70.5	18.4	23.8
Chlorite [(1)]	180.9	53.4	27.2	170.0	23.5	60.3	18.4	23.8	70.5
Quartz [(2)]	87.3	6.6	12.0	87.3	12.0	105.8	57.2	57.2	40.4

Note [(1)] Militzer *et al.* 2010; [(2)] Heylinger 2002

Since orientation distributions are close to axial symmetry, cylindrical symmetry (transverse isotropy) is imposed for the polyphase aggregate property calculations, reducing the elastic tensor from 21 to 5 independent components ($C_{11} = C_{22}$, $C_{12} = C_{11} - 2C_{66}$, $C_{13} = C_{23}$, C_{33}, $C_{44} = C_{55}$, all others are zero) (Nye 1956). First, elastic properties of contributing mineral phases were calculated by averaging single crystal elastic properties over the mineral orientation distributions for the individual phases in the software BEARTEX (Wenk et al. 1998) and then averaging over all phases according to volume fractions was performed. Values of C_{ij} for Voigt (1887), Reuss (1929), Hill (1963) averages and a geometric mean average (Matthies and Humbert 1993) are shown in Table 5.5. There is a considerable difference between the constant strain (Voigt) and constant stress (Reuss) average for these strongly anisotropic materials, particularly for coefficients along the diagonal (C_{11}, C_{33}, C_{44} and C_{66}). For example, C_{33} for the Voigt average is 44% larger than for the Reuss average. There is not much difference between arithmetic (Hill) and geometric means.

Table 5.5: Calculated polycrystal stiffness tensor coefficients (C_{ij}) in GPa assuming axial symmetry by Voigt, Reuss, Hill averages, and Geometric mean.

C_{ij}	Qu1				Qu2				Qu3			
	Voigt	Reuss	Hill	Geo.	Voigt	Reuss	Hill	Geo.	Voigt	Reuss	Hill	Geo.
C_{11}	124.88	87.72	103.70	107.72	119.35	83.97	99.35	102.07	126.36	88.63	104.99	108.70
C_{13}	22.80	20.26	21.49	22.75	23.32	20.70	22.64	22.74	25.25	21.85	23.46	24.92
C_{33}	94.09	72.25	81.91	81.27	101.97	75.06	85.69	86.96	97.82	73.56	84.25	83.99
C_{44}	40.51	27.80	33.23	32.88	41.97	28.69	33.35	34.17	40.50	27.45	33.06	32.70
C_{66}	48.10	33.15	39.60	40.64	46.20	31.64	37.20	38.44	47.44	32.54	39.00	39.81

From these aggregate elastic properties, P- and S-wave velocities as well as P-wave anisotropy were calculated (Anisotropy % = 200*[(Vpmax-Vpmin)/(Vpmax+Vpmin)]). The calculated results of an average over the stiffness tensors of the three samples as a representative value for the polyphase aggregate properties of the Qusaiba Shale and derived corresponding velocities (Table 5.6, Qu_{AVE}). Figure 5.6 shows calculated P-wave velocities and shear-wave splitting for individual clay components, averaged over the three samples, as a function of the angle to the bedding plane normal. Low P-wave velocities and no S-wave splitting are observed perpendicular to the bedding plane (0°). In all samples, illite-mica and illite-smectite are strongly anisotropic (11.8–22.4% and 15.4–34.0%, respectively), combining strong preferred orientation and strong single crystal anisotropy. The anisotropy of kaolinite is smaller, ranging from 12.0–17.1%. The anisotropy of chlorite is strongest but also has large variations among samples (9.9–22.9%). The contribution of quartz, feldspars and pyrite to anisotropy is negligible. These elastic properties and velocities are only representative of the mineral polyphase aggregate and do not include the effects of porosity, interlayer water, fluid or kerogen fill.

5.4.4) Ultrasonic Velocities

Velocities measured at slight overpressure conditions ($Qu_{US\text{-}OP}$) and at *in-situ* stress conditions ($Qu_{US\text{-}is}$) are shown in Table 5.6. At over-pressure conditions, the maximum P-wave velocity is 5.31 km/s while the minimum is 4.03 km/s, with an anisotropy of 27.4%. The values at the *in-situ* stress conditions are only slightly higher, with Vp maximum is 5.33 km/s and the minimum 4.09 km/s, yielding 26.3% anisotropy. The increase with net stress is relatively small and has a minor impact on the P-wave anisotropy. Because of the axial sample symmetry, the S-wave traveling along the cylinder axis (axial wave) has no splitting because the S-wave velocity (2.10–2.14 km/s) is independent of polarization. The experimental uncertainty in the measured values is ~1%. P- and S-wave velocities have also been recorded in the well by wire-line measurements. Mud pressure in the well was higher than the estimated fluid pressure at that depth, which may have affected the P- and S-wave velocities in the borehole walls

The ultrasonic measurement gives a quantitative measure of the order of magnitude of the effect to be expected. The P-wave velocity from wire-line logs in the cored well, which would be equivalent to Vp at 90° to the bedding plane in the laboratory test, was measured to be around 3.76 km/s. This is about 8% lower than the velocity determined from the core plug (Table 5.6, Qu_{Wire}). Similarly, the shear velocity as measured in the wire-line is some 1.96 km/s, again about 8% lower than the velocity measured in the core plug. This difference between sonic and ultrasonic

measurements is substantially higher than the difference in velocities measured in ultrasonic measurements at *in-situ* conditions and at slight overpressure conditions. The discrepancy between ultrasonic and sonic velocities is most likely due to the difference in temperature (100◦ C *in-situ* versus room temperature in the laboratory, e.g., Johnston (1986) and Manafov et al. (2007)) and in the frequency used for the measurements (10 kHz versus 1 MHz).

Table 5.6: Elastic properties e.g. wave velocities from calculation (row 1-3) and from measurement (row 4-5), anisotropy%, and Thomsen's parameters are displayed.

Sample	Clay (vol%)	Averaging model	V_p min (km/s)	V_p max (km/s)	V_p min (km/s)	Ani. (%)	ε	γ	δ
Qu1	67.15	Voigt	3.87	6.80	5.90	14.2	0.16	0.12	0.11
		Reuss	3.20	5.69	5.17	9.6	0.11	0.10	0.05
		Hill	3.50	6.19	5.50	11.8	0.13	0.10	0.07
		Geometric	3.47	6.28	5.44	14.3	0.16	0.12	0.10
Qu2	72.52	Voigt	3.94	6.64	6.14	7.8	0.09	0.05	0.05
		Reuss	3.25	5.77	5.27	9.1	0.06	0.05	0.04
		Hill	3.51	6.06	5.63	7.4	0.08	0.06	0.04
		Geometric	3.48	6.12	5.59	9.1	0.09	0.06	0.05
Qu3	73.48	Voigt	3.87	6.84	6.01	12.9	0.15	0.09	0.09
		Reuss	3.18	5.72	5.21	9.3	0.10	0.09	0.04
		Hill	3.49	6.23	5.58	11.0	0.12	0.09	0.07
		Geometric	3.45	6.29	5.52	12.0	0.15	0.11	0.08
Qu_{AVE}	72.05	Voigt	3.89	6.76	6.02	11.6	0.13	0.08	0.08
		Reuss	3.21	5.73	5.22	9.32	0.09	0.08	0.04
		Hill	3.50	6.16	5.57	10.1	0.11	0.08	0.06
		Geometric	3.47	6.23	5.52	12.1	0.13	0.10	0.08
$Qu_{US\text{-}OP}$ (overpressure condition)	-	-	2.10	5.31	4.03	27.4	0.37	-	-
$Qu_{US\text{-}is}$ (in-situ condition)	-	-	2.14	5.33	4.09	26.3	0.35	-	-
Qu_{Wire} (wire-logging)	-	-	1.96		3.76				

5.5) DISCUSSION

5.5.1) Preferred Orientation

Three diagenetic shales from the Silurian Qusaiba formation were analyzed for LPO and SPO, mainly relying on synchrotron X-ray experiments. The samples have similar mineralogical composition, with the members of the illite-group dominating (33–42 wt%). Kaolinite is also abundant in the samples with approximately 25–28 wt%. The LPO of kaolinite, illite-mica, illite-smectite and chlorite were quantified with (001) pole figure maxima ranging from 2.4–6.8 m.r.d (Fig. 5.4). The degree of LPO for illite and kaolinite observed here are similar to previous synchrotron studies for Posidonia Shale (See Chapter 3: 3.7-6.3 m.r.d.), Kimmeridge North Sea shale (Wenk et al. 2010, 2–6 m.r.d.), Callovo- Oxfordian shales and Opalinus clay from Central Europe (Wenk et al. 2008a,b, 2–9 m.r.d.), shales from Nigeria (Lonardelli et al. 2007, 2–5m.r.d.) and shales from Silver Hill, Montana (Wenk et al. 2007, 10 m.r.d.). This also agrees with data obtained by pole figure

goniometry for shales/siltstones from the Barnett Shale (Day-Stirrat et al. 2010, 2-7 m.r.d.), North Sea (Valcke et al. 2006, 3–5 m.r.d.), Gulf Coast mudstones (Ho et al. 1999, 2–7 m.r.d.) and Zechstein shales (Sinbutin 1994a, 4–6 m.r.d.) but the anisotropy is considerably weaker than the one encountered in metamorphic slates (Sinbutin 1994b, 5–18 m.r.d. and Oertel and Phakey 1972, 16 m.r.d.) and schists (Wenk et al. 2010, 7–14 m.r.d.).

Overlapping peaks of authigenic illite-smectite are successfully separated from detrital illite-mica. Fine-grained authigenic illite-smectite has a lower degree of LPO than coarser detrital llite-mica. A strong degree of LPO is generally related to a high amount of clay content (Voltolini et al. 2009). Qu3 has the largest amount of clay (73.8 wt%) and displays the highest degree of LPO for chlorite and kaolinite. However, the (001) pole figure maximum of illite-mica in Qu1 is the highest among all phases (6.8 m.r.d., Table 5.3), even though it has a lower clay content (65.9 wt%). Aside from the dependency on the percentage of clay, the degree of LPO may be related to burial and compaction history and local heterogeneities. All samples were acquired within a few feet of each other and thus overall burial is identical. Illite-smectite is more poorly oriented than other clays as shown in the SEM image (Fig. 5.2) and observed from a broad and weak peak at ~10°A in the diffraction profile (Fig. 5.3). This authigenic clay has a very small size and represents most of the background material in the SEM images, which indeed show little orientation, in contrast to the detrital illite-mica flakes, which can be easily distinguished and are orientated perpendicular to the maximum vertical compaction stress. The pole densities of illite-smectite range from 2.4–4.0 m.r.d, which is considerably lower than those of illite-mica. The orientation distributions of quartz, K-feldspars and pyrite are nearly random and close to 1 m.r.d. A considerable portion of crystallites is randomly oriented as expressed by (001) minima of 0.2–0.4 m.r.d. for clay minerals.

5.5.2) Elastic Anisotropy

Illite-mica, chlorite and kaolinite have higher calculated Vp velocities and stronger anisotropy in comparison to illite-smectite (Fig. 5.6a), consistent with higher single crystal stiffness and higher degree of LPO. The shear-wave splitting (Vs) of chlorite, kaolinite and illite-mica is relatively high for waves propagating in the bedding plane (Fig. 5.6b, 90◦) and consistent with other observations Wenk et al. 2008b; Voltolini et al. 2009). The complex behavior for kaolinite can be explained with the large values of non-diagonal stiffness coefficients, which is a consequence of the triclinic kaolinite structural model used by Militzer et al. (2011).

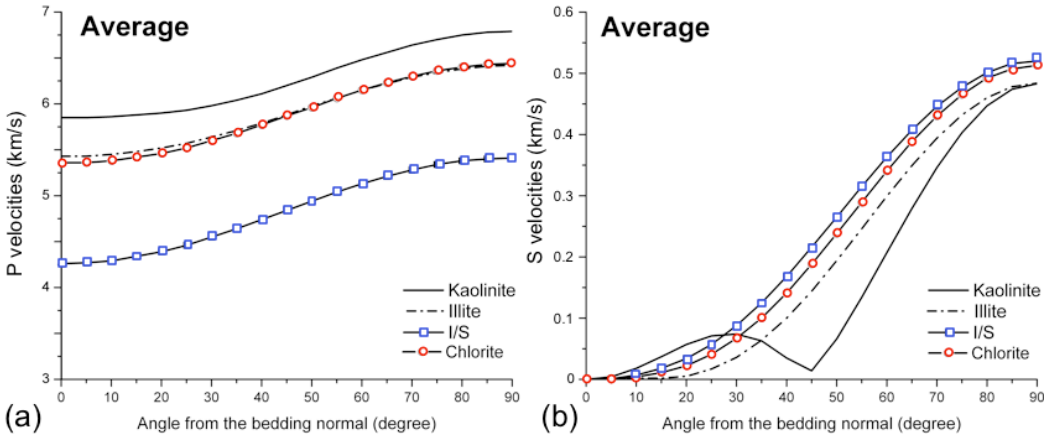

Figure 5.6: The average calculated (a) compressional velocities (V_p) and (b) shear wave splitting (ΔV_s) in km/s of individual clays and the polycrystal average versus the angle from the bedding normal plane. Geometric mean is used for the averaging.

Calculated P-wave anisotropies with geometric mean are ranging from 9.1–14.3% (Table 5.6, Fig. 5.7). The predicted anisotropies are comparable with other reports on calculated velocities of natural shales from the North Sea (Valcke 2006, 12%) and shales from Nigeria (Lonardelli et al. 2007, 10%) but relatively weaker than Mont Terri shale (Wenk et al. 2008a, 20%) and measured velocities for Kimmeridge shale (Hornby 1998, 38%). The anisotropic properties can be expressed in terms of Thomsen's parameters (Thomsen 1986), which assume transverse isotropy, i.e., axial symmetry around the bedding plane normal.

$$\varepsilon = \frac{(C_{11} - C_{33})}{2C_{33}}$$

$$\gamma = \frac{(C_{66} - C_{55})}{2C_{55}}$$

$$\delta = \frac{(C_{13} + C_{55}) - (C_{33} - C_{55})}{C_{33}(C_{33} - C_{55})}$$

These parameters are used to characterize P- and S-wave propagation through a weakly anisotropic medium. Average values calculated for the Qusaiba samples are given in Table 5.6. P-wave anisotropy (9.1–14.3%) is associated with anisotropy parameters ε (0.10–0.16) while parameter γ (0.07–0.12) is a measure of S-wave anisotropy. The Thomsen parameter δ (0.08–0.10) is related to the near-vertical P-wave velocity and is used to explain the discrepancy between vertical velocity and small-offset normal moveout (NMO) velocity and to understand small-offset amplitude variation with an offset (AVO) response. The calculations show comparable anisotropy to shale samples from the North Sea, Africa and the Gulf Coast with parameters ε (0.08–0.33), γ (0.11–0.53) and δ (–0.05–0.23) (Wang 2002) but relatively higher than shales from the Nigerian Coast with anisotropy parameters ε (0.03–0.07), γ (0.01–0.10) and δ (–0.03–0.03) (Lonardelli et al. 2007).

A significant difference exists between the velocities as computed for the polyphase aggregate and the velocities determined experimentally in ultrasonic measurements and sonic measurements in the borehole (Table 5.6). Experimental values for P-wave velocities in the bedding plane are 14% lower than calculated ones (V_{pmax} in Fig. 5.7). Velocities perpendicular to the bedding plane as measured by sonic in the borehole and in the ultrasonic experiments (V_{pmin}) are 27% lower and correspondingly anisotropy is higher. This highlights the fact that different factors influence elastic properties of aggregates. One of them is LPO of the component crystals (the polyphase aggregate) and another one is the SPO of the minerals and low density features, including pores, fractures and organic materials as illustrated in Fig. 5.5. Simple modelling of the elastic properties indicates that these differences are well within the limits to be expected and also suggests causes for this discrepancy. The layered alternation of kerogen-rich and less kerogen-rich layers is unlikely the cause of major differences. The elastic properties of kerogen are largely unknown and different estimates can be found in the literature (e.g., Rundle and Schuler 1981; Vernik and Liu 1997; Mavko, Mukerji and Dvorkin 1998). Modeling of the unrealistic scenario of interlayering of pure kerogen with the shale polyphase aggregate can be done by Backus averaging (Backus 1962) and the anisotropy increases in such a case. But only when a kerogen type with very low stiffness is selected, compressional and shear velocities along the symmetry axis are obtained that are of the same order of magnitude as the measured velocities. The fastest (radial) velocity is hardly affected in such geometry and the interbedding of the kerogen and polyphase aggregate can be ruled out as a single source of the velocity reduction.

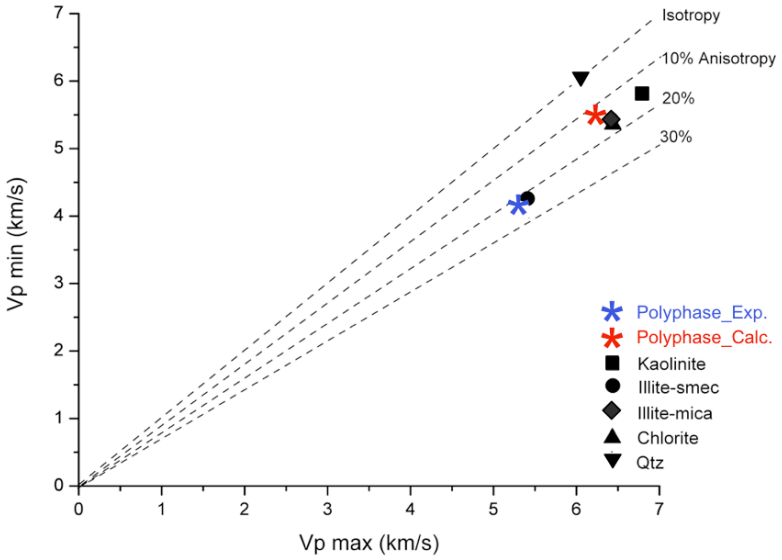

Figure 5.7: The experimental minimum and maximum P-wave velocities and calculated average of each phase component and polyphase average. The dashed lines indicate degrees of anisotropy.

An alternative explanation for the softening of the polyphase aggregate is the loss of coherence between crystals affected by porosity, interlayer water and kerogen (Hornby et al. 1994). Bound water and kerogen are independent mechanisms tying crystals together in addition to the clay cement. Aylmore et al. (1960) argued that nanometer-sized porosity should be considered as the porosity between crystal plates and hence the porosity will align with the crystal structure. Katahara (1996) saw this effect as a reason for the discrepancy between elastic properties deduced from LPO measurements and the elastic properties as deduced from direct velocity measurements. The strong anisotropy at the nm scale is also in-line with the observation that the μm scale porosity is anisotropic (Fig. 5.5a), which is related to the weakness in the axial direction relative to the radial direction.

In a realistic averaging model, the SPO of constituent phases (i.e., grain shape, grain orientation, volume, shape and alignment of pores) needs to be considered, which is not done in simple averaging schemes. Currently, self-consistent methods are being developed for this (e.g., Matthies 2010), but are beyond the scope of this work. These methods are based on more empirical full effective medium modeling (by e.g., Hornby 1994; Hornby et al. 1994; Johansen, Ruud and Jakobsen 2004; Draege, Jakobsen and Johansen 2006) but incorporate quantitative crystal preferred orientation. An approximation can be obtained by using a Voigt-Reuss-Hill average to calculate the properties of the matrix with the kerogen inclusions and adding the porosity as cracks parallel to the bedding plane, with an aspect ratio of the order of 0.03 (Cheng 1993). Given the uncertainties in kerogen properties, exact porosity value and the anisotropy caused by the interbedding of kerogen layers, such a solution is far from unique. The different in calculated and measured anisotropy is largely due to anisotropic porosity and open fracture distribution that affect mainly the lower V_{pmin} values. The degree of porosity and fractures are crucial factors that should be considered in the system. During compaction by overburden (axial compression), porosity diminishes and clay platelets become more aligned. The more sophisticated models that consider porosity (Bayuk, Ammerman and Chesnokov 2007), fracture distribution (Sayers 1998), saturation (Pham et al. 2002) and frequency dependency (Sams et al. 1997), which can contribute to anisotropy, may be of use to tie the calculated matrix properties to the velocities measured in ultrasonic measurements.

The LPO can also be used to estimate the compaction strain in the system. Based on March's method (March 1932), it is assumed that preferred orientation of originally randomly oriented rigid platelets embedded in a viscous matrix when the composite is homogeneously strained. Oertel and Curtis (1972) later modified the original March model for compaction by taking a volume change into account. The compaction strain (ε_c) is expressed in terms of the maximum pole density (ρmax) as $\varepsilon_c = \rho_{max}^{-1/2} - 1$. The maximum (001) pole densities of each phase are used to calculate the March strain (Table 5.7). The calculated compaction strain values (–0.36 to –0.61) are comparable to that of 75–100 wt% clay in the compression experiment of Voltolini et al. (2009), which found that with 5 MPa compression on 75–100wt% clay, the compaction strains range from –0.35 to –0.51. With higher pressure applied, as much as 50 MPa, the compaction strains were –0.48 to –0.65. This suggests that the Qusaiba shales had undergone an extensive compaction history. The slight variation between the three samples and clay minerals is to natural heterogeneities and different crystal shapes. To estimate the compaction strain, the LPO of detrital illite-mica is probably the most reliable, because they constitute relatively large platelets in a fine-grained matrix.

Table 5.7. Estimated compaction strain (ε_c) values from maximum pole densities (ρ_{max}) of kaolinite, illite-smectite, illite-mica and chlorite. ($\varepsilon_c = \rho_{max}^{-1/2} - 1$)

Sample	Kaolinite		Illite-Smectite		Illite-Mica		Chlorite	
	ρ_{max}	ε_c	ρ_{max}	ε_c	ρ_{max}	ε_c	ρ_{max}	ε_c
Qu1	4.81	-0.54	3.97	-0.50	6.75	-0.62	5.61	-0.58
Qu2	4.41	-0.52	2.42	-0.36	3.23	-0.44	3.56	-0.47
Qu3	6.49	-0.61	3.31	-0.45	4.56	-0.53	5.77	-0.58

5.6) CONCLUSIONS

The microscopic observation of microstructural features is combined with an evaluation of macroscopic properties of deeply buried shale subjected to compaction and diagenesis. With the use of synchrotron X-ray diffraction, the quantitative LPO of kaolinite, illite-mica, illite-smectite and chlorite in the Qusaiba Shale is obtained. Main factors contributing to the degree of LPO is the clay content, burial, and compaction. Kaolinite, illite-mica and chlorite generally exhibit strong LPO while nanocrystalline illite-smectite shows weaker alignment. The elastic properties of Qusaiba Shale are also calculated from microstructure data. However, the distribution of kerogen and more importantly the orientation of the microfracture and porosity network are not included in the model. These features reduce the strength of the matrix, enhancing the anisotropy and these porosity-related effects are significant contributors to the elastic anisotropy. Through linking the matrix and porosity components, a more comprehensive model of shale elastic properties is thus necessary for further study.

SUMMARY & FUTURE DIRECTIONS

The development of LPO in Zn, Cd, Os, and Hf at high pressure and temperature is investigated in Chapter 2. Deformation experiments in the rDAC and D-DIA apparatus show that the *c*-axes of all hcp metals preferentially orient near the compression axis. Textures in Zn and Cd are initially developed by basal slip. At higher pressure, slip may be accompanied by tensile twinning when the *c*/*a* ratio of Zn and Cd decreases below the critical value. In contrast, a rapid texture evolution in Os and Hf evolves mainly due to tensile twinning. At high temperature, tensile twinning is suppressed and texturing is activated by basal and prismatic slip. Under all conditions, slip appears to be the main deformation mechanism in hcp metals at extreme conditions. These finding are consistent to those of hcp-Fe and useful to better understand the deformation mechanisms of hcp metals and their implications to elastic anisotropy in the Earth's inner core.

Chapter 3 addresses factors that influence texture development of clay minerals in the Posidonia Shale from the Hils syncline in Northern Germany, subjected to different local histories. The texture of kaolinite, illite-mica, illite-smectite, and calcite was quantified by synchrotron X-ray diffraction techniques, followed by Rietveld refinement. The degree of LPO of clays and calcite in all four samples with different maturity history is comparable (3.7-6.3 m.r.d.). Kaolinite and illite-mica (3.9-6.3 m.r.d.) generally exhibit stronger preferred orientations than microcrystalline illite-smectite (3.7-4.6 m.r.d.). The difference in local history, which causes significant changes in the maturity of organic matter, did not influence the LPO to a large extent and thus most of mineral preferred orientation evolved rather early.

Chapter 4 focuses on the quantification of 3D internal features and distribution of low density features, including pores, fractures, and kerogen, as well as other phases such as pyrite in shales by the SXMT technique. Low density features are generally anisotropic and aligned parallel to the bedding plane whereas pyrite is dispersed throughout the sample. Shales are challenging samples because many microstructural features are in the micron scale, at the limit of the resolution. The sharpness of phase boundaries in the reconstructed data collected from the APS and SLS was comparable and slightly more refined than in the data obtained from the ALS. The discrepancy of data quality and volume fractions is contributed by different types of optical instruments and varying technical setups at each facility.

In Chapter 5, the microscopic observation of microstructural features is combined with an evaluation of macroscopic properties of deeply buried shale subjected to compaction and diagenesis. With the use of synchrotron X-ray diffraction and microtomography, the information about LPO and SPO of different phases in Qusaiba Shale are quantified. The SPO of low density features here is anisotropic and consistent with that of Posidonia Shale. For LPO, Kaolinite, illite-mica and chlorite generally exhibit stronger alignment than the alignment of illite-smectite. Main factors

contributing to the high degree of LPO of Qusaiba Shale is the clay content, burial, and compaction. Mineral orientation distributions are then used to calculate the elastic properties of shales. However, the distribution of kerogen, microfracture, and porosity network are not included in the model. These features reduce the strength of the matrix, enhancing the anisotropy and these porosity-related effects are significant contributors to the elastic anisotropy. Through linking the matrix and porosity components, a more comprehensive model of shale elastic properties is thus necessary for further study.

In conclusion, state-of-the-art synchrotron X-ray techniques and the Rietveld refinement in MAUD are proven to be valuable tools to address fundamental questions about preferred orientation and elastic anisotropy. This dissertation particularly describes the rDAC and D-DIA applications to hcp metals and provides information about rheology of minerals in Earth's inner core. Beyond the scope of this thesis, mantle minerals such as perovskite (Wenk et al. 2004), and post-perovskite (pPV) (Merkel et al. 2006, Merkel et al. 2007, Miyagi et al. 2010) have been extensively studied with these techniques. However, texture and deformation mechanisms of polyphase assemblages in the mantle (e.g. perovskite and magnesiowuestite) are poorly understood. The interaction of polyphase assemblages under extreme conditions, and the texture development upon phase transformation have remained controversial. With the improvement of technology such as gasket design and combined laser and resistive heating system, higher pressure and temperature ranges can be achieved in the experiment. A further study on these minerals is thus necessary for a better understanding of rheology and seismic anisotropy in the deep Earth.

The application of synchrotron X-ray diffraction and microtomography techniques to shales illustrates the importance of microstructural data quantification at high resolution. Nevertheless, many questions about shales still remain unanswered; for instance, what is the 3D structure of nanopores at high pressure and temperature? what are the elastic properties of kerogen-types, maturity? how do these factors affect elastic properties in shales and can we accurately predict them?

Limitations on spatial resolution of SXMT and different sources of artifacts as well as bluriness introduce challenges into visualization and quantitative extraction of constituent phases in shales with a wide range of grain sizes and phases of different absorption characteristics. SXMT methods may be complemented with nanoscale approaches such as transmission electron microscopy (TEM) (Midgley et al. 2007), focused ion beam scanning electron microscopy (FIB-SEM) (Elfallagh and Inkson 2009; Keller et al. 2011; Bera et al. 2011), and X-ray nanotomography (Nelson et al. 2011; Grew et al. 2010). Further study of porosity and appropriate statistical averaging methods are necessary for understanding macroscopic physical properties of shales in detail. In addition, a high-resolution tomography apparatus that can simultaneously heat and compress shales while collecting tomographic images needs to be investigated. The changes of 3D distribution of kerogen and pores upon elevated pressure and temperature can then be described in their most natural conditions. Moreover, a self-consistent averaging based on more empirical full effective medium modelling (by e.g., Hornby 1994; Hornby et al. 1994; Johansen, Ruud and Jakobsen 2004; Draege, Jakobsen and Johansen 2006) needs to be incorporated for elastic properties calculations. With all information combined, a rock physics model can be better-constrained and used to resolve issues on the macroscopic scale.

REFERENCES

van Aarle, W. and Batenburg, K.J. (2011) Optimal threshold selection for segmentation of dense homogenous objects in tomographic constructions. *IEEE Trans Medical Imaging,* 30, 980-989.

Agatston, A. S., Janowitz, W. R.,Hildner, F. J., Zusmer, N. R., Viamonte, M. and Detrano, R. (1990) Quantification of coronary artery calcium using ultrafast computed tomography. *J. Am. Col. Cardiol.* 15, 827-832.

Agnew, S.R., Tomé, C.N., Brown, D.W., Holden, T.M. and Vogel, S.C. (2003) Study of slip mechanisms in a magnesium alloy by neutron diffraction and modeling. *Sc. Mater.* 48, 1003-1008.

Al-Harbi, O.A. (1998) Petrography and diagenetic controls on reservoir characteristics in Unayzah Formation, Central Saudi Arabia. *JKAU:Earth Science* 10, 45–57.

Aplin, A.C. and Larter S.R. (2005) Fluid flow, pore pressure,wettability and leakage in mudstone cap rocks. In: Evaluating Fault and Cap Rock Seals (eds P. Boult and J. Kaldi), pp. 1–12. AAPG.

Aplin, A.C., Matenaar, I.F., McCarty, D.K. and van der Pluijm, B.A. (2006) Influence of mechanical compaction and clay mineral diagenesis on the microfabric and pore-scale properties of deep-water Gulf of Mexico mudstones. *Clays Clay Min.* 54, 500-514.

Armentrout, M. and Kavner, A. (2010) Incompressibility of osmium metal at ultrahigh pressures and temperatures. *J. Appl. Phy.* 107, 093528.

Avizo®, Visualization Sciences Group, Burlington, Massachusetts USA: www.vsg3d.com

Aylmore, L. and Quirk, J.P. (1960) Domain or turbostratic structure of clays. *Nature* 187, 1046–1048.

Bachrach, R. (2011) Elastic and resistivity anisotropy of shale during compaction and diagenesis: Joint effective medium modeling and field observations. *Geophysics*, 76, E175-E186.

Backus, G.E. (1962) Long-wave elastic anisotropy produced by horizontal layering. *J. Geophys. Res.* 67, 4427–4440.

Baker, D.W., Chawla, K.S. and Krizek, R.J. (1993) Compaction fabrics of pelites: experimental consolidation of kaolinite and implications for analysis of strain in slate. *J. Struct. Geol.,* 15, 1123-1137.

Baruchel, J., Buffière, J.Y., Maire, E., Merle, P. and Peix, G. *X-ray tomography in Material Science* (Hermes Science Publications, Paris, 2000).

Bayuk, I.O., Ammerman, M. and Chesnokov, E.M. (2007) Elastic moduli of anisotropic clay. *Geophysics* 72, D107–D117.

Beckmann, F., Grupp, R., Haibel, A., Huppmann, M., Nöthe, M., Pyzalla, A., Reimers, W., Schreyer, A. and Zettler, R. (2007) In-situ synchrotron X-ray microtomography studies of microstructure and damage evolution in engineering materials. *Adv. Eng. Mater.* 9, 939-950.

Bera, B., Mitra, S. K. and Vick, D. (2011) Understanding the microstructure of Berea Sandstone by the simultaneous use of Micro-Computed Tomography (micro-CT) and Focused Ion Beam-Scanning Electron Microscopy (FIB-SEM). *Micron* 42, 412-418.

Bernard, S., Horsfield, B., Schulz, H.-M., Schreiber, A., Wirth, R., Vu, T.T. A., Perssen, F., Könitzer, S., Volk, H., Sherwood, N. and Fuentes, D. (2010) Multi-scale detection of organic

signatures provides insights into gas shale properties and evolution. *Chemie der Erde*, 70, 119-133.

Bernard, S., Horsfield, B. , Schulz, H-M., Wirth, R., Schreiber, A. (2011) Geochemical evolution of organic-rich shales with increasing maturity: a STXM and TEM study of the Posidonia Shale (Lower Toarcian, nothern Germany). *Mar. Petrol. Geol.,*doi:10.1016/j.marpetgeo.2011.05.010.

Best, M.E. and Katsube, T. J. (1995) Shale permeability and its significance in hydrocarbon exploration. *The Leading Edge*, 14, 165-170.

Bilgili, F., Götze, H.-J., Pašteka, R., Schmidt, S. and Hackney R. (2009) Intrusion versus inversion-a 3D density model of the southern rim of the Northwest German Basin. *Int. J. Earth Sci.,* 98, 571-583.

Birch, F. (1947) Finite elastic strain of cubic crystals. *Phys. Rev.* 71,809-824.

Bish, D.L. (1993) Rietveld refinement of kaolinite structure at 1.5 K. *Clays Clay Min.*, 41, 738-744.

Bossart, P. and Thury, M. (2007) Research in the Mont Terri Rock Laboratory, quo vadis. *Phys. Chem. Earth* 32, 19–31.

Brabant, L., Vlassenbroeck, J., De Witte, W., Cnudde, V., Boone, M. N., Dewanckele, J. and Van Hoorebeke, L. (2011) Three-dimensional analysis of high-resolution X-ray computed tomography data with Morpho+. *Microsc. Microanal.* 17, 252-263.

Brown, D.W., Abeln, S.P., Blumenthal, W.R., Bourke, M.A.M., Mataya, M.C., and Tomé, C.N. (2005) Development of Crystallographic Texture during High Rate Deformation of Rolled and Hot-Pressed Beryllium. *Metall. Mater. Trans.* 36A, 929-939.

Brown, J.M. and McQueen, R.G. (1982) The equation of state for iron and the Earth's core. *High-P. Res. Geohys.* (S. Akimoto and M.H. Manghnani eds), pp. 611-623. Center Acad. Publ., Tokyo.

Brun, F., Mancini, L., Kasae, P., Favretto, S., Dreossi, D. and Tromba, G. (2010) Pore3D: a software library for quantitative analysis of porous media. *Nucl. Instrum. Methods Phys. Res.* 615, 326–332.

Busch, A., Alles, A., Gensterblum, Y., Prinz, D., Dewhurst, D., Raven, M. D., Stanjek, H. and Krooss, B. M. (2008) Carbon dioxide storage potential of shales. *Inter. J. Greenh. Gas Con.* 2, 297-308.

Cerreta, E., Yablinsky, C.A., Gray, G.T. III, Vogel, S.C. and Brown, D.W. (2007) The Influence of Grain Size and Texture on the Mechanical Response of High Purity Hafnium. *Mater. Sci. Engi. A.* 456, 243–251.

Chadwick, R.A., Zweigel, P., Gregersenc, U., Kirby, G.A., Holloway, S. and Johannessen, P.N. (2004) Geological reservoir characterization of a CO2 storage site. The Utsira Sand, Sleipner, northern North Sea. *Energy* 29, 1371–1381.

Cheng, C.H. (1993) Crack models for a transversely isotropic medium. *J. Geophys. Res.* 98, 675–684.

Clausen, B., Tomé, C.N., Brown, D.W., Agnew, S.R. (2008) Reorientation and stress relaxation due to twinning: Modeling and experimental characterization for Mg. *Acta Mater.* 56,2456-68.

Connolly, B. J., Horner, D. A., Fox, S. J., Davenport, A. J., Padovani, C., Zhou, S., Turnbull, A., Preuss, M., Stevens, N. P., Marrow, T. J., Buffière, J.-Y., Boller, E., Grošo, A. and Stampanoni, M. (2006) X-ray microtomography studies of localised corrosion and transitions to stress corrosion cracking. *Mater. Sci. Technol.* 22, 1076-1085.

Curtis, C.D., Lipshie, S.R., Oertel, G. and Pearson, M.J. (1980) Clay orientation in some Upper Carboniferous mudrocks, its relationship to quartz content and some inferences about fissility, porosity and compactional history. *Sedimentology*, 27, 333-339.

Curtis, M.E., Ambrose, R.J. and Sondergeld, C.H. (2010) Structural characterization of gas shales on the micro- and nano-Scales. Canadian unconventional resources and international petroleum conference. Calgary, Alberta, Canada.

Day-Stirrat, R., Loucks R.G., Milliken, K.L., Hillier, S. and van der Pluijm, B. (2008a) Phyllosilicate

orientation demonstrates early timing of compactional stabilization in calcite-cemented concretions in the Barnett Shale (Late Mississippian), Fort Worth Basin, Texas (U.S.A). *Sediment. Geol.*, 208, 27-35.

Day-Stirrat, R.J., Aplin, A.C., Srodon, J. and van der Pluijm, B.A. (2008b) Diagenetic reorientation of phyllosilicate minerals in Paleogene mudstones of the Podhale Basin, Southern Poland. *Clays Clay Mine,* 56, 100-111.

De Carlo, F. and Tieman, B. (2004) High-throughput x-ray microtomography system at the advanced photon source beamline 2-BM. *Development in X-ray IV*. U Bonse (Ed.) *Proc. SPIE,* 5535, 644-651.

Deng, X.H., Lu, W., Hu, Y.M. and Gu, H. (2009) The elastic properties of hexagonal osmium under pressure. *Phys B: Condens. Matter.* 404, 1218-1221.

Deutloff, O., Teichmüller, M., Teichmüller, R. and Wolf, M. (1980) Inkohlungsuntersuchungen im Mesozoikum des Massivs von Vlotho (Niedersächsisches Tektogen). *Neues Jahrb. Geol. Paläontol. Monatsh.,* 6, 321–341.

Dewhurst, D.N. and Siggins, A.F. (2006) Impact of fabric microcracks and stress field on shale anisotropy. *Geophys. J. Inter.* 165, 135–148.

Diamond, S. (2000) Mercury porosimetry. An inappropriate method for the measurement of pore size distributions in cement-based materials. *Cement Concrete Res.* 30, 1517–1525.

Dierick, M., Masschaele, B., and Van Hoorebeke, L. (2004) Octopus, a fast and user-friendly tomographic reconstruction package developed in Lab View®. *Meas Sci Technol,* 15, 1366-1370.

Doornenbal, J.C. and Stevenson, A.G. (eds) (2010), *Petroleum Geological Atlas of the southern Permian Basin Area*. European Association of Geoscientists and Engineers Publications BV., Houten, The Netherlands. 354pp.

Dowd, B.A., Campbell, G.H., Marr, R.B., Nagarkar, V., Tipnis, S., Axe., L. and Siddons, D. P. (1999) Developments in synchrotron X-ray computed microtomography at the National Synchrotron Light Source. in *Proc. SPIE*; *Vol. 3772*, edited by U. Bonse, Denver, CO, USA, p. 224.

Downs, R.T. and Hall-Wallace, M. (2003), The American Mineralogist Crystal Structure Database. *Am. Mineral.,* 88, 247-250.

Draege, A., Jakobsen, M. and Johansen, T.A. (2006) Rock physics modeling of shale diagenesis. *Petrol. Geosci.*, 12, 49-57.

Elfallagh, F. and Inkson, B.J. (2009). 3D analysis of crack morphologies in silicate glass using FIB tomography. *J. Eur. Ceram. Soc.,* 29, 47-52.

Fast, L., Ahuja, R., Nordstrom, L., Wills, J.M., Johansson, B., Eriksson, O. (1997) Anomaly in c/a ratio of Zn under pressure. *Phys. Rev. Lett.* 79, 2301-2303.

Fei, Y., Ricolleau., A., Frank, M., Mibe, K., Shen, G., Prakapenka, V. (2007) Toward an internally consistent pressure scale. *PNAS*. 104, 9182-9186.

Fjaer, E., Holt, R.M., Horsrud, P., Raaen, A.M. and Risnes, R. (2008) Petroleum Related Rock Mechanics, 2nd edn. Elsevier.

Fusseis, F., Regenauer-Lieb, K., Liu, J., Hough, R.M. and De Carlo, F. (2009) Creep cavitation can establish a dynamic granular fluid pump in ductile shear zones. *Nature* 459, 974-977.

Fusseis, F. Schrank, C., Liu, J., Karrech, A., Llana-Fúnez, Xiao, X., Regenauer-Lieb, K. (2012) Pore formation during dehydration of a polycrystalline gypsum sample observed and quantified in a time-series synchrotron X-ray micro-tomography experiment. *Solid Earth* 3, 71-86.

Friedrich, J. M., P.Wignarajah, D., Chaudhary, S., Rivers, M. L., Nehru, C. E. and Ebel, D. S. (2008) Three-dimensional petrography of metal phases in equilibrated L chondrites – effects of

shock loading and dynamic compaction. *Earth Planet. Sci. Lett.* 275, 172–180.
Gualtieri, A.F. (2000) Accuracy of xrpd qpa using the combined Rietveld-rir method. *J. Appl. Crystall.*, 33, 267-278.
Gai, Z., Donoghue, P. C. J., Zhu, M., Janvier, P. and Stampanoni, M. (2011) Fossil jawless fish from China foreshadows early jawed vertebrate anatomy. *Nature* 476, 324-327.
Garland, C.W. and Silverman, (1960) Elastic constants of cadmium from 4.2 K to 300 K. *J. Phys. Rev.* 119,1218-1222.
Grew, K. N., Chu, Y. S., Yi, J., Peracchio, A. A., Izzo Jr., J., Hwu, Y., De Carlo, F. and Chiu, W. K. S. (2010) Nondestructive Nanoscale 3D Elemental Mapping and Analysis of a Solid Oxide Fuel Cell Anode. *J. Electrochem. Soc.* 157, B783-B792.
Gschneidner, K Jr. (1964) Physical Properties and Interrelationships of Metallic and Semimetallic Elements. *Solid State Phys.* 16,275-426.
Hammersley, A.P. (1998) Fit2D. V12.012 reference manual. Version 6.0., European Synchrotron Radiation Facility, Internal Report ESRF98HA01T. (www.esrf.ed/computing/scientific/FIT2D).
Hao, Y.J., Zhu, J., Lin, Z., Ren, H.S., Qu, J.Y. (2010) Structure phase transition and elastic properties of halfnium: first-principles study. *Philos. Mag. Lett.* 91,1-9.
Hashin, Z. and Strickman, S. (1963) A variational approach to the theory of the elastic behavior of multiphase materials. *J. of Mech. Phys. Solids.* 11,127-140.
Heim, S., Guttmann, P., Rehbein, S., Werner, S., Schneider, G. (2009). Energy-tunable full-field X-ray microscopy. Cryo-tomography and full-field spectroscopy with the new BESSY TXM. *J. Phys.: Conference Series,* 186, 012041.
Heyliger P., Ledbetter, H. and Kim, S. (2002) Elastic constants of natural quartz. *J. Acoust. Soc. Am.* 114, 644–650.
Hill, R. (1963) Elastic properties of reinforced solids: Some theoretical principles. *J. Mech. Phys. Solids* 11, 357–372.
Hintermüller, C., Marone, F., Isenegger, A. and Stampanoni M. (2010) Image processing pipeline for synchrotron-radiation-based tomographic microscopy. *J. Synchrotron Radiat.* 17, 550-559.
Ho, N.-C., Peacor, D.R. and van der Pluijm, B.A. (1995) Reorientation of phyllosilicates in mudstones-to-slate transition at Lehigh Gap, Pennsylvania. *J. Struct. Geol.*, 17, 345-356.
Ho, N.-C., Peacor, D.R. and van der Pluijm, B.A. (1999) Preferred orientation of phyllosilicates in Gulf Coast mudstones and relation to the smectite-illite transition. *Clays Clay Min.*, 47, 495-504.
Holzner, C., Feser, M., Vogt, S., Hornberger, B., Baines, S.B. and Jacobsen, C. (2010) Zernike phase contrast in scanning microscopy with X-rays. *Nature Phys.* 6, 883-887.
Hornby, B.E. (1994) The elastic properties of shales. PhD thesis, University of Cambridge.
Hornby, B.E., Schwartz, L. M. and Hudson, J.A. (1994). Anisotropic effective-medium modelling of the elastic properties of shales. *Geophysics* 59, 1570–1583.
Hornby, B.E. (1998) Experimental laboratory determination of the dynamic elastic properties of wet, drained shales. *J. Geophys. Res.* 103, 29945–29964.
Hutchinson, J.W. (1976) Bounds and self-consistent estimates for creep of polycrystahe materials. *Proc R Soc* London. 348,101-127.
Jakobsen, M. and Johansen, T.A. (2000) Anisotropic approximations for mudrocks: A seismic laboratory study. *Geophysics* 65, 1711–1725.
Jeanloz, R., Wenk, H.-R. (1988) Convection and anisotropy of the inner core. *Geophys. Res. Lett.* 15,72-75.
Jenkins, C.D. and Boyer II, C.M. (2008) Coalbed- and Shale-Gas Reservoirs. *J. Petrol. Technol.,* 60, 92-

99.

Johansen, T. A., Ruud, B.O. and Jakobsen, M. (2004) Effect of grain scale alignment on seismic anisotropy and reflectivity of shales. *Geophys. Prospect.*, 52, 133-149.

Johnston, D.H. (1987) Physical properties of shale at temperature and pressure. *Geophysics* 52, 1391–1401.

Joswig, W., Fuess, H., Rothbauer, R., Takeuchi, Y. and Mason, S.A. (1980) A neutron diffraction study of a one-layer triclinic chlorite (penninite). *Am. Mineral.* 65, 349–352.

Kanitpanyacharoen, W., Kets, F.B., Wenk, H.-R., Lehr, C., and Wirth, R. (2011) Texture and anisotropy of Qusaiba Shales, Saudi Arabia. *Geophys. Pros.,* 59,536-556.

Kanitpanyacharoen, W., Merkel, S., Miyagi, L., Kaercher, P., Tomé, C.N., Wang, Y., Wenk, H.-R. (2012a) Significance of mechanical twinning in hexagonal metals at high pressure. *Acta Mat.,* 60,422-430.

Kanitpanyacharoen, W., Kets, F.B., Wenk, H.-R. and Wirth, R. (2012b) Mineral Preferred orientation and microstructure of Posidonia Shale in relation to different degrees of thermal maturity. *Clays Clay Min.,* 60,315-329.

Kanitpanyacharoen, W., Parkinson, D., De Carlo, F., Marone, F., Stampanoni, M., Mokso, R., MacDowell, A., and Wenk, H.-R. (2013) A comparative study of X-ray microtomography on shales at different synchrotron facilities: ALS, APS, and SLS. *J. Synchr. Rad.,* 20,1-9.

Karato, S. (1999) Seismic anisotropy of the Earth's inner core resulting from flow induced by Maxwell stresses. *Nature (London)* 402, 871.

Katahara, K.W. (1996) Clay mineral elastic properties. 66th SEG meeting, Denver, Colorado, USA, Expanded Abstracts, 1691–1694.

Keller, L.M., Holzer, L. Wepf, R. and Gasser, P. (2011) 3D Geometry and topology of pore pathways in Opalinus clay: Implications for mass transport, *Appl. Clay Sci.,* 52, 85-95.

Ketcham, R. A. (2005) Computational methods for quantitative analysis of three-dimensional features in geological. *Geosphere.* 1, 32-41.

Kocks, U.F., Tomé C.N. and Wenk, H.-R. (2000) Texture and Anisotropy. Preferred Orientations in Polycrystals and Their Effect on Material Properties. Cambridge University Press.

Kus, J., Cramer, B. and Kockel, F. (2005) Effects of a Cretaceous structural inversion and a postulated high heat flow event on petroleum systerm of the western Lower Saxony Basin and the charge history of the Apeldorn gas field. *Neth. J. Geosci.,* 84, 3-24.

Lebensohn, R.A. and Tomé, C.N. (1993) A self-consistent approach for the simulation of plastic deformation and texture development of polycrystals: application to Zirconium alloys. *Acta Mater.* 41,2611.

Ledbetter, H.M. (1977) Elastic constants of polycrystalline copper at low temperatures. Relationship to single-crystal elastic constants. *Phys. Status Solidi B.* 181,81.

Lenoir, N., Bornert, M., Desrues, J., Besuelle, P. and Viggiani, G. (2007) Volumetric Digital Image Correlation Applied to X-ray Microtomography Images from Triaxial Compression Tests on Argillaceous Rock. *Strain* 43, 193-205.

Leythaeuser, D., Alterbaeumer, F.J. and Schaefer, R.G. (1980) Effect of an igneous intrusion on maturation of organic matter in Lower Jurassic shales from NW-Germany. *Phys. Chem. Earth,* 12, 133-139.

Liermann, H.P., Merkel, S., Miyagi, L., Wenk, H.-R., Shen, G., Cynn, H. and Evans, W.J. (2009) Experimental method for in situ determination of material textures at simultaneous high pressure and high temperature by means of radial diffraction in the diamond anvil cell. *Rev. Sci. Instru.* 80,104501.

Lindquist, W. B., Venkatarangan, A., Dunsmuir, J. & Wong, T.-F. (2000) Pore and throat size distributions measured from sychrotron X-ray tomographic images of Fontainebleau sandstones. *J. Geophys. Res.* 105B, 21508-21528.

Lindquist, W. B. (2002b) Quantitative analysis of three-dimensional X-ray tomographi images. in *Proc. of SPIE Vol. 4503* edited by U. Bonse, Seattle, WA, USA, p. 103.

Littke, R. and Rullkötter, J. (1987) Mikroskopische und makroskopische Unterschiede zwischen Profilen unreifen und reifen Posidonienschiefers ans der Hilsmulde. *Facies*, 17, 171-180.

Littke, R., Baker, D.R., Leythaeuser, D. (1988) Microscopic and sedimentologic evidence for the generation and migration of hydrocarbons in Toarcian source rocks of different maturities. *Org. Geochem.,* 13, 549-559.

Littke, R., Baker, D.R., Leythaeuser, D., Rullkötter, J. (1991) Keys to the depositional history of the Posidonia Shale (Toarcian) in the Hils Syncline, northern Germany. *Geol. Soc., London, Special Publications,* 58, 311-333.

Littke, R., Baker, D.R., Rullkötter, J. (1997) Deposition of petroleum source rocks. In: Welte, D.H., Horsfield, B., Baker, D.R. (Eds.). *Petrol. Basin Evol.*. Springer, Heidelberg, pp. 271-333.

Lonardelli, I., Wenk, H.-R. and Ren, Y. (2007) Preferred orientation and elastic anisotropy in shales. *Geophysics*, 72, D33-D40.

Loucks, R.G., Reed, R.M., Ruppel, S., Jarvie, D.M. (2009) Morphology, genesis, and distribution of nanometer-scale pores in siliceous mudstones of the Mississippian Barnett Shale. *J. Sediment. Res.,* 79, 848-861.

Lutterotti, L., Matthies, S., Wenk, H.-R., Shultz, A.J. and Richardson, J.W. (1997) Combined texture and structure analysis of deformed limestone from time-of-flight neutron diffraction spectra. *J. Appl. Phys.*, 81, 594-600.

MacEwan, S.R. and Tomé, C.N. (1987) in: Zirconium in the Nuclear Industry Seventh International Symposium, American Society of Testing and Materials, Philadelphia, PA. p. 631, ASTM STP 939.

Mallants, D., Marivoet, J. and Sillen, X. (2001) Performance assessment of the disposal of vitrified high-level waste in a clay layer. *J. of Nuclear Mater.* 298, 125–135.

Manafov, R.T., Holt, R.M. and Fjaer, E. (2007) Temperature sensitivity of wave velocities in shales. 69th EAGE meeting, London, UK, Expanded Abstracts.

Mann, U., Leythaeuser, D., Müller, P.J. (1986) Relation between source rock properties and wireline log parameters: An example from Lower Jurassic Posidonia Shale, NW-Germany. *Orga. Geochem.*, 10, 1105-1112.

Mann, U. (1987) Veränderung von Mineralmatrix und Porosität eines Erdölmuttergesteins durch einen Intrusivkörper (Lias epsilon 2–3: Hilsmulde, NW-Deutschland). *Facies*, 17, 181-188.

March, A. (1932) Mathematische Theorie der Regelung nach der Korngestalt bei affiner Deformation. *Zeitschrift fuer Kristallographie* 81, 285–297.

Markötter, H., Manke, I., Krügr, P., Arlt, T., Haussmann, J., Klages, M., Riesemeier, H., Hartnig, C., Scholta, J. and Banhart, J. (2011) Investigation of 3D water transport paths in gas diffusion layers by combined in-situ synchrotron X-ray radiography and tomography. *Electrochem. Commun.* 13, 1001-1004.

Marone, F., Hintermüller, C., McDonald, S., Abela, R., Mikuljan, G., Isenegger, A. and Stampanoni, M. (2009) X-ray Tomographic Microscopy at TOMCAT. *J. Phys.: Conference Series,* 186, 012042.

Martini, A.M., Walter, L.M., Ku, T.C.W., Budai, J.M., McIntosh, J.C. and Schoell, M. (2003) Microbial production and modification of gases in sedimentary basins: A geochemical case study from a Devonian shale gas play, Michigan basin. *AAPG Bulletin,* 87, 1355-1375.

Matthies, S. (1996) Moment pole figures in residual stress analysis. *Text Micro.* 25, 229-236.

Matthies, S. (2010) On the combination of self-consistent and geometric mean elements for the calculation of the elastic properties of textured multi-phase samples. *Solid State Phenom.* 160, 87–93.

Matthies, S. and Humbert, M. (1993) The realization of the concept of a geometricmean for calculating physical constants of polycrystalline materials. *Physica Status Solidi B* 177, K47–K50.

Matthies, S., Priesmeyer, H.G. and Daymond, M.R. (2001)On the diffractive determination of single-crystal elastic constants using polycrystalline samples. *J. Appl. Cryst.* 34,585-601.

Matthies, S. and Vinel, G.W. (1982) On the reproduction of the orientation distribution function of textured samples from reduced pole figures using the concept of conditional ghost correction. *Physica Status Solidi B*, 122, K111-K114.

Matthies, S. and Wenk, H.-R. (2009) Transformations for monoclinic crystal symmetry in texture analysis. *J. Appl. Crystall.* 42, 564–571.

Mavko, G., Mukerji, T. and Dvorkin, J. (1998) The Rock Physics Handbook. Cambridge University Press.

MAVI-Modular Algorithms for Volume Images, Fraunhofer Institut für Techno- und Wirtschaftsmathematik (2005).

Meirer, F., Cabana, J., Liu, Y., Mehta, A., Andrews, J.C. and Pianetta, P. (2011) 3D imaging of chemical phase transformations at the nanoscale with full field transmission X-ray microscopy. *J. Synchr. Rad.* 18, 773-781.

Merkel, S., Tomé, C.N. and Wenk HR. (2009) Modeling analysis of the influence of plasticity on high pressure deformation of hcp-Co. *Phys Rev B.* 79,064110.

Merkel, S., Wenk, H.-R., Gillet, P., Mao, H.-K., Hemley, R.J. (2004) X-ray diffraction study of the single crystal elastic moduli of e-Fe up to 30 GPa. *Phys. Earth Planet Inter.* 145, 239-251.

Merkel, S. and Yagi, T. (2005) X-ray transparent gasket for diamond anvil cell high pressure experiments. *Rev. Sci. Instru.* 76, 046109.

Midgley, P.A., Ward, E.P.W., Hungria, A.B. and Thomas, J.M. (2007). Nanotomography in the chemical, biological and materials sciences. *Chem. Soc. Rev.,* 36, 1477-1494.

Militzer, B., Wenk, H.-R., Stackhouse, S. and Stixrude, L. (2011) First-principles calculation of the elastic moduli of sheet silicates and their application to shale anisotropy. *Am. Mineral.,* 96, 125-137.

Mitri, F. G., Garzon, F. H. and Sinha, D. N. (2011) Characterization of acoustically engineered polymer nanocomposite metamaterials using x-ray microcomputed tomography. *Rev. of Sci. Instrum.* 82, 034903.

Miyagi, L., Kunz, M., Nasiatka, J., Voltolini, M., Knight, J., Wenk and H.-R. (2008) *In-situ* study of texture development in polycrystalline iron during phase transformations and deformation at high pressure and temperature. *J. Appl. Phys.* 104,103510.

Miyagi, L., Nishiyama, N., Wang, Y., Kubo, A., West, D.V., Cava, R.J., Duffy, T.S. and Wenk, H.-R. (2008) Deformation and texture development in $CaIrO_3$ post-perovskite phase up to 6 GPa and 1300 K. *Earth Planet. Sci. Lett.* 268,515-525.

Mondol, N.H., Jahren, J., Bjørlykke, K. and Brevik, I. (2008) Elastic properties of clay minerals. *The Leading Edge,* 27, 758–770.

Monteiro, P. J. M., Kirchheim, A. P., Chae, S., Fischer, P. , MacDowell, A. A., Schaible, E. and Wenk, H.-R. (2009) Characterizing the nano and micro structure of concrete to improve its durability. *Cem. Concr. Compos.* 31, 577-584.

Molinari, A., Canova, G.R. and Ahzi, S. (1987) Self consistent approach of the large deformation polycrystal viscoplasticity. *Acta Mater.* 35,2983-2994.

Morelli, A., Dziewonski, A.M. and Woodhouse J.H. (1986) Anisotropy of the inner core inferred from PKIKP travel times. *Geophys. Res. Lett.* 13,1545-1548.
Müller, J., Hipsley, C. A., Head, J. J., Kardjilov, N., Hilger, A., Wuttke, M. and Reisz, R. R. (2011) Eocene lizard from Germany reveals amphisbaenian origins. *Nature.* 473, 364-367.
Muñoz, Y.A., Littke, R. and Brix, M.R. (2007) Fluid systems and basin evolution of the western Lower Saxony Basin, Germany. *Geofluids*, 7, 335-355.
Nelson, G. J., Harris, W. M., Izzo Jr., J., Grew, K. N., Chiu, W. K. S., Chu, Y. S., Yi, J., Andrews, J. C., Liu, Y. and Pianetta, P. (2011) Three-dimensional mapping of nickel oxidation states using full field x-ray absorption near edge structure nanotomography. *Appl. Phys. Lett.* 98, 173109.
Nye J.F. (1956) The Physical Properties of Crystals. Clarendon.
Occelli, F., Farber, D.L., Badro, J., Aracne, C.M., Teter, D.M., Hanfland, M., Canny, B. and Couzinet, B. (2004) Experimental evidence for a high-[ressure isostructureal phase transition in osmium. *Phys. Rev. Lett.* 93,095502.
Oertel, G. and Curtis, C.D. (1972) Clay-ironstone concretion preserving fabrics due to progressive compaction. GSA Bulletin 83, 2597–2606.
Oertel, G. and Phakey, P.P. (1972) The texture of a slate from Nantille, Caernarvon, North Wales. *Texture.* 1, 1–8.
Ostanin, S.A. and Trubitsin, V.Y. (2000) Calculation of the P-T phase diagram of hafnium. *Comp. Mat. Sci.* 17,174-177.
Parkinson, D.Y. (2012) Manual of beamline 8.3.2., http://microct.lbl.gov/manual.
Pham, N.H., Carcione, J.M., Helle, H.B. and Ursin, B. (2002) Wave velocities and attenuation of shaley sandstones as a function of pore pressure and partial saturation. *Geophys. Prospect.* 50, 615–627.
Plançon A., Tsipurski, S.I. and Drits, V.A. (1985) Calculation of intensity distribution in the case of oblique texture electron diffusion. *J. Appl. Crystall.* 18, 191-196.
Petmecky, S., Meier, L., Reiser, H. and Littke, R. (1999) High thermal maturity in the Lower Saxony Basin: Intrusion or deep burial? *Tectonophysics*, 304, 317-344.
Prasad, M., Kopycinska, M., Rabe, U. and Arnold, W. (2002) Measurement of Young's modulus of clayminerals using atomic force acoustic microscopy. *Geophys. Res. Lett.* 29, 1172–1175.
Proust, G., Tomé, C.N., Kaschner, G.C. (2007) Modeling texture, twinning and hardening evolution during deformation of hexagonal materials. *Acta Mater.* 55, 2137-48.
Reuss, A. (1929) Berechnung der Fließgrenze von Mischkristallen auf Grund der Plastizitä tsbedingung für Einkristalle. Zeitschrift für, *Angewandte Mathematik und Mechanik* 9, 49–58.
Rietveld, H.M. (1969) A profile refinement method for nuclear and magnetic structures. *J. Appl. Crystall.*, 2, 65-71.
Rullkötter, J., Leythaeuser, D., Horsfield, B., Littke, R., Mann, U., Müller, P.J., Radke, M., Schaefer, R.G., Schenk, H.-J., Schwochau, K., Witte, E.G. and D.H.Welte. (1988) Organic matter maturation under the influence of a deep intrusive heat source: A natural experiment for quantitation of hydrocarbon generation and expulsion from a petroleum source rock (Toarcian shale, northern Germany). *Orga. Geochem.*, 13, 847-856.
Rundle, J.B. and Schuler, K.W. (1981) A composite model for the anisotropic elastic moduli of lean oil shale. *Geophysics* 46, 163–171.
Sams, M.S., Neep, J.P., Worthington, M.H. and King, M.S. (1997) The measurement of velocity dispersion and frequency-dependent intrinsic attenuation in sedimentary rocks. *Geophysics* 62, 1456–1464.
Sato, H., Ono, K., Johnston, C.T. and Yamagishi, A. (2005) First principles studies on elastic constants of a 1.1 layered kaolinite mineral. *Am. Mineral.* 90, 1824–1826.

Sayers, C.M. (1994) The elastic anisotropy of shales. *J. Geophys. Res.*, 99, 767-774.
Sayers, C.M. (1998) Misalignment of the orientation of fractures and the principal axes for P and S waves in rocks containing multiple non-orthogonal fracture sets. *Geophys. J. Inter.* 133, 459–466.
Schenk, C., Pollastro, R. and Ahlbrandt, T. (2002) Assessment of undiscovered oil and gas of the Lower Silurian Qusaiba-Paleozoic total petroleum system of the Arabian Peninsula. US Geological Survey Facts Sheet FS-008–02.
Schillinger, B., Lehmann, E. and Vontobel, P. (2000) 3D neutron computed tomography: requirements and applications. *Physica B*: Condens Matter. 276, 59-62.
Schulz, H.-M., Horsfield, B. and Sachsenhofer, R.F. (2010) Shale gas in Europe: a regional overview and current research activities. *Petrol. Geol. Conf. series*, 7, 1079-1085.
Sezgin, M. and Sankur, B. (2004) Survey over image thresholding techniques and quantitative performance evaluation. *J. Electron Imaging* 13, 146-165.
Singh AK, Balansingh C. (1994) The lattice strains in a specimen (hexagonal system) compressed nonhydrostatically in an opposed anvil high pressure setup. *J. Appl. Phys.* 75,10.
Singh, A.K., Balansingh, C., Mao. H.-K., Hemley, R.J., Shu, J.F. (1998) Analysis of lattice strains measured under nonhydrostatic pressure. *J. Appl. Phys.* 83,7567-7575.
Sintubin, M. (1994a) Clay fabrics in relation to the burial history of shales. *Sedimentology,* 41, 1161-1169.
Sintubin, M. (1994b). Phyllosilicate preferred orientation in relation to strain path determination in the lower Paleozoic Stavelot-Venn Massif (Ardennes, Belgium). *Tectonophysics* 237, 215–231.
Slaughter, M. and Hill, R.J. (1991) The influence of organic matter in organogenic dolomization. *J. Sediment. Res.*, 61, 296-303.
Stampanoni, M., Borchert, G., Wyss, P., Abela, R., Patterson, B., Hunt, S., Vermeulen, D. and Rüegsegger, P. (2002) High-resolution X-ray detector for synchrotron-based microtomography. *Nucl. Inst. Methods Phys. Res.* 491, 291-301.
Stampanoni, M., Groso, A. Isenegger, A., Mikuljan, G., Chen, Q., Bertrand, A., Henein, S., Betemps, R., Frommherz, U., Böhler, P., Meister, D., Lange, M. and Abela, R. (2006) Trends in synchrotron-based tomographic imaging: the SLS experience. *In:* Ulrich Bonse (ed), Developments in X-ray Tomography V, *Proceedings of SPIE,* 6318, 63180M.
Stixrude, L., Wasserman, E. and Cohen, R. (1997) Composition and temperature of earth's inner core. *J. Geo. Res.* 102,24729-739.
Takemura, K. (1997) Structural study of Zn and Cd to ultrahigh pressure. *Phys. Rev. B* 56,5170.
Takemura, K. (2004) Bulk modulus of osmium: high-pressure powder x-ray diffraction experiments under quasihydrostatic conditions. *Phys. Rev. B.* 70, 012101.
Tenckhoff, E. (1988) Deformation mechanisms-texture and anisotropy in zirconium and zircoaloy. ASTM 966 Philadelphia, PA.
Terasaki, H., Urakawa, S., Funakoshi, K., Nishiyama, N., Wang, Y., Nishida, K., Sakamaki, T., Suzuki, A. & Ohtani, E. (2009) *Phys. Earth Planet. In.* 174, 220-226.Thomsen L. 1986. Weak elastic anisotropy. Geophysics 51, 1954–1966.
Tissot, B.O. and Welte, D.D. (1984) Petroleum Formation and Occurrence, 2nd edn. Springer-Verlag.
Valcke, S.L.A., Casey, M., Lloyd, G.E., Kendall, J.-M. and Fisher, Q.J. (2006) Lattice preferred orientation and seismic anisotropy in sedimentary rocks. *Geophys. J. Inter.*, 166, 652-666.
Vernik, L. (1994) Hydrocarbon-generation-induced microcracking of source rocks. *Geophysics,* 59, 555-563.
Vernik, L. (1993) Microcrack-induced versus intrinsic elastic anisotropy in mature hc-source shales. *Geophysics*, 58, 1703-1706.

Vernik, L. and Liu, L. (1997) Velocity anisotropy in shales: A petrophysical study. *Geophysics* 62, 521–532.

Vernik, L. and Nur, A. (1992) Ultrasonic velocity and anisotropy of hydrocarbon source rock. *Geophysics*, 57, 727-735.

Vidal, F.P., Letang, J.M., Peix, G. & Cloetens, P. (2005) Investigation of artefact sources in synchrotron microtomography via virtual X-ray imaging. *Nucl. Inst. Methods Phys. Res.* B 234, 333-348.

Voigt, W. (1928) Lehrbuch der Kristallphysik. Teubner-Verlag.

Voigt, W. (1887) Theoretische Studien über die Elasticitätsverhältnisse der Krystalle. Abh. Kgl. Ges. Wiss. Göttingen, Math.Kl. 34.

Voltolini, M., Wenk, H.-R., Mondol, N.H., Bjørlykke, K. and Jahren, J. (2009) Anisotropy of Experimentally Compressed Kaolinite-Illite-Quartz mixtures. *Geophysics,* 74, 13-23.

Voltolini, M., Zandomeneghi, D., Mancini, L. and Polacci, M. (2011) Texture analysis of volcanic rock samples: Quantitative study of crystals and vesicles shape preferred orientation from X-ray microtomography data. *J. Volcanol. Geoth. Res.* 202, 83-95.

Wang, Z. (2002) Seismic anisotropy in sedimentary rocks: Part 2 – Laboratory data. *Geophysics,* 67, 1423–1440.

Wang, Z., Wang, H. and Cates, M.E. (2001) Effective elastic properties of solid clays. *Geophysics,* 66, 428–440.

Wang, Y., De Carlo, F. D., Mancini, C., McNulty, I., Tieman, B., Bresnahan, J., Foster, I., Insley, J., Lane, P., von Laszewski, G., Kesselman, C., Su, M.-H. and Thiebaux, M. (2001) A high-throughput x-ray microtomography system at the Advanced Photon Source. *Rev. Sci. Instrum.* 72, 2062-2068.

Wenk, H.-R., Baumgardner. J., Lebensohn. R.A., Tomé, C.N. (2000b) A convection model to explain anisotropy of the inner core. *J. Geophys. Res.* 105, 5663-5677.

Wenk, H.-R., Kanitpanpanyacharoen, W. and Voltolini, M. (2010) Preferred orientation of phyllosilicates: Comparison of fault gouge, shale and schist. *J. of Struct. Geol.*, 32, 478-489.

Wenk H.-R., Lonardelli I., Franz H.,Nihei K. andNakagawa S. (2007) Preferred orientation and elastic anisotropy of illite-rich shale. *Geophysics,* 72, E69–E75.

Wenk, H.-R., Matthies, S., Donovan, J. and Chateigner, D. (1998) Beartex: A windows-based program system for quantitative texture analysis. *J. Appl. Crystall.*, 31, 262-269.

Wenk, H.-R., Matthies, S., Hemley, R.J., Mao, H.-K., Shu, J. (2000) The plastic deformation of iron at pressures of the Earth's inner core. *Nature.* 405,1044-1047.

Wenk, H.-R., Voltolini, M., Mazurek, M., Loon, L.R.V. and Vinsot, A. (2008) Preferred orientations and anisotropy in shales: Callovo-Oxfordian shale (France) and Opalinus clay (Switzerland). *Clays Clay Min.*, 56, 285-306.

Wenk, H.-R., Voltolini, M., Kern, H., Popp, T. and Mazurek, M. (2008b) Anisotropy in shale from Mont Terri. *The Leading Edge*, 27, 742–748.

Wirth, R. (2009) Focused Ion Beam (FIB) combined with SEM and TEM: Advanced analytical tools for studies of chemical composition, microstructure and crystal structure in geomaterials on a nanometre scale. *Chem. Geol.* 261, 217–229.

Yoo, M.H. (1981) Slip, twinning, and fracture in hexagonal close-packed metals. *Metall. Trans. A.* 12A, 409-418.

Zhu, W., Gaetani, G.A., Fusseis, F., Montési, L.G.J. and De Carlo, F. (2011) Microtomography of partially molten rocks: three-dimensional melt distribution in mantle peridotite. *Science* 332, 88-91.